Development of creep resistant titanium aluminide alloys for the Metal Injection Moulding process

Von der Fakultät für Maschinenbau, Elektrotechnik und Wirtschaftsingenieurwesen der Brandenburgischen Technischen Universität Cottbus zur Erlangung des akademischen Grades eines Doktors der Ingenieurwissenschaften genehmigte Dissertation

vorgelegt von

Master of Science

Juliano Soyama

geboren am 28. August 1984 in Matelândia, Brasilien

Vorsitzender: Prof. Dr.-Ing Bernd Viehweger

Gutacher: Prof. Dr.-Ing Florian Pyczak

Gutacher: Prof. Dr.-Ing Karl Ulrich Kainer

Tag der mündlichen Prüfung: 02. Oktober 2014

Acknowledgements

Firstly, I would like to thank my supervisors Dr. Thomas Ebel and Prof. Dr. Florian Pyczak for the guidance, patience and helpful discussions throughout my PhD.

I am greatly thankful for the technical and scientific support of all colleagues at Helmholtz-Zentrum Geesthacht:

Andreas Dobernowsky, Christian Siewers, Dirk Matthiessen, Dr. Frank-Peter Schimansky, Frank Nickel, Gert Wiese, Günter Meister, Dr. Heike Gabrisch, Jens Hübscher, Jürgen Knaack, Kay Erdmann, Marcus Rackel, Martin Wolff, Prof. Dr. Michael Dahms, Petra Fischer, Peter Haack, René Dinse, Dr. Roland Hoppe, Sabine Schrader, Dr. Sangbong Yi, Stefan Eggert, Stefan Riekehr, Dr. Ulrich Fröbel, Uwe Lorenz and Wolfgang Limberg.

Special thanks to:

Dr. Michael Oehring for all the fruitful discussions and for proof reading the manuscript of my PhD thesis. Dr. Jonathan Paul for the assistance with the creep measurements. Dr. Andreas Stark for the assistance with the HEXRD measurements and analysis, as well as Dr. Chamini Lakshi Mendis for providing me with diffraction patterns. Prof. Dr. Karl Ulrich Kainer for the scientific support and assistance with the manuscript of the PhD thesis.

The students that assisted me throughout my work, Annika Mainusch, Martin Holm, Martin Vogel and Rafael Paiotti Marcondes Guimarães.

The friends that made the long years of my PhD very cheerful, Alencar Marcon Milioli, André Bastos Abibe, Björn Wiese, Cesar Augusto Stüpp, Daniela Penther, Da-Peng Zhao, Diego Blaese, Domonkos Tolnai, Douglas Dal Pozzo, Elias Sakkal, Emerson Luis Dal Pozzo, Gabor Szakacs, Gabriel Freitas Nunes, Gustavo Teixeira, Henrique Kazuo Matsumoto, Jan Carstensen, Javier Trinidad, Jonathan Inzunza, José Victoria Hernandez, Leandro Neckel, Lígia Nascimento Silva Ferri, Lilian Rayas Martinez, Luciano Andrei Bergmann, Lucian Blaga, Luciana Cemin, Lydia Katsarou, Maria Domenica Constantino, Maria del Rosario Silva Campos, Marta Mohedano Sanchez, Maximilian Hehenberge, Murilo Pereira Hablitzel, Orley Milagres Ferri, Paula de Oliveira Guglielmi, Ricardo Henrique Buzolin, Ricardo Peniche, Rodrigo Pacher Fernandes, Seyed Mohammad Goushegir, Vanessa Fischer da Silveira Fischer and Viviane Teixeira.

Lastly, my family, without their support I could never have accomplished this work.

Abstract

Titanium aluminides show great technological potential due to their light weight and excellent creep resistance. Their utilisation thus offers a potential to decrease fuel consumption and simultaneously improve the performance of components subjected to stress at high temperatures. However, shaping of titanium aluminides is still a very challenging and costly task considering their brittleness and the sensitivity on chemical composition. Therefore powder metallurgy near-net shape manufacturing techniques are very attractive to decrease material waste and reduce overall processing costs.

This research work was focused on the preparation, characterisation and optimisation of creep resistant titanium aluminides for the Metal Injection Moulding (MIM) process. Considering the little information available regarding processing of titanium aluminides by MIM, this work had firstly the goal of assessing the creep behaviour of a reference titanium aluminide alloy. Secondly, alloy variations with compositions based on the reference material were designed with the objective of improving the creep resistance, especially concerning primary creep. The basic strengthening mechanisms applied involved the addition of slow diffusing elements and elements that cause precipitation of hard particles.

The specimens were prepared by using pre-alloyed powder and mixtures of a master alloy (pre-alloyed) and elemental powders. Consequently, a great deal of effort was spent in the characterisation of the sintering behaviour in order to achieve reliable test pieces. Even though both methods can deliver sound specimens, the pre-alloyed powder approach led to the best results in terms of residual porosity and microstructural homogeneity.

The mechanical testing results indicate that processing of titanium aluminides by MIM is feasible and acceptable creep properties can be achieved with the proper sintering parameters. Even though the ductility at room temperature was considerably limited due to the residual porosity and high amounts of impurities intrinsic to the MIM process, alloys developed within this study showed improved primary creep resistance in the high stress – high temperature regime. In particular alloy variations containing additions of Mo, Si and Gd led to a considerable improvement of the primary creep resistance in comparison to the reference material at 800 °C – 350 MPa loading.

Kurzfassung

Titanaluminide zeigen ein großes technologisches Potenzial durch ihre geringe Dichte und hervorragende Kriechfestigkeit. Deswegen kann durch ihre Verwendung der Kraftstoffverbrauch reduziert und gleichzeitig die Gesamtleistung von mechanisch belasteten Hochtemperaturkomponenten verbessert werden. Die Formgebung von Titanaluminiden ist jedoch noch ein sehr schwieriger und kostenintensiver Prozess, vor allem aufgrund der Sprödigkeit und der starken Abhängigkeit der Eigenschaften von der chemischen Zusammensetzung. Daher sind pulvermetallurgische „near-net shape“ Fertigungstechniken sehr attraktiv in Bezug auf Reduzierung des Materialabfalls und der Gesamtverarbeitungskosten.

Inhalt diese Arbeit war die Herstellung, Charakterisierung und Optimierung von kriechfesten Titanaluminiden für das Metallpulverspritzguss-Verfahren (Metal Injection Moulding – MIM). Angesichts der wenigen existierenden Informationen über die Verarbeitung von Titanaluminiden durch MIM war das erste Ziel dieser Arbeit die Ermittlung des Kriechverhaltens einer Referenz-Titanaluminid-Legierung. Zweitens wurden Legierungsvarianten auf Basis des Referenzmaterials mit dem Ziel der Verbesserung der Kriechfestigkeit hergestellt, insbesondere in Bezug auf primäres Kriechen. Das Design der Legierungsvarianten basierte dabei auf der Anwendung folgender grundlegender Verstärkungsmechanismen: Zugabe von langsam diffundierenden Elementen und von Elementen, die härtende Ausscheidung bilden können.

Die Proben wurden entweder aus vorlegierten Pulvern oder Mischungen aus einer Masterlegierung (vorlegiert) und Elementarpulvern hergestellt. Um eine Überlagerung von fertigungsbedingten Faktoren, wie hohe Porosität, auf die ermittelten mechanischen Eigenschaften auszuschließen, wurde zuerst eine intensive Charakterisierung des Sinterverhaltens durchgeführt. Obwohl mit beiden Methoden geeignete Proben herstellbar waren, führte die Verwendung von vorlegierten Pulvern zu den besten Ergebnissen in Bezug auf Restporosität und Gefüge-Homogenität.

Die Ergebnisse der mechanischen Versuche zeigen, dass die Verarbeitung von Titanaluminiden durch MIM möglich ist und eine mit etablierten Herstellungsverfahren konkurrenzfähige Kriechfestigkeit mit den richtigen Sinterparametern erreicht werden kann. Obwohl sich die mit dem MIM Verfahren verbundene Restporosität und den relativ hohen Gehalt an Verunreinigungen negativ auf die Raumtemperaturduktilität auswirkten, zeigten die neuen Legierungen eine verbesserte primäre Kriechfestigkeit im Bereich hoher Spannungen und Temperaturen. Insbesondere die Legierungsvarianten, die Zusätze von Mo, Si und Gd enthalten, führten zu einer erheblichen Verbesserung der primären Kriechbeständigkeit im Vergleich zum Referenzmaterial bei 800 ° C und 350 MPa Belastung.

Table of contents

List of figures

List of tables

1. Introduction

Titanium aluminides are promising candidates for various high temperature applications [1–9] due to their good creep resistance and high specific strength. The constitution of these materials is based on ordered intermetallic phases that, as a direct consequence, provide high temperature strength but limit the ductility at room temperature [10]. Additionally, given the multitude of possible phase transformations and the sensitive dependence on chemistry in the compositional range of engineering alloys, shaping of titanium aluminides is extremely challenging. Nonetheless, titanium aluminides have been successfully processed by many techniques including casting [11–13], forging [14–16] and powder metallurgy [17,18]. Powder metallurgy offers some highly attractive advantages such as fine and homogeneous microstructures, isotropic properties (no texture), as well as the possibility of significantly decreased production costs through near-net shaping.

Powder metallurgy processing of titanium aluminides is multifaceted and several PM techniques have been reported to provide reasonable properties. In the 90's a lot of effort in PM research was aimed at shaping elemental powders followed by reactive sintering [19–25]. This particular route has the advantage of shaping unreacted mixtures of elemental titanium and aluminium powders, thus allowing easy fabrication of complex forms through green machining. Consequently, the use of the more expensive pre-alloyed powders is not necessary. However, additional heat treatments are always necessary to achieve the desired intermetallic phases. This involves the formation of many intermediate phases through exothermic reactions often leading to high porosity. Later some research works also focused on Hot Isostatic Pressing (HIP) of powders followed by subsequent forming operations [26,27] culminating in the production of titanium aluminide sheets. More recently, a wider variety of near-net shape powder processing techniques have been tried including layered additive manufacturing (Electron Beam Melting [28,29] and Selective Laser Sintering [30,31]) and Metal Injection Moulding (MIM) [16,17,32–37].

MIM has a great potential from the manufacturing point of view, if small parts with complex geometries are to be fabricated. The possibility to rapidly produce a great volume of near-net shape components at low costs could further push titanium aluminides in applications where traditional materials are normally employed. Furthermore, the popularisation of MIM-TiAl would simultaneously create a cultivating ground for new applications in which the production costs are the limiting factor for the materials' choice, such as in the automotive

industry. Therefore the limited use of rather expensive titanium aluminides could be considerably expanded by developments in MIM, and both novel and traditional applications could profit from the extraordinary properties of this class of materials.

There are however, up to this date, only a few published research works regarding MIM of titanium aluminides [16,34–40]. Besides, no particular work addressed directly the characterisation of creep behaviour. The presence of residual mostly round porosity and the inevitable uptake of additional impurities during processing make the MIM process special compared to more traditional fabrication techniques. An initial assessment of the creep behaviour is of great importance to elucidate if the MIM microstructures are detrimental in comparison to competing and more mature techniques like casting, for example. Moreover, in case of most engineering components that are exposed to creep loading, the maximum allowed plastic deformation during application is normally limited to 1% or less. Since this amount of deformation takes often place usually within the primary creep regime of titanium aluminide alloys, the investigation of the initial stage of creep is of uttermost interest.

Given the importance of primary creep from the application point of view, several research works have investigated the influence of different factors such as different stress levels [41,42], lamellar spacing [43,44], aging [42,45] and the presence of β phase in the microstructure [46,47]. Publications dealing with the underlying mechanisms of primary creep [41,48–51] are also available. In spite of that, no systematic study focused specifically on the optimisation of the primary creep resistance in the high stress – high temperature regime through alloy design. Considering that powder metallurgy is a relatively easy and fast method for the preparation of different compositions, screening of alloying elements that could potentially enhance primary creep resistance is possible with limited effort.

1.1 Scope of this work

The main objective of this research work is the characterisation and optimisation of the primary creep resistance of titanium aluminides prepared by MIM. Firstly, the primary creep behaviour of a reference titanium aluminide alloy is characterised in order to achieve an overview and to have a reference for comparison with the literature data available. For that purpose, the alloy TNB-V5 has been chosen due to its balanced mechanical properties and excellent creep resistance [52–54]. Secondly, a series of specimens containing various promising alloying elements for the optimisation of primary creep resistance is elaborated.

The alloying elements are chosen based on their effect on the microstructure and consequently on primary creep resistance. These included addition of the heavy elements W, Nb, Ta and Mo for solid solution hardening and to slow down diffusional processes, as well as the addition of the elements Si and Gd that induce precipitation strengthening. The effect of C and N is also considered in the context of both mentioned mechanisms, since their presence is process-related.

In order to achieve the described objectives, the creep behaviour of TNB-V5 prepared by two different techniques (powder metallurgy and arc melting) is measured in compression. Compression creep has been chosen as the main parameter due to the simplicity of specimen preparation and testing. Afterwards, screening of alloying elements through compression creep is performed in order to find the best alloy candidates. The selection of the candidates is conducted in an eliminating fashion, in which the alloys that showed poor performance in compression creep in the as-sintered condition are not further considered.

The alloy variations are prepared by blending a master alloy (pre-alloyed TNB-V5) and elemental powders to achieve different compositions. This approach is necessary considering that the use of pre-alloyed powder for small screening batches at laboratory scale is not viable. Additionally, in order to achieve reasonable properties, MIM components are required to have low porosities (<5 %), consequently the characterisation of the sintering behaviour of the alloy variations and the reference material is essential. Plenty of parameter studies for sintering have been published [16,33–35,37] but since sintering is highly dependent on the conditions of each particular sinter furnace and on alloy composition, a study of the sintering behaviour is inevitable during the alloy development process.

2. Theoretical background

2.1 Titanium aluminides

Titanium aluminides are multi-phase advanced intermetallic engineering materials. Intermetallics are composed of two or more different metals and show a different crystal structure than the parent materials [55]. Usually there is a strong atomic binding between the species and, in contrast to pure metals, intermetallics contain both metallic and covalent bonds. As the intermetallic phase is formed, a long range ordering of the atoms often follows, which provides increased strength, especially at high temperatures, but reduced ductility and fracture toughness [56]. Titanium aluminides are therefore very attractive candidates for high temperature applications in aerospace [4,57] and automotive industries [2,5] due to the high specific strength, good oxidation resistance and outstanding creep properties [58].

Despite the large number of phases that can be found in the binary Ti-Al phase diagram (Figure 1), only few of them are of engineering interest. The most studied and therefore known alloys are based on the tetragonal γ (TiAl) and variable amounts of hexagonal α_2 phase (Ti_3Al). These alloys lie in the range of 43 to 48 at.% aluminium and contain the following phases [58]:

- Ordered hexagonal close-packed α_2 phase (Ti_3Al) with the structure $D0_{19}$;
- Ordered face centred tetragonal γ phase (TiAl) with the crystalline structure $L1_0$ and a slightly distorted *c*/*a* ratio of ≈ 1.02;
- Body centred cubic β titanium (A2), which can also exist in an ordered (B2) form referred to as β_0 (usually not displayed in the binary diagram);
- Disordered hexagonal close-packed α titanium (A3).

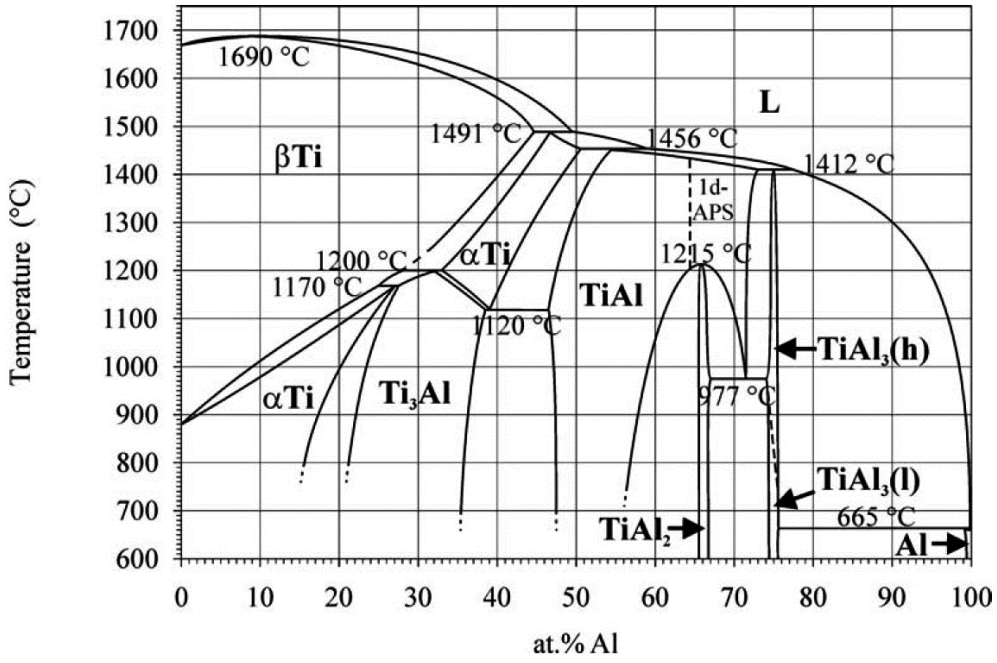

Figure 1 – Ti-Al binary phase diagram, according to Schuster and Palm [59].

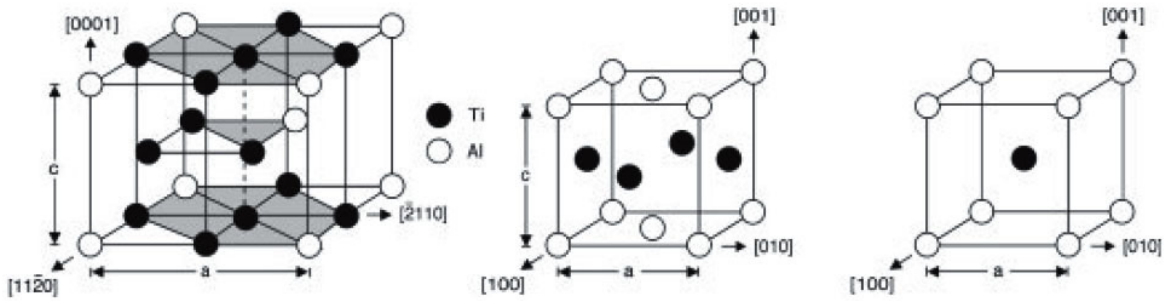

Figure 2 – Crystal structure of (from left to right) α_2 (Ti_3Al), γ (TiAl) and β_0 titanium phases [58].

In the aluminium range of typical two-phase titanium aluminides (43-48 at.%), the presence of one peritectic and one eutectoid point can be found. Casting, forging, extrusion, powder metallurgy, etc. make use of starting materials that were once solidified from the melt. Thus, solidification paths play a critical role by influencing microstructure and properties independent of the processing technique intended. In the special case of powder metallurgy, sintering temperatures might be above the solidus line. It is thus likely that formation of liquid phase during sintering takes place. Consequently, phase transformations related to the solidification paths are induced, which also have an influence on the distribution of alloying elements and the presence of segregations. Dependent on the aluminium content two principal solidification paths are found in titanium aluminides:

- Peritectic solidification: $L + \beta \rightarrow \alpha + \beta \rightarrow \alpha \rightarrow \alpha + \gamma \rightarrow \alpha_2 + \gamma$
- Solidification through the β phase field: $L + \beta \rightarrow \beta \rightarrow \alpha + \beta \rightarrow \alpha \rightarrow \alpha + \gamma \rightarrow \alpha_2 + \gamma$

The peritectic solidification starts with the solidification of primary β phase that coexist with the liquid in a two phase field. At the peritectic point, approximately 1491 °C (for binary alloys), the α phase can either originate from the melt or from the β phase, the latter following the Burgers orientation relationship [60]:

$$\{110\}_\beta \,//\, (0001)_\alpha \text{ and } < 111 >_\beta \,//\, < 11\bar{2}0 >_\alpha$$

If the α phase originates from the β phase, it should be oriented in 12 possible variants, however, as Singh et al. [61] explained, in cases of strong temperature gradients, e.g. chilled mould walls, only one variant of the 12 was observed to envelop a parent β phase. Additionally, according to Johnson et al. [62], the α phase actually precipitates heterogeneously from the melt because it was found to grow at its preferential direction [0001], which was not related to the β phase. This implies that in the case of peritectic solidification through $L + \beta \rightarrow \alpha$, the α phase controls the final texture of the material and also forms large columnar grains because it grows through the β dendrites as a consequence of low nucleation and very rapid growth rates.

Solidification through the β phase provides a more homogenous distribution of alloying elements, also leading to a more refined microstructure in comparison to peritectic solidification [63]. Firstly, solidification starts by precipitation of β phase coexisting with the melt and later it is completely solidified ($L + \beta \rightarrow \beta$). Further phase transformations occur entirely in the solid state.

The $\beta \rightarrow \alpha$ transformation can occur in different ways depending on the cooling rate. For the case of furnace cooling, the α phase either precipitates at the boundaries of β grains or, for slower cooling rates, inside the β grain, creating a Widmannstätten microstructure, similarly to titanium alloys [56]. The α phase originates from the parent β phase and it follows the Burgers orientation relationship, which allows 12 possible orientations of the α phase [64]. Additionally, solidification through the β phase decreases texture formation. This in particular was applied to optimise cast microstructures [65–67].

Following solidification and $\beta \rightarrow \alpha$ phase transition, two other important solid state transformations take place with moderate cooling rates. Firstly, once the two-phase field $\alpha + \gamma$ is crossed during cooling, the γ phase starts to precipitate ($\alpha \rightarrow \alpha + \gamma$). Later at the eutectoid point (~1120 °C in binary alloys), the α phase becomes ordered together with further formation of γ phase ($\alpha + \gamma \rightarrow \alpha_2 + \gamma$). The final microstructure consists of alternating plates of α_2 and γ phases forming a lamellar structure. In contrast to pearlite formation in steels, this transformation is not discontinuous and the γ lamellae are actually precipitated directly from the α phase [68] following the Blackburn relationship [69]:

$$(0001)_{\alpha 2} \,//\, \{111\}_{\gamma} \text{ and } < 11\bar{2}0 >_{\alpha 2} \,//\, < 1\bar{1}0]_{\gamma}$$

According to Kim [70], the microstructures that can be developed in forged two-phase titanium aluminides upon heat treatment are virtually unlimited. Nevertheless all variations can be classified in four groups: near-gamma, duplex, nearly-lamellar and fully lamellar. Examples of these microstructures are displayed in Figure 3. Each particular microstructure offers different advantages in regard to property optimisation. For the case of creep resistance and fracture toughness, a fully lamellar microstructure with narrow lamellar spacing is usually the best choice [71,72], while for maximum ductility and strength at room temperature a duplex microstructure is required [73,74].

From the binary phase diagram it is possible to see that the γ phase fraction increases as the temperature decreases, therefore annealing treatments at different temperatures can generate the different groups of microstructures. Holding at the α phase field followed by furnace cooling creates the fully lamellar microstructure, whereas the other microstructures are obtained by annealing in the two-phase field $\alpha + \gamma$. The lower the temperature of this annealing step (as indicated by the arrows in Figure 3), the larger the thermodynamic stable fraction of γ phase. For annealing treatments conducted slightly above the eutectoid point, the near-gamma microstructure is achieved.

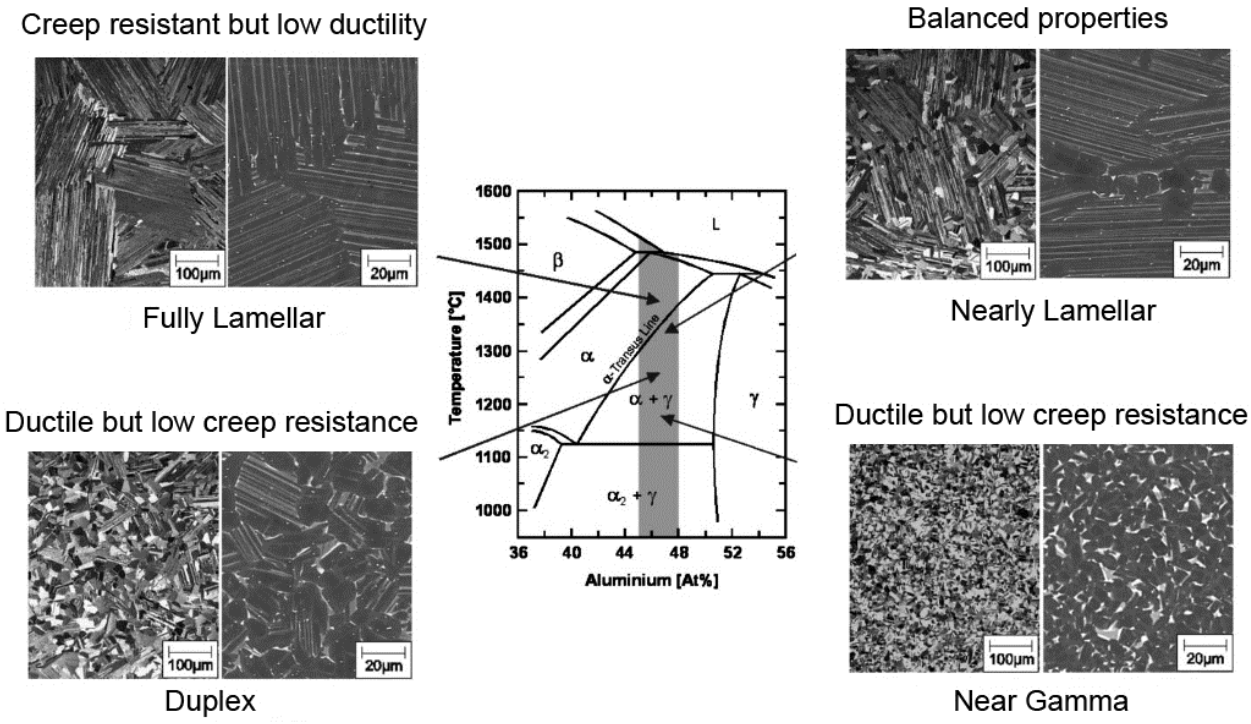

Figure 3 – Different microstructures that can be obtained by thermomechanical treatment of two-phase titanium aluminides [9,75].

2.2 Creep

When materials are subjected to mechanical loadings at elevated temperatures, even at stresses below the yield strength, a time-dependent deformation process takes place, leading to a continuously increasing strain and ultimately to failure. This phenomenon is known as creep [76,77]. Normally, creep deformation becomes important for temperatures in the order of 0.5 T_m, where T_m is the melting temperature; however this estimate is material dependent and might vary considerably.

The characterisation of creep behaviour is essential for the life time prediction of components that are subjected to stress at elevated temperatures. Most engineering materials display typically three distinct regions during creep, as displayed in Figure 4 [77–79]. These regions are normally called primary, secondary and tertiary creep regime.

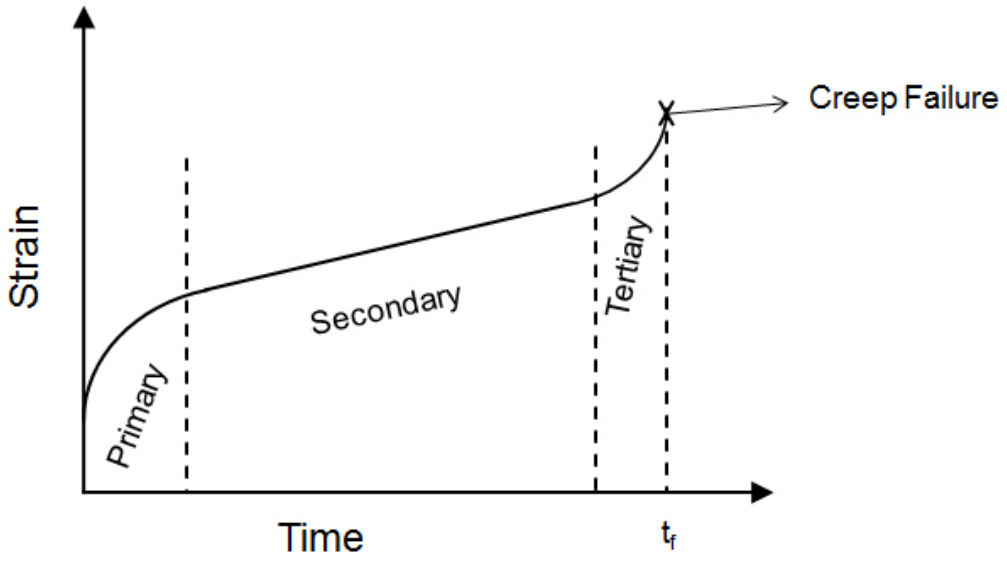

Figure 4 – Schematic representation of a creep curve with a fixed load and temperature. The time until failure is indicated as t_f. Adapted from [79].

- **Primary creep**: firstly upon loading, the material deforms elastically, which occurs almost instantaneously. Primary creep follows after the initial elastic deformation. The primary creep regime is characterised by a decreasing strain rate as a function of time (time dependent transient strain) reaching a value of minimum creep rate. Primary creep is governed by hardening processes normally associated with dislocations interactions [77].

- **Secondary creep**: after the primary creep regime, the strain rate reaches a nearly constant value (steady-state strain rate) due to an equilibrium between hardening and softening, e.g. dislocation generation and annihilation. The secondary creep regime is characterised by a balance of recovery and work hardening over a long strain interval [10,77].

- **Tertiary creep**: after the secondary creep regime, the strain rate rapidly increases due to creep damage. The tertiary creep regime is characterised by the formation of creep cavities and cracks [76], but recrystallisation of the heavy deformed microstructure and precipitate coarsening [80,81] might also contribute. Cavities additionally decrease the load bearing cross section and might act as stress concentration sites. Creep failure normally occurs within the tertiary creep regime.

Depending on the load and temperature combinations, different creep mechanisms can be dominating and thus be rate controlling during steady-state creep (secondary creep). At moderate to high stresses and moderate to high temperatures, the plastic deformation in steady-state creep follows a phenomenological power law relationship, which combined with an Arrhenius equation can adequately describe secondary creep [77].

$$\dot{\varepsilon} = A(\sigma_a)^n exp\left(-\frac{Q_c}{RT}\right) \qquad \textbf{Equation 1}$$

Where A is a microstructure dependent material quantity (assumed constant), σ_a the applied stress, n the stress exponent, R the universal gas constant, T the temperature and Q_c the activation energy for creep. As explained by Kassner [77], Q_c describes the change in creep rate for a given substructure (strength), at a fixed applied load with changes in temperature.

In the case of pure metals, the activation energy (Q_c) shows a good correlation with the activation energy for self-diffusion in various stress and temperature combinations [82–84]. Additionally, the stress exponent (n) usually assumes a value of approximately 5 for power law creep, which indicates that the creep process is controlled by a climb mechanism [77].

At very high stresses and temperatures, the steady-state creep rate shows a drastic increase with increasing stress, characterising a power law breakdown. In this case, the stress exponent might increase to large values ($n > 5$), while Q_c typically decreases [77]. The power law breakdown is usually associated with a transition from a diffusion climb controlled creep to thermally activated dislocation glide [85].

At low stresses diffusional flow is the dominating mechanism. In this region, plastic deformation takes place through diffusion of vacancies. Grain boundaries act as a preferred source and sink for vacancies, therefore under uniaxial tensile stress, an excess of vacancies is accumulated at the grain boundaries perpendicular to the stress axis [77]. The pathway for diffusion can be along grain boundaries (Cobble creep) and/or through the lattice (Nabarro-Herring creep). Both creep mechanisms show a stress exponent of 1.

2.3 Creep behaviour of titanium aluminides

A typical strain vs. time creep curve of a titanium aluminide alloy (Ti-45Al-10Nb) is displayed in Figure 5 together with a corresponding strain rate vs. strain curve. The end of

the primary creep regime is clearly identified by an inflection of the strain rate, which corresponds to the minimum creep rate. It is noteworthy that in the case of titanium aluminides the secondary creep regime is often very small or almost absent. Consequently, the strain rate increases continuously after primary creep.

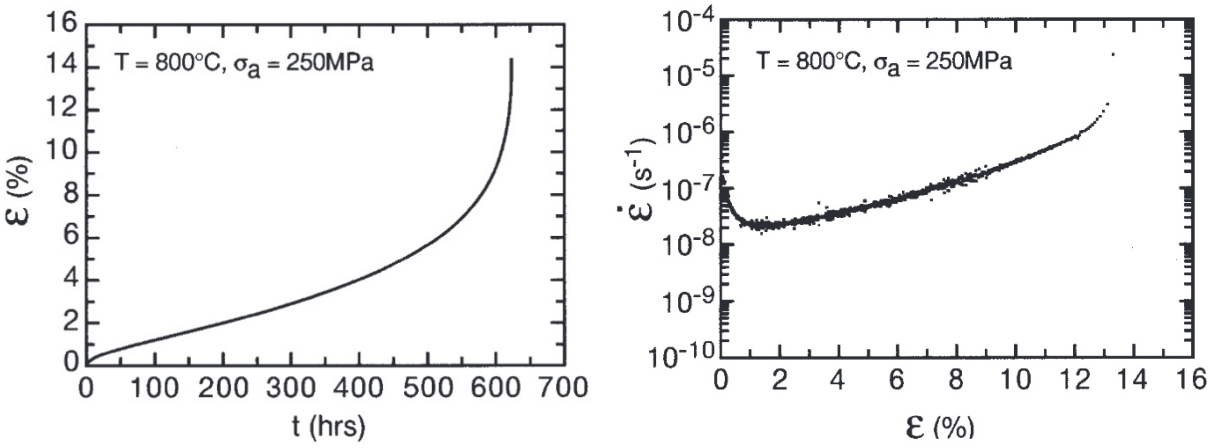

Figure 5 – Creep data of Ti-45Al-10Nb. (a) Creep curve recorded until rupture. (b) Strain rate plotted as a function of strain. Curves extracted from [53].

2.3.1 Critical microstructural features

The creep behaviour of titanium aluminides is greatly influenced by the microstructure. Among all different microstructures possible, the fully lamellar is the most creep resistant, when compared to other variants with the same chemical composition [73,86]. The reason for the high creep resistance of the fully lamellar microstructure is the reduced slip length achieved through the fine lamellae. Moreover, there is an additional contribution from the coherency stresses at the interfaces that need to be overcome for the movement of dislocations [87]. Considering the importance of the fully lamellar microstructure for creep resistant titanium aluminide alloys, only the parameters involving this type of microstructure will be addressed in this work.

The colony size has been shown to influence the creep resistance but only up to about 100 µm. Parthasarathy et al. [88] conducted a comparative study with literature data and concluded that the effect of grain size in fully lamellar alloys was insignificant between 100-1200 µm. Maruyama et al. [72] studied two different alloys binary Ti-42Al and Ti-48Al-2Nb-2Cr prepared with the same lamellar spacing but varying colony sizes and found that little

change occurred for sizes larger than 100 μm. The authors explained that due to the strain induced grain boundary migration, dynamic recrystallisation occurred resulting in fine grains at the boundaries. The creep rate of fully lamellar microstructures is increased, if grain boundary instability due to recrystallisation takes place. Under creep conditions, the fully lamellar microstructure undergoes a spheroidisation process through localised shear deformation at colony boundaries [89]. This process leads to smaller colony sizes and consequently to higher creep rates.

The refinement of lamellar spacing normally leads to higher creep resistance according to results of different studies [88,72,43,90–93]. Wen et al. [91] pointed out three different mechanisms that account for this effect. Firstly, the amount of lamellar interfaces increases with finer lamellae. The larger the volumetric amount of interfaces, the more difficult it is for dislocations to glide. Secondly, dislocation segments get trapped at interfacial boundaries, which could further restrict dislocation motion. Lastly, the presence of finer lamellae can prevent additional dislocation generation from the interfaces. Fine lamellae can more effectively block the dislocations before they reach a critical shape (e.g. semicircle), which would facilitate further multiplication of dislocations.

On the other hand, the presence of fine lamellae can be a disadvantage because they are not thermally stable and thus prone to coarsening. As described by Yamamoto et al. [94] this effect becomes noticeable at low stresses. Below 100 MPa at 927 °C, a lamellar spacing of 0.1 μm gave a higher minimum creep rate than 0.25 μm. The authors explained that the prominent discontinuous coarsening of the fine lamellar structure was responsible for the low creep resistance. It was suggested that a stabilising treatment for the lamellae might improve the creep strength by completing the discontinuous coarsening prior to creep testing. The reason for the thermal instability was pointed out to be the fast cooling necessary to achieve fine lamellae [95]. Furthermore, according to Zhu et al. [96] since fine lamellae are more susceptible to form fine globular structures by spheroidisation, tertiary creep rate increases and the creep life shortens.

The fully lamellar microstructure shows anisotropic creep behaviour depending on the orientation of the lamellae in relation to the stress axis. Parthasarathy et al. [97] showed that a polysynthetically twinned (PST) crystal responded with different creep strength when the external load was applied at 0, 45 and 90° with respect to the lamellar orientation (the PST crystal corresponds to a single grain of a two phase fully lamellar polycrystalline alloy). The creep resistance was highest for 0° and weakest for 45°, which are normally referred to

"hard" and "soft" orientations. In practice grains with the orientation between 30° and 50° are considered to be in the soft mode. The mechanical properties of isotropic polycrystalline titanium aluminides, such as obtained by powder metallurgy processes, are normally inferior to that of a PST crystal oriented in the hard direction.

2.3.2 Creep mechanisms and the influence of stress

In general, the creep resistance of titanium aluminides decreases as the stress and temperature are increased. However, the active creep mechanisms change as a function of the creep conditions. Normally, the creep deformation process requires the emission of dislocations from a source, glide of dislocations in a slip plane until an obstacle is reached and dislocation climb. The creep rate is controlled by the slowest event. The stress exponent (n) can be used for the assessment of active mechanisms at a particular stress and temperature combination. Nevertheless, an unambiguous clarification of the rate controlling mechanisms is rather difficult due to the complexity of microstructures, the large variation of the stress exponent (n) and the continuous increase of the strain rate after the minimum creep rate (absence of steady-state rate). As previously discussed, according to the classic theory of creep, a rough classification of mechanisms is $n = 1$ for diffusion creep, whereas $n \approx 5$ identifies climb and $n > 5$, glide of dislocations as rate controlling process [77].

The influence of stress and temperature on the minimum creep rate is displayed in Figure 6 [10]. Clearly, the stress exponent varies with the applied stress. In the low stress regime ($\sigma_a \approx$ 100 MPa) $n = 1$ is found while in the high stress regime ($\sigma_a > 400$ MPa) n lies between 7 and 10. An increase in the stress exponent with stress might be an indication of a transition from diffusional creep at low stresses to dislocation controlled creep or power law breakdown at high stresses [78]. Additionally, activation energies (Q_c) were reported to vary significantly (230 – 430 kJ mol^{-1}), indicating that different mechanisms might be present during creep and perhaps even overlap [78]. Obviously, at the same stress the minimum creep rate can increase by one order of magnitude if the temperature is only modestly raised, Figure 6.

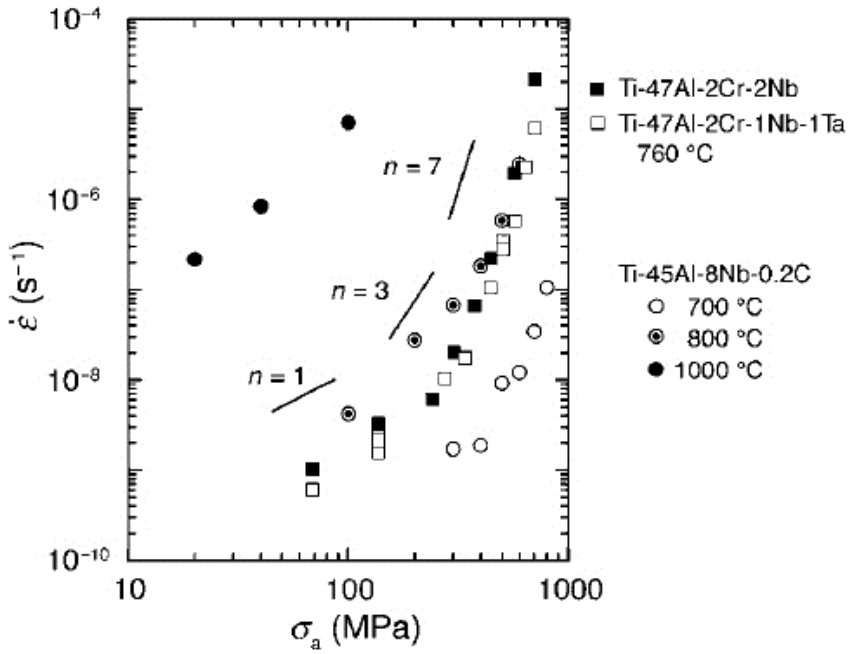

Figure 6 – Minimum creep rate as a function of stress and temperature [10].

Beddoes et al. [78] analysed a wide range of creep data and concluded that a stress-temperature domain exists where the creep rate is climb controlled. The authors also suggested that in case of a fully lamellar microstructure, in the high stress and temperature regime (>200 MPa and >700 °C), dislocation climb is most likely the creep rate controlling mechanism. However, if creep rate is controlled by dislocation climb, a stress exponent $n \approx 5$ and activation energies close to the lattice self-diffusion are expected. Consequently, the high stress exponents from Figure 6 at the high stress regime require elucidation. Several explanations for this disparity have been proposed by Kassner [77]:

- The presence of a back stress due to the lamellar interfaces that trap dislocation segments. This back stress needs to be overcome to initiate dislocation mobility;
- Microstructural instabilities, such as dynamic recrystallisation that are able to increase the strain rate;
- The condition of constant structure creep ($n \geq 8$), since the subgrain size corresponding to a climb controlled creep rate might be larger than the lamellar spacing. Consequently, the lamellar thickness becomes the effective subgrain size.

A technique for the determination of the borders of climb/glide controlled creep rates is the stress reduction test. Zhang et al. [98] determined a stress of 180 MPa at 760 °C as the lower limit for glide controlled creep in the case of the Ti-47Al-4(Nb,W,B) alloy. The studies of Wang et al. [99] found at the same temperature (760 °C) stresses ≥ 241 MPa in slightly different alloys.

In conclusion, the creep mechanisms are highly dependent on the stress and temperature combination, but other microstructural features such as colony size and lamellar spacing, as well as composition also play an important role. The composition can particularly impart a significant change due to the additions of ternary elements. Additions such as Ta, Nb, W, C, N, etc., might influence creep processes by solid solution hardening and/or precipitation, besides an extrinsic effect of changing the lamellar structure, e.g. lamellar spacing. Independent of the mechanisms active, there is enough experimental evidence that the creep behaviour is controlled by dislocation processes (either climb or glide) at high stresses and temperatures.

2.3.3 Primary creep

In the case of most common engineering materials, the characterisation of the secondary creep behaviour is of greater importance for the prediction of creep life and service intervals [100]. However, considering that for many applications, the maximum allowed plastic strain might be limited to <1%, the primary creep region becomes the limiting factor if a material accumulates significant strain during the primary creep regime. In case of titanium aluminides, primary creep is critical since it comprises a significant portion of the allowed plastic deformation.

According to Es-Souni et al. [101], in lamellar microstructures, the primary creep deformation originates from the abundance of interfaces and the high density of dislocations in the starting microstructures. The presence of dislocations at the lamellar interfaces is necessary to compensate for coherency stresses [102], which in turn contributes to hinder dislocation movement along the interfaces creating a high glide resistance at low temperature [10]. As the temperature is increased, the glide resistance decreases and the coherency stresses relax due to thermal activated processes.

As explained by Appel et al. [10], during creep, dislocations are emitted from the lamellar interfaces and move away by glide and climb forming interconnected loops. As this

mechanism gets exhausted, the primary creep rate decreases. This microstructural observation was confirmed by several works that found similar dislocation loops in the γ phase [44,50,91]. Consequently, climb and glide are important mechanisms in primary creep. In fact, Cho et al. [103] measured the activation energy of Ti-45.5Al-2Cr-2.6Nb-0.17W-0.1B-0.2C-0.15Si during primary creep at several strains up to 1% and reported a value of 300 $kJ.mol^{-1}$, which corresponds to a climb controlled process. However, the apparent activation energy increased as a function of strain and saturated at $Q \approx 400$ $kJ.mol^{-1}$, as the minimum creep rate (pseudo steady-state) was reached, possibly indicating a glide dominated creep deformation.

Moreover, not only the pre-existing dislocations but also the lamellar interfaces play a major role in primary creep. As pointed out by Chen et al. [90], the mobility of interface dislocations and the interface morphology greatly influence the primary creep properties. Upon application of stress, the pile-up of dislocations at the interfaces and the corresponding stress fields lead to emission of dislocations loops into the adjacent γ lamellae contributing to primary creep strain. Hsiung et al. [104] also suggested that the primary creep strain is accommodated by mobile dislocations at the interfaces. At low stress, colonies with soft orientation with respect to the applied load were mostly deformed, while at high stress both soft and hard colonies contained deformation substructures.

Lastly, another process that can be present during primary creep is a stress induced phase transformation ($\alpha_2 \rightarrow \gamma$), which causes the thinning of α_2 laths. This transformation might lead to large primary creep strains considering its shear character. Additionally, the formation of new γ laths as the α_2 phase dissolves results in the presence of coarser γ. This in turn leads to more intense dislocation activity, thus further increasing primary creep strain. Seo et al. [42] in a study using a W-containing alloy (Ti-48Al-2W) observed that stress induced phase transformations were more critical in the unaged condition, in contrast to the more stable lamellar structure after aging. Therefore, by eliminating metastable phases through heat treatments prior to creep deformation, a more stable microstructure is achieved and the effect of stress induced phase transformation is decreased [98].

2.3.3.1 The controlling factors

Zhang and Deevi [98] performed an extensive analysis of primary creep in various titanium aluminide alloys. The authors identified a critical dependence of primary creep strain from

the applied stress. Below a critical threshold value, the strain was independent of composition and microstructure, resulting in very low deformations in the order of 0.1-0.2%. However, for stresses above the threshold value, the primary strain increased sharply with stress. Therefore large primary strain becomes of concern in the case of high stresses. The authors also described the factors influencing the threshold stress. The most influencing ones are stress induced phase transformation, twinning and dislocation multiplication.

Stress induced phase transformation, as previously explained, results from an instability of the lamellar structure leading to the dissolution of the α_2 laths. The main reason for these transformations is the sluggish nature of the eutectoid reaction $\alpha \rightarrow \alpha_2 + \gamma$, which is incomplete even after furnace cooling. As a direct consequence, the α_2 phase contains a higher than equilibrium aluminium concentration at the creep temperatures. Diffusion at creep temperatures is rather slow but the transformation is aided by the externally applied stress. Consequently, the presence of a metastable lamellar microstructure, such as in the unaged condition, leads to lower threshold stress.

Morris et al. [50,51] studied the microstructure of deformed specimens after primary creep up to 2% deformation and reported that twinning becomes more pronounced at high stresses. The authors found that at high stresses about 50% of the total strain was due to twinning. The twin interfaces subdivided the γ grains, decreasing the mean free path of mobile dislocations, which possibly raises the threshold stress. This contribution, however, was only present in the case of duplex microstructures.

Dislocation multiplication is also able to raise the threshold stress. The more obstacles dislocations find while gliding, the larger the pile-up of stress and the multiplication of dislocations. As a direct consequence, the increase in dislocation density leads to more obstacles for further glide of dislocations and a higher stress is required to activate dislocation motion, hence the higher threshold stress. Dislocation multiplication is particularly effective with fine lamellar spacing [91].

2.3.3.2 Approaches for the optimisation of primary creep resistance

The primary creep behaviour at high stresses is greatly dependent on the climb and glide of dislocations. Consequently, effective methods for improving primary creep resistance require in principle a decrease of the mobility and generation of dislocations under creep conditions.

The main metallurgical techniques that have been applied in titanium aluminides for the optimisation of primary creep resistance were summarised by Appel et al. [10]:

- Refinement of lamellar spacing;
- Aging treatments of the material prior to testing for the stabilisation of the microstructure and formation of precipitates;
- Prestraining of alloys at higher creep stresses;
- Prestraining in tension at constant strain rate beyond the yield point.

From the above mentioned strategies, the formation of precipitates at the lamellar interfaces, e.g. through aging, is probably one of the most effective. If precipitates are well distributed and have the proper size, they can effectively hinder dislocation glide. Considering the importance of climb in primary creep, the addition of slowly diffusing atoms can also be greatly beneficial. Noteworthy to mention is that the understanding of the exact mechanisms involving primary creep is still under discussion in the literature, especially in regard to the role of the lamellar interfaces.

2.4 Typical alloying additions in titanium aluminides for the improvement of mechanical properties

In thermodynamic equilibrium the aluminium content controls the phase fractions of γ and α_2, as can be seen in the binary phase diagram, therefore, to some extent, it also controls the mechanical properties. However, alloying elements can drastically change the extension of the phase fields and the stability of phases [105].

In the early research of titanium aluminides, a great deal of effort was spent to optimise the ductility, which was achieved by varying the aluminium content [106] and by additions of Cr, Mn and V [107–109]. Refractory elements such as Ta, W, Mo and Nb were reported to greatly increase the mechanical properties by solid solution hardening and/or precipitation strengthening of ordered fine β phase (B2) particles [110–112,45,53]. They are additionally able to stabilise the disordered bcc β phase at high temperatures, which might be helpful for hot working operations (forging, extrusion, etc.) due to its increased plasticity [9].

Light elements such as O, C, N and B are frequently found in titanium aluminides, but they are normally present in low amounts (<1 at.%). Boron additions were introduced for microstructural refinement of cast parts [113,114], while carbon [115,116], oxygen [117] and nitrogen [118] were considered for the improvement of creep resistance through solid solution hardening and precipitation strengthening. Furthermore, Si additions were investigated for the same purpose [119]. In a smaller scale, rare earth elements were considered for refinement of the microstructure and to improve mechanical properties [120–122]. Each group of additions will be shortly described in the following subsections.

2.4.1 Ductilising elements

Three alloying elements have been found to effectively increase the ductility of titanium aluminides: Cr, Mn and V [73]. Cr additions of 2 at.% to binary Ti-48Al were reported to increase the tensile plastic fracture strain up to 2.8% [123]. The authors explained that the effect of Cr resides by the decrease of the α transus temperature, which decreases the volume fraction and stability of the α_2 laths leading to coarse γ regions that can deform unhindered. Additionally Cr reduces the covalency of the Ti-Al bond when it substitutes the aluminium atoms, which favours plastic deformation [124]. The effect of V is believed to be similar to Cr. A value of 2.4% plastic fracture strain was reported in the case of the Ti-47Al-3V alloy [108].

The effect of Mn in increasing the ductility of titanium aluminides is created mainly by two different factors. Firstly, thermal twins are stabilised due to Mn segregation at twin boundaries and secondly the stacking fault energy of the γ phase is decreased [125]. Both factors contribute to enhancing the plasticity because they facilitate deformation by mechanical twinning of the γ phase [126]. Additionally, even though the site occupancy of Mn is dependent on the Ti/Al ratio, in aluminium lean alloys Mn was found to mostly occupy aluminium sites [127]. As a direct result, a weakening of the Ti-Al covalent bond takes place, which also contributes to increased ductility.

2.4.2 Refractory elements

Refractory metals have melting points in the order of 2000 °C and thus are extraordinarily resistant to heat. Several refractory metals such as Ta, W, Mo and Nb have already been

studied as alloying elements for titanium aluminides [128–131]. Since the stability of phases is strongly dependent on chemistry, the additions of refractory elements might cause drastic changes in the phase boundaries [6,105]. All refractory elements mentioned act as β phase stabilisers. Besides expanding the β phase field, the formation of additional phases might take place, depending on the solubility of each element and processing conditions. Furthermore, the β phase at low temperatures exists in an ordered variant (B2 structure), which can cause embrittlement depending on morphology and distribution, especially if it decomposes into other products such as ω phases [132]. However, in general, refractory elements are very attractive additions because they can facilitate processing or optimise high temperature properties such as creep and oxidation resistance.

In titanium aluminides, addition of Ta in the range of 7 at.% (Ti-45Al-7Ta) was shown to improve creep resistance at 800 °C in a fully lamellar microstructure prepared by casting [131]. The authors explained the increase due to the low diffusivity of Ta but also identified the precipitation of a Ta-containing τ phase at the colony boundaries, which was formed during annealing. Lapin et al. [133] investigated a similar alloy, Ti-46Al-8Ta, and also found the presence of the τ phase in specimens after creep testing at 700 °C. The greatest advantage of large additions of Ta, however, is the reduced diffusivity that allows massive γ transformation with slower cooling rates. With the proper heat treatment, fine convoluted microstructures could be achieved [134].

W additions to titanium aluminides have been reported to improve strength and creep resistance significantly [135,136,130,137,138]. This was explained on the basis of solid solution hardening, reduced diffusivity and due to the presence of small ordered β phase precipitates (B2). The latter requires a solution treatment followed by aging [112]. As described by Yu et al. [139], the B2 precipitates nucleate preferentially at ledges located in the α_2/γ interfaces, which greatly hinders dislocation glide. The authors confirmed that the nucleation barrier at ledges was lower due to W enrichment at those areas. Another important microstructural effect of W addition is the refinement of lamellar spacing and colony size that increases hardness and tensile strength [138].

Mo was initially evaluated to improve oxidation resistance of binary titanium aluminides [140] and to increase strength [141]. Recently, Mo additions have been considered for the optimisation of the hot working processing. Mo is a strong β phase stabiliser and leads to a large volume fraction of the softer β phase at high temperature [142], which facilitates plastic deformation. In fact, Imayev et al. reported superplastic elongations in the order of 200% at

high temperatures (>900 °C) with alloys containing Nb and Mo [143]. Despite the presence of retained β phase, creep properties might also profit from the presence of Mo. Similar to W additions, Mo promotes the precipitation of ordered β phase (B2) with the proper heat treatments [144,46,145]. However, the amount of Mo addition is critical and depending on the processing conditions, if not optimised, might lead to poor mechanical properties. Since Mo is a heavy atom, it makes phase transformations sluggish and that hinders the formation of the equilibrium lamellar structure during heat treatment [146].

Nb is one of the most frequently found alloying elements in titanium aluminides. It is present in state-of-the-art alloys such as TNB Ti-(42-45)Al-(5-10)Nb-(0-0.8)B [142,147,53] and TNM Ti-(42-44)Al-(3-5)Nb-(0.1-2)Mo-(0.1-1)B [9,148,149]. Nb additions were studied for improving the oxidation resistance [150], but were also found to greatly increase the mechanical properties at room and high temperatures [53].

The effect of Nb on the mechanical properties is not straightforward. Many reports of improved strength by Nb additions have been published [111,151,27,152] and solid solution hardening is often mentioned. However considering that Nb mostly occupies titanium sites [153,127] and that the atoms size misfit is about 0.2 % [75], there are other factors playing a role, as well. Kim et al. [154] studied sheets of Ti-45Al-5Nb and found that actually the strength of Ti-45Al-5Nb and Ti-45Al were similar in the same thermomechanically processed conditions. However, the main contribution of Nb in strengthening of the as-rolled sheets was due to unstable structures (originated from a shift in the phase boundaries in comparison to binary alloys), grain boundary strengthening and solution hardening. The latter also had an extra contribution considering that Nb additions reduced the aluminium content in the γ phase by 2.8 at.%. As a direct result, the vacant aluminium sites were occupied by titanium, enhancing the solid solution hardening effect. Additionally the decreased aluminium content caused an increase in the oxygen solubility, possibly further increasing hardening by oxygen interstitials. Lastly, there is also a strengthening contribution of Nb due to structural refinement [53,129]. The improved creep resistance was explained to originate from an increase in the stress required to initiate dislocation glide and twinning [155]. That is a combined result of basically two factors, the reduced dislocation climb rate due to the low diffusivity of Nb and the lower stacking fault energy, which also hinders dislocation climb [156].

2.4.3 Light elements

Strengthening through precipitation of hard particles is one of the most efficient ways to improve primary creep resistance. Precipitates are formed due to solid state transformations during aging and at creep temperatures as well. Common elements that form precipitates are C, O, B, N and Si, but β stabilising elements can also trigger precipitation, as discussed in the latter subsection.

The eutectoid transformation of the α phase into $\alpha_2 + \gamma$ is known to be sluggish, normally leading to a volume fraction of the α_2 phase that is not at equilibrium. Therefore the α_2 phase decomposes into γ in order to reach a balance. Since the solubility of interstitials is higher for the α_2 phase, a decrease of the α_2 volume fraction results in precipitation of interstitials in the γ phase, which often occurs by heterogeneous nucleation [157]. The precipitates are usually located at the lamellar interfaces and consequently the dislocations are subjected to an additional gliding resistance, which greatly increases resistance to primary creep but can cause lower ductility at room temperature.

Carbide precipitates in titanium aluminides have been widely studied for strengthening [158,159,115,160–162]. Carbides are typically found in two different phases: perovskite "P" (Ti_3AlC) and hexagonal "H" carbides (Ti_2AlC). Both have different formation temperatures, 750 °C and 800-900 °C, respectively. P type carbides have usually a rod-like morphology, although they can also exist as plates for larger precipitate sizes. On the other hand, the H type carbides are usually plate-like and they are larger and coarser because precipitation takes place at higher temperatures and longer aging times. Consequently the strengthening effect is not as pronounced as for the smaller P carbides. The effect of nitrogen is similar to carbon as described by Tian et al. [159]. Interstitial nitrogen forms either P-type (Ti_3AlN) or H-type (Ti_2AlN) nitrides and they both have different formation temperatures. Additionally they have similar morphology as the carbides and are prone to overage softening after the H-phase is formed [163].

The effect of oxygen on high temperature properties of titanium aluminides is difficult to assess. Kawabata et al. [117] conducted a systematic study on binary alloys Ti-(50, 53, 56)Al with different oxygen contents (up to 0.69 at.%) and showed that the oxygen addition on Ti-50Al could increase the yield stress 1.5 times, nevertheless this effect was not so strong for the Al rich alloys. Additionally α-Al_2O_3 was precipitated in the Ti-(53, 56)Al but in all cases

a grain refinement effect was found to take place, which makes it difficult to isolate the variables influencing the strengthening effect.

Boron has a very low solubility in all binary Ti-Al phases and is present in different forms of borides (MB, MB_2 and Cr-enriched M_2B) [164], which can exist in various morphologies such as flakes, plates and needles, depending on the composition, solidification path and rate and on the fabrication method [165]. Borides are classically known for microstructure refinement, especially of cast alloys [165,64,114]. Since borides are normally not precipitated at the γ/γ and α_2/γ interfaces [166] they might not be efficient for the improvement of creep properties, nevertheless at the proper volume fraction and distribution they might have a positive effect [167].

Silicon addition to titanium aluminides leads to the formation of the hexagonal ζ phase Ti_5Si_3. Although controversially discussed, the effect of silicides is usually considered beneficial for the creep properties [88,167]. Noda et al. [119] studied the effect of Si additions on a fully lamellar Ti-48Al-1.5-Cr-(0.2-0.65)Si alloy and found that the ζ phase was nucleated at the lamellar interfaces, which in turn increased the creep resistance up to 850 °C due to the dispersion strengthening effect. However, Du et al. [168] showed that addition of 0.3 at.% Si to the alloy Ti-47Al-2Cr-1Nb-0.8Ta-0.2W-0.15B was not as beneficial as previously discussed. The authors explained that due to the parameters of the fabrication process used (extrusion) the Si atoms remained in solid solution, which promoted dislocation climb by the increased vacancy density.

2.4.4 Rare earth elements

Rare earth elements have been used to refine the microstructure and increase the strength of many different materials such as magnesium, steels, aluminium, etc. Nonetheless the use of rare earth elements in titanium aluminides is still a bit unusual and few published works investigated their effect. The group around K. Xia studied the effect of rare earth additions to cast Ti-44Al but their research mostly concerned Gd additions [120,169–171,122].

Gd was studied with the objective of refining the microstructure [171,172] and also to improve creep resistance through precipitation strengthening [122]. At first, Gd causes the formation of a phase that was tentatively identified to be an oxide (Gd_2TiO_5) with finger shaped morphology in the as-cast condition. The presence of finely dispersed Gd_2TiO_5 and

the possible segregation of Gd to colony boundaries were pointed out as possible explanations for the refinement of the microstructure [120]. After annealing different morphologies were identified including particulates, plates and rods, which were much larger in size than particles that could effectively increase creep resistance. In a later study Xia et al. reported that by addition of 0.15 at.% Gd to a fully lamellar Ti-44Al-1Mn-2.5Nb alloy, they were actually able to increase the creep strength for the same lamellar thickness in comparison to the Gd free version [122]. However, the particles that were actually responsible for increasing creep resistance were precipitated during the creep test and were much smaller (tens of nanometres). Additionally these small particles were often found to be located at dislocations and interfaces. The authors explained that the secondary Gd-rich particles were most probably dynamically precipitated as the α_2 phase was dissolved.

2.5 Processing of titanium aluminides by Metal Injection Moulding (MIM)

Shaping of powders is an important step in powder metallurgical processes. Parts can be made successfully out of powder by many different techniques including press and sinter, Hot Isostatic Pressing (HIP), extrusion, Metal Injection Moulding (MIM), etc. The particular choice of each process is highly dependent on the materials being processed and geometry of the parts. Yet, the ultimate factor is the compromise between costs and desired properties, since different techniques can be used to accomplish the same outcome.

MIM is a shaping process for metals and alloys that was adapted from the plastics technology. It combines the flexibility of plastic injection moulding in terms of forming with the superior properties of nearly full dense metal parts at the end of the process. The remarkable feature of this technique is the possibility of producing high performance components with complex geometries at low costs [173].

Additionally, MIM offers the advantage of near-net shape production. This special feature decreases the need for secondary operations (like grinding, drilling and boring), hence costs. MIM is also able to deliver a much finer and more homogeneous microstructure than competing conventional techniques like die casting, for example.

The first step of the process is mixing of metallic powders and binders, which are later homogenised and pelletised forming a homogeneous blend called feedstock. The material is

subsequently heated to a temperature that allows plastic flow of the mass by controlled injection of the melt into a cavity where it cools to the desired form. The parts undergo a process for removal of the binder (debinding) that is usually carried out in two steps. Firstly, the low melting point components are removed in a bath of solvents and later the remaining of the binder is removed thermally. The final step of the process is sintering. At this stage the parts are densified and shrink to the final size. At the end of the process, high quality parts are produced within tight geometrical tolerances.

The MIM process is highly dependent on the materials being handled. In case of more sensitive and reactive metals such as titanium and its alloys, MIM is still under development or industrially employed in a much smaller scale than more traditional materials, e.g. steels. Only a few research works dealing with parameter studies for MIM of titanium aluminides have been published [38,32–34,16,35,39,36,40].

Despite the early reports of MIM-TiAl in Japan [174,175], it seems that significant results were not disclosed before the year 2000. One of the first accounts of adequate mechanical properties was perhaps from Terauchi et al. [38] also in Japan. The authors achieved a UTS of 322 MPa and ductility of around 1.8% at room temperature with the alloy Ti-47.4Al-2.6Cr. The residual porosity was in the order of 2%, which was accomplished with sintering at 1365 °C for 2 hours in vacuum. These results proved the feasibility and further emphasised the encouraging potential of processing titanium aluminides by MIM.

In 2001-2002, Gerling et al. [32,33] confirmed the feasibility of MIM-TiAl by successfully preparing the Ti-47-4(Nb, Mn, Cr, Si, B) alloy with porosities <5%, however the mechanical properties showed a high scatter with UTS between 200-400 MPa. The authors explained that the main contributing factors were the oxygen levels and the irregular porosity distribution (porosity nests). Consequently, as the authors stated, these limiting factors should be optimised for achieving more reliability on the mechanical properties.

In a later study Gerling et al. [34] were able to optimise the sintering step achieving porosities <4% and UTS of around 350 MPa, which are still a bit lower than a HIP compact of the same alloy, namely Ti-47Al-4(Nb,Mn,Cr,Si,B). A few years later, Y. C. Kim et al. [16] published a study of binary Ti-48Al processed by MIM. The authors achieved porosities <2% using extremely long (30 h) sintering times in combination with a pre-sintering step but no mechanical tests were conducted. One year later, Zhang et al. [35] investigated MIM of a

high Nb containing alloy (Ti-45Al-8.5Nb-0.2W-0.2B-0.002Y) achieving UTS of 336 MPa with a porosity of nearly 3% by sintering at 1480 °C during 3 hours.

Only recently in 2012, the group around T. Ebel, was able to successfully process a titanium aluminide alloy, Ti-45Al-5Nb-0.2B-0.2C, by MIM with extremely low porosity (<1%) and high strength at room temperate (UTS 630 MPa). Up to this date, these results are the best mechanical properties ever reported for a MIM-TiAl alloy, with strength values in the range of the as-cast material [37]. The authors achieved the high room temperature strength by conducting sintering at a near solidus temperature (1500 °C) in vacuum or argon for 1-2 hours, which also led to fairly low oxygen and nitrogen contents. These new findings and the increasing demand for lightweight energy-saving materials that can be inexpensively produced is a constant driving force for the further development and optimisation of the MIM process.

3. Materials and experimental procedure

3.1 Materials

All starting materials used throughout this work were in the form of metallic powders (pre-alloyed and elemental). The materials used for the preparation of arc melting specimens were the only exception, in which metal pieces were used instead of powders.

The specimens prepared for this research work can be divided in three different groups and classified in accordance to the stage of alloy development:

- Screening Part I: firstly, a series using TNB-V5 (Ti-45Al-5Nb-0.2B-0.2C, all compositions mentioned are in at.%) as master alloy was prepared and evaluated. In Screening Part I, the following elements were varied and/or introduced: W, Ta, Nb, Mo, Cr, Si and Gd.
- Screening Part II: in a second stage of screening, specimens were prepared with Ti-48Al-3Nb-0.2B-0.2C and Ti-48Al-5Nb-0.2B-0.2C as master alloys. In Screening Part II, the following elements were varied and/or introduced: Mo, Ta, Si and Gd.
- Final Alloy Candidates: ultimately, the compositions tested were narrowed down and the starting pre-alloyed powder Ti-44.5Al-3Nb-1Mo-0.2B-0.2C was used. In the Final Alloy Candidates, the following elements were varied and/or introduced: Mo, Si and Gd.

3.1.1 Arc melting

The master alloy Ti-49Al-0.4C supplied by GfE GmbH, Nürnberg, Germany together with high purity metals in different forms were used to prepare arc melted specimens, as displayed in Table 1.

Table 1 – Materials for arc melting.

Material	Manufacturer	Purity	Form
Ti-49Al-0.4C	GfE	--	Ingot
Nb	Alfa Aesar	99.6 %	Turnings
Mn	Alfa Aesar	99.9 %	Chips
Mo	Alfa Aesar	99.95 %	Wire
Ti	Alfa Aesar	99.6 %	Sponge
Al	Alfa Aesar	99.7 %	Shot

In order to create references specimens with cast microstructures and for initial screening purposes, a series of 5 different alloys were prepared by arc melting. The alloys studied included variations in elements that were already present in the composition of TNB-V5, namely an alloy with higher niobium content and alloys with lower and higher aluminium levels. Two different quaternary alloys were also prepared including the introduction of one slowly diffusing element (Mo) and one ductilising element (Mn).

Table 2 – Specimens prepared by arc melting

Concept	Alloy	Composition
Reference	TNB-V5	Ti-45-5Nb-0.2B-0.2C
Slow diffusion	+Mo	Ti-45Al-5Nb-**1.5Mo**-0.2B-0.2C
Ductilising	+Mn	Ti-45Al-5Nb-**1.5Mn**-0.2B-0.2C
Base alloy variation	+Nb	Ti-45Al-**8Nb**-0.2B-0.2C
	-Al	Ti-**44Al**-5Nb-0.2B-0.2C
	+Al	Ti-**47Al**-5Nb-0.2B-0.2C

3.1.2 Metallic powders

Four different base systems were used as master alloys (Table 3), which were prepared by gas atomisation of pre-alloyed rods using the EIGA (Electrode Induction Melting Gas Atomisation) technique. The pre-alloyed rods at the exact composition of the different base alloys were supplied by GfE GmbH, Nürnberg, Germany. The rods were placed inside a purged container with an induction coil at one end. The tip of the rod was melted and the droplets passed through a gas nozzle, where they were atomised by an argon jet. The powders were later sieved under argon and only the fine fraction of <45 μm was used for the specimen preparation. Details regarding the atomisation technique can be found here [17].

Table 3 – Base systems and their interstitial levels.

Base system	Interstitials	
	Oxygen (μg/g)	Nitrogen (μg/g)
Ti-45Al-5Nb-0.2B-0.2C (TNB-V5)	845 ± 53	184 ± 17
Ti-48Al-5Nb-0.2B-0.2C	473 ± 16	145 ± 22
Ti-48Al-3Nb-0.2B-0.2C	562 ± 31	123 ± 15
Ti-44.5Al-3Nb-1Mo-0.2B-0.2C	708 ± 14	374 ± 28

In order to achieve the desired composition, various elemental powders were added to the different base systems during feedstock preparation (Table 4). All powders were relatively fine with an average particle size in the order of 50 μm or smaller. The only exception was gadolinium silicide that was mainly composed of small irregular pieces.

Table 4 – Elemental powders.

Material	Manufacturer	Purity	Size
Aluminium	Alfa Aesar	99.5 %	<45 µm
Boron	H.C. Starck	95 %	<1 µm
Chromium	Sigma Aldrich	>99%	<45 µm
Gadolinium Silicide ($GdSi_2$)*	Alfa Aesar	99.9 %	6 mm and down
Gadolinium**	--	--	--
Manganese	MHC	99.7 %	50 µm
Molybdenum	MHC	≥99.95 %	50 µm
Niobium	MHC	≥99.9 %	50 µm
Silicon	Alfa Aesar	99.5 %	<45 µm
Tantalum	MHC	99.97 %	50 µm
Titanium	TLS	99.7 %	<45 µm
Tungsten	Alfa Aesar	99.9 %	<45 µm

*** Gadolinium silicide was crushed into powder using a mortar and pestle.**

**** Gadolinium powder was prepared by milling small pieces of an ingot.**

3.1.3 Binder system

The binder system used in this study has been demonstrated to work well in MIM of titanium alloys leading to adequate levels of impurities [176,177]. It was prepared with a mixture of three different components: paraffin wax (60 wt.%), stearic acid (5 wt.%) and polyethylene vinyl acetate, EVA (35 wt. %).

3.1.4 Screening of alloying elements Part I: TNB-V5 as master alloy

Screening of alloying elements started with TNB-V5 as master alloy that was used to prepare the main series of alloy variations displayed in Table 5. TNB-V5 was also the reference material for all the experiments conducted, independent of the screening phase. Two different concepts were considered based on the amount of β stabilising elements added, the high β and the low β series. Within each series it is possible to find sub variations that included three different basic principles:

- addition of slowly diffusing refractory elements;
- addition of elements that can cause precipitation of third phases; and
- addition of a ductilising element (Cr).

Table 5 – Main series of alloy variations from Screening Part I.

Main Series	Concept	Alloy	Composition
Low β	Reference	TNB-V5	Ti-45Al-5Nb-0.2B-0.2C
	Solid solution hardening/Slow diffusion	+W +Ta +Mo	Ti-44.5Al-3Nb-0.7W-0.2B-0.2C Ti-44.5Al-3Nb-2Ta-0.2B-0.2C Ti-44.5Al-3Nb-1Mo-0.2B-0.2C
	Precipitation	+Si +Gd	Ti-44.5Al-5Nb-1Si-0.2B-0.2C Ti-44.5-3Nb-(0.2-0.5)Gd-0.2B-0.2C
	Ductilising	+Cr	Ti-44.5Al-5Nb-1Cr-0.2B-0.2C
High β	Solid solution hardening/Slow diffusion	+Nb +W +Ta +Mo	Ti-44.5-8Nb-0.2B-0.2C Ti-44.5Al-5Nb-1W-0.2B-0.2C Ti-44.5Al-5Nb-3Ta-0.2B-0.2C Ti-44.5Al-5Nb-1.5Mo-0.2B-0.2C
	Ductilising	+Cr	Ti-44.5Al-8Nb-1Cr-0.2B-0.2C

3.1.5 Screening of alloying elements Part II: Ti-48Al-3Nb-0.2B-0.2C and Ti-48Al-5Nb-0.2B-0.2C as master alloys

The second part of the screening of alloying elements was conducted with different master alloys. In order to decrease the amounts of elemental powders necessary for adjustments of compositions and to completely eliminate the necessity for the addition of pure aluminium, the compositions Ti-48Al-3Nb-0.2B-0.2C and Ti-48Al-5Nb-0.2B-0.2C were used. In comparison to TNB-V5, the aluminium content was higher from the start, which enabled the addition of elemental powders of different alloying elements without the need to add elemental aluminium. The different niobium values came out due to the different main series (high β and low β), thus minimising the amounts of elemental niobium required to balance the compositions.

Similar main series as before containing low β and high β candidates were prepared. After selecting the promising candidates based on the results of compression creep test, many of the alloys previously investigated were discarded. Combining the elements that brought the greatest increase in compression creep resistance, three new compositions were investigated, Ti-44.5Al-3Nb-1Mo-1Si-0.2B-0.2C, Ti-44.5Al-3Nb-1Mo-0.2Gd-0.2B-0.2C and Ti-44.5Al-3Nb -1Mo-1Si-0.2Gd-0.2B-0.2C. Additionally, a new way of introducing Gd was employed. Instead of adding pure Gd, as in Screening Part I, a compound containing both Gd and Si was used ($GdSi_2$). Therefore the contaminations that came from the high reactivity of pure Gd could be avoided.

Table 6 – Main series of alloy variations from Screening Part II.

Main Series	Concept	Alloy	Composition
Low β	Reference	TNB-V5	Ti-45-5Nb-0.2B-0.2C
	Solid solution hardening/Slow diffusion	+Mo	Ti-44.5Al-3Nb-1Mo-0.2B-0.2C
	Precipitation	+Gd	Ti-44.5-3Nb-0.2Gd-0.2B-0.2C
		+Si	Ti-44.5Al-5Nb-1Si-0.2B-0.2C
	Solid solution hardening/Slow diffusion + Precipitation	+Mo+Si	Ti-44.5Al-3Nb-1Mo-1Si-0.2B-0.2C
		+Mo+Gd	Ti-44.5Al-3Nb-1Mo-0.2Gd-0.2B-0.2C
		+Mo+Si+Gd	Ti-44.5Al-3Nb-1Mo-1Si-0.2Gd-0.2B-0.2C
High β	Solid solution hardening/Slow diffusion	+Ta	Ti-44.5Al-5Nb-3Ta-0.2B-0.2C

3.1.6 Final Alloy Candidates: Ti-44.5Al-3Nb-1Mo-0.2B-0.2C as master alloy

Based on compression creep results after Screening Part II, three candidates were selected to be further investigated. These Final Alloy Candidates were also prepared by MIM and tensile creep tested under different loading conditions. A new master alloy with a composition very close to the final candidates was prepared (Ti-44.5Al-3Nb-0.2B-0.2C), so the difficulties faced when adding elemental powders could be minimised. Although the additions of Si and

Gd were still in the form of elemental powders, no elemental Al was added. Considering that only little amounts of Si and Gd were necessary, the variation of the Al content was negligible.

Table 7 – Final Alloy Candidates.

Main Series	Concept	Alloy	Composition
Low β	Reference	TNB-V5	Ti-45-5Nb-0.2B-0.2C
	Solid solution hardening/Slow diffusion	+Mo	Ti-44.5Al-3Nb-1Mo-0.2B-0.2C
	Solid solution hardening/Slow diffusion + Precipitation	+Mo+Si +Mo+Si+Gd	Ti-44.5Al-3Nb-1Mo-1Si-0.2B-0.2C Ti-44.5Al-3Nb-1Mo-1Si-0.2Gd-0.2B-0.2C

3.2 Specimen preparation

Three different techniques were used to prepare specimens according to the stage of alloy development (Table 8). In the following subsections each particular technique will be described.

Table 8 – Summary of specimen preparation techniques.

Preparation method	Type of specimen	Main purpose
Arc melting	Buttons	Reference of cast materials, compression creep screening
Uniaxial Pressing of feedstock	Cylinders	Sintering experiments, compression creep screening
Metal Injection Moulding	Tensile and tensile creep	Mechanical characterisation

3.2.1 Arc melting

Arc melting was conducted in a water cooled copper hearth under argon atmosphere using the Edmund Buehler D-7400 (Tübingen) system. Firstly, the chamber was purged 5 times with argon to avoid contamination, then backfilled with 800 mbar of argon. The weighed pieces of metal were melted via an electric arc and solidified in a button-like shape of approximately

30 g weight. Later the button was turned around and remelted and this process was repeated at least 6 times to ensure homogeneity.

For the preparation of compression creep specimens, the solidified buttons were cut parallel to the cooling direction (in the direction perpendicular to the cooled copper hearth) and ultimately ground into cylinders of 8 mm height and 4 mm diameter. Specimens were taken from the middle of the button after removing the top and bottom part, which could contain residual porosity.

3.2.2 Feedstock preparation

The mixture of binder system and metallic powders (feedstock) was prepared in two different ways, depending on the desired amount of feedstock. The end result, however, is assumed to be the same independent of the preparation method. For the screening experiments a small amount of feedstock of approximately 20 g was necessary, while for MIM larger amounts in the order of 500-900 g were required.

Small amounts of feedstock for Uniaxial Pressing were prepared by mixing the pre-alloyed powder together with elemental powders and the binder system using a tumbler mixer model Thinky ARE-250. In the mixtures 8 wt.% binder was added. Firstly, the components of the feedstock were weighed and sealed in a stainless steel can that was filled with argon. The can was subsequently heated to approximately 120 °C and after a short dwelling time, the binder system was melted. Afterwards the can was placed in the tumbler mixer and stirred at 2000 rpm for 2.5 minutes. The whole process was repeated 4 times totalising 10 minutes of mixing time in order to assure feedstock homogeneity.

Feedstock for MIM was prepared by mixing the pre-alloyed and elemental powders with the binder system using a double Z-Blade mixer (FEMIX KM 0,5K). The feedstock was mixed at 120 °C under an argon atmosphere for 2 hours and subsequently homogenised by extrusion through the injection moulding barrel. Finally the feedstock was pelletised by means of a cutting mill. The binder system was applied at a fraction of 10 wt.%. This increased binder content for the feedstock for MIM was selected because it leads to a better surface quality in sintered parts [177].

3.2.3 Uniaxial Pressing (UP)

Cylinders of 8 mm and 4 mm diameters were prepared by Uniaxial Pressing of feedstock using a hydraulic hand press from the company Enerpac. Firstly the tools (matrix and stamps) were heated up to approximately 70 °C with a laboratory hot plate from Jenway model 1100. The feedstock was then separately heated to around 120 °C. As the feedstock became plasticised, it was inserted inside the matrix cavity and uniaxially pressed from both sides with a pressure of approximately 400 MPa. After pressing, the whole system (tool and specimen) was cooled down until the temperature reached 30-40 °C. Lastly the pressed specimen was manually extracted. Specimens in the as-pressed condition were about 10-12 % larger in length than the final sintered specimens.

3.2.4 Metal Injection Moulding (MIM)

Injection moulding was conducted using an Arburg machine Allrounder 320S. Different injection parameters were necessary depending on the geometry of the specimens; nonetheless the parameters were optimised to minimise the chance of moulding defects. The as-moulded green specimens were also subjected to non-destructive testing by X-Ray radiography to ensure the absence of defects. Similarly to pressed specimens, green specimens were about 10-12 % larger in length than sintered specimens. Two different pre-forms were moulded for tensile creep and regular tensile specimens, Figure 7 (a) and (b) respectively.

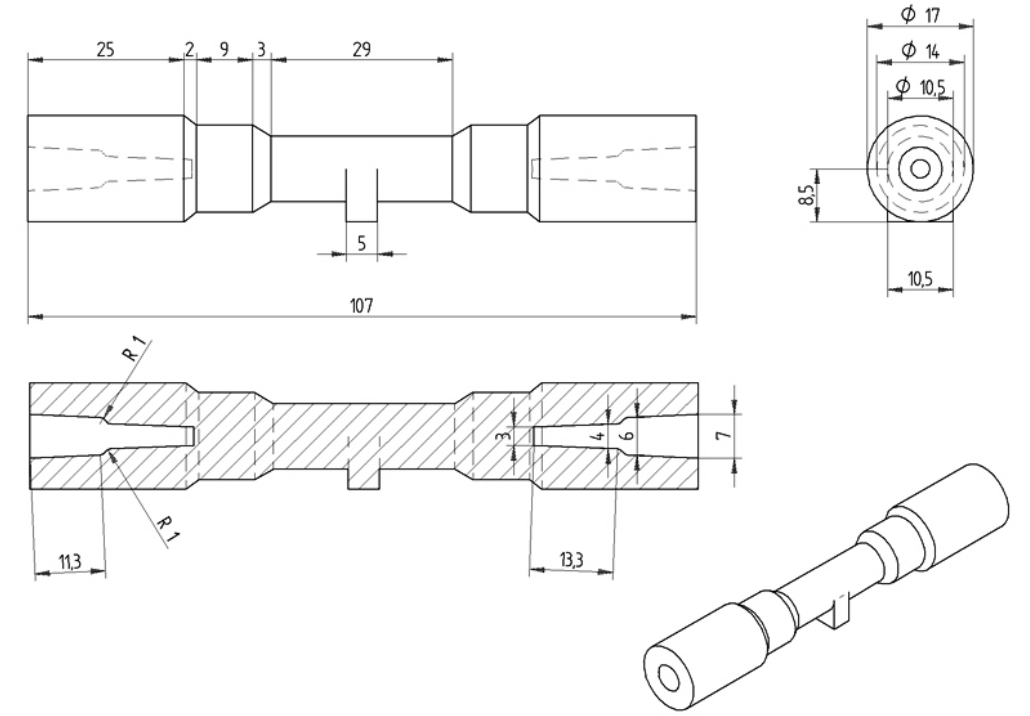

(a)

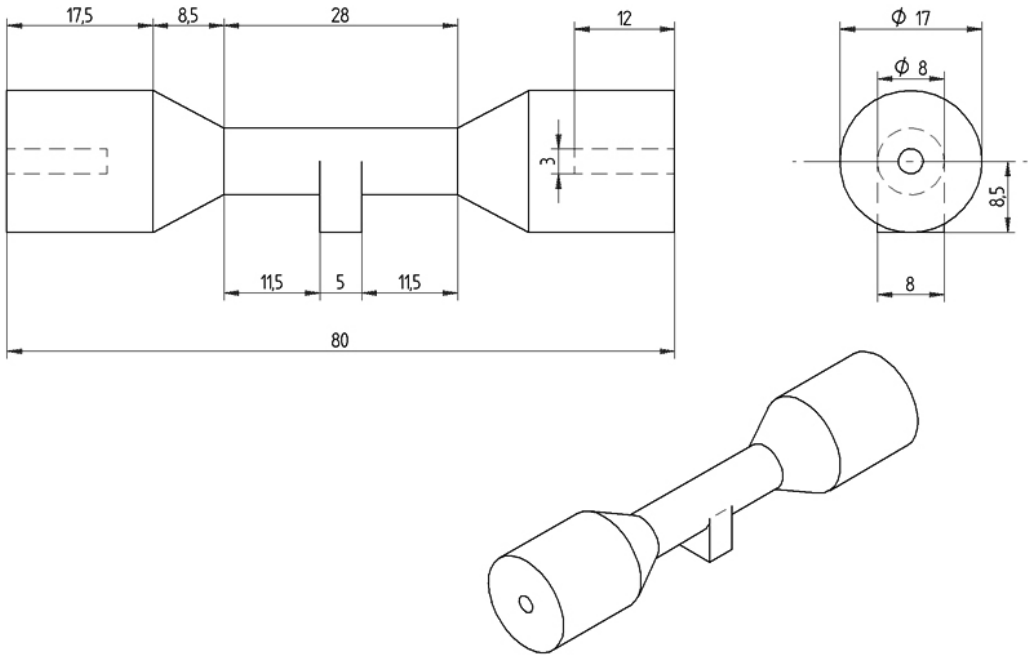

(b)

Figure 7 – Pre-forms of specimens prepared by MIM. (a) Tensile creep specimen. (b) Tensile specimen. Dimensions are from the sintered parts in millimetres.

3.2.5 Debinding and sintering

Debinding was conducted in two steps. Firstly the low melting point components (wax) were extracted chemically by a hexane bath at 40 °C for variable times of 15-30 hours, depending on the diameter of the specimens. Longer times were applied in the case of the tensile and tensile creep pre-forms due to the larger cross sections. Afterwards the remaining of the binder was thermally removed inside the sintering furnace at 5 mbar argon pressure by a sequence of controlled heating rates and holding times at specific temperatures (Figure 9).

Sintering was conducted following the debinding cycle in the same furnace run. The structure of the sintering furnace consists of a vertical retort where rings of molybdenum were stacked. Molybdenum plates coated with yttria are placed between the rings, which served as support for the specimens during debinding and sintering, Figure 8. The furnace also has hollow water cooled walls and base to protect the steel frame. The heating elements are made of tungsten and are positioned around the retort. A cold trap for the binder was placed at the bottom in front of the vacuum pump connectors to catch the remains of the binder.

Figure 8 – Vacuum sinter furnace from Xerion.

Different sintering temperatures and times were necessary depending on the chemical composition of the specimens. The range of temperatures and sintering times applied was 1450 to 1520 °C and 2 or 4 hours. The sintering atmosphere applied was high vacuum of approximately 10^{-4} mbar at the sintering temperature. An example of a sintering profile is displayed in Figure 9. This profile is a result of several preliminary experiments and was designed to ensure proper removal of the binder and minimise residual porosity. The actual cooling rate of 100 °C per minute is only valid from the sintering temperature until approximately 1000 °C, after that it decreases gradually.

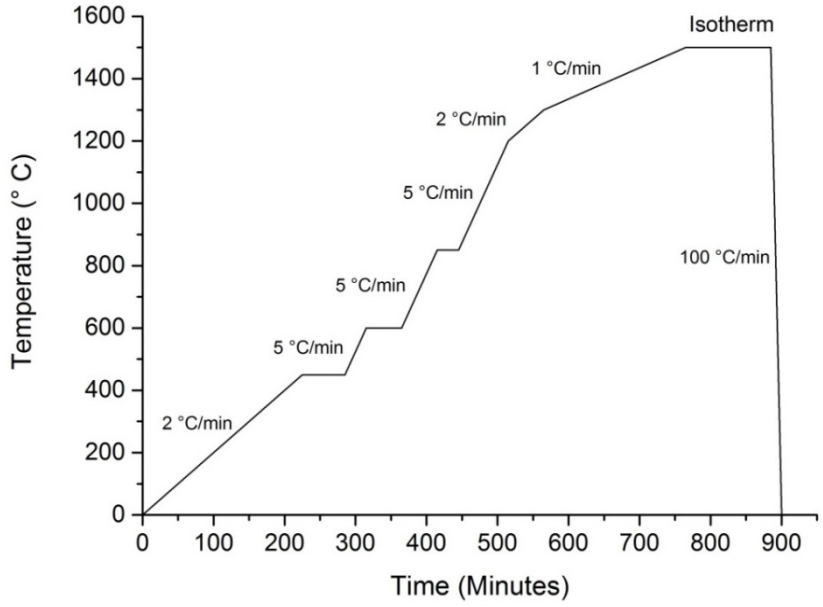

Figure 9 – Sintering profile with sintering temperature at 1500 °C for 2 hours. The cooling rate of 100 °C/min is only true from the sintering temperature to approximately 1000 °C.

3.3 Density measurements

Density measurements were carried out using the immersion method, as described in the ASTM B311. Based on measurements of the weight of the specimen in air and also completely immersed in a known liquid (pure ethanol was used) it was possible to determine the density of the specimens. The measurements were performed using an analytical scale from Sartorius model LA230S. The pieces used for the measurements were cut from representative volumes of the bulk sintered part.

3.4 Microstructural and structural characterisation

Sintered specimens were subjected to metallographic preparation prior to microstructural characterisation. Representative areas of the specimens were selected and mechanically cut with a precision cutting machine Isomet Plus from Buehler. The pieces were afterwards embedded in resin, stepwise ground with increasing grit from 360 to 2000 and lastly mechanically polished for 30 minutes using an Active Oxide Polishing Suspension (OPS) of silicon dioxide with 1 μm particle size from Struers. Grinding and polishing were conducted using a Buehler machine model Motopol 2000.

Porosity and colony size measurements were carried on metallographic polished surfaces with usually 4 different pictures taken with a magnification of 200 from different areas of the specimen. An optical microscope Olympus PMG-3 and the image analysis software AnalySIS Pro were used for picture taking and analysis. Backscattered and secondary electron images were recorded using the scanning electron microscope DSM962 from Zeiss.

The impurity levels were measured by means of a melt extraction technique (LECO System). The model TC – 436AR was used for oxygen and nitrogen and the CS – 444 for carbon.

Structural characterisation was conducted using a D5000 Diffractometer from Siemens. Prior to X-Ray Diffraction (XRD) measurements, specimens cut from the MIM pre-forms were mounted in resin and ground to 2000 grit. XRD was carried out using a Cu Kα radiation and a graphite secondary monochromator. The 2θ scanning was recorded from 10 to 90 degrees with a step size of 0.2 degree. The specimen was rotated at 40 rpm during the measurement. Quantitative analysis was conducted via comparison of the integrated area of the peaks.

High-energy X-ray diffraction experiments were carried out at the HZG beamline HEMS at the Deutsches Elektronen-Synchrotron (DESY). Samples with a diameter of about 4 mm were measured in transmission geometry using a beam cross section of 0.5 mm × 0.5 mm. High-energy X-Rays having a photon energy of 87 keV, corresponding to a wavelength of $\lambda = 0.1425$ Å, were used to penetrate the specimens. The resulting Debye-Scherrer diffraction rings were recorded on a Mar345 image plate detector with an exposure time of 4 s. Conventional diffraction patterns were generated by an azimuthal integration of the Debye-Scherrer rings.

3.5 Thermal analysis

Thermal analysis measurements during this research work were mainly Differential Scanning Calorimetry (DSC), although in the case of TNB-V5 dilatometry experiments were also conducted.

Differential Scanning Calorimetry measurements were carried out in a Netzsch DSC404 Pegasus calorimeter on pre-alloyed and on powder mixtures of pre-alloyed + elemental powders. The powder mixing was conducted using a tumbler mixer Thinky ARE-250 at 2000 rpm for 5 minutes. From the total amount of powders mixed (approximately 10 g), smaller parts of about 60 mg were used to fill the alumina DSC crucible. All DSC measurements were recorded from room temperature until the melting point. The heating rate applied was 20 K/min.

Dilatometry experiments were conducted using a vertical Linseis dilatometer model L70/2171. Sintering experiments were conducted on uniaxially pressed specimens with a similar profile as shown in Figure 9. The cylinders had diameters of about 4 mm and lengths around of 8 mm. The specimens had been pre-sintered to remove the binder and to provide enough mechanical strength to handle them. The pre-sintering temperature was 1050 °C with one hour holding time in vacuum.

3.6 Mechanical testing

3.6.1 Hardness

Hardness measurements were conducted on polished or ground specimens (grit 2000) using a load of 5 kg applied during 30 seconds and, in some cases, 2 kg and 30 seconds. All the results presented correspond to the average of at least 6 points. None of the hardness measurements were conducted close to the surface of the specimens, thus the values displayed correspond to an average of the bulk material. The measurements were carried out using an Emcotest model M1C010 equipped with a Vickers type indenter.

3.6.2 Tensile

The tensile tests were conducted using specimens with 30 mm of strain gauge in air at room temperature. A servohydraulic test machine model MTS 810 from Materials Testing Systems with a load cell of 100 kN capacity was used. The strain rate applied was 2.38 x 10^{-5} per second. The elongation was measured by an extensometer attached to the ridges of the specimen. Two to three specimens were normally tensile tested and the results averaged.

3.6.3 Creep

Creep tests were conducted in two different loading modes: compression and tension. For screening of alloying elements (Part I and Part II) compression creep loading was always used, while for the Final Alloy Candidates both tensile and compression creep tests were conducted. Three different creep loading conditions were applied throughout this work, as displayed in Table 9. All measurements were carried out in air.

Table 9 – Creep testing parameters.

Temperature (°C)	Stress (MPa)
800	350
900	100
950	200

Compression creep experiments were carried out using an Instron-Satec SF-16 2230 machine with a lever arm ratio of 1/16. Three thermocouples (type K) were used as input for temperature control. Two of the thermocouples were placed directly above and below the specimen. One of the thermocouples was attached at the centre of the specimen. Temperature variations achieved were within ± 2° C of the desired temperature. The cylindrical specimens had an average length of about 9.5 mm and a diameter of 7.2 mm. They were also ground on both ends to remove the rough sintered surface before creep testing. All specimens were deformed at least until 1% strain.

Tensile creep experiments were conducted using Instron-Satec machines model M3 Mentor with a lever arm ratio of 1/16. Three thermocouples (type K) were used as input for

temperature control, which were attached to the specimen at the top, bottom and middle region. Temperature variations were within ± 1° C of the desired temperature. The specimens were machined from MIM pre-forms and tested with as-machined surfaces, Figure 10. All specimens were tested until creep rupture.

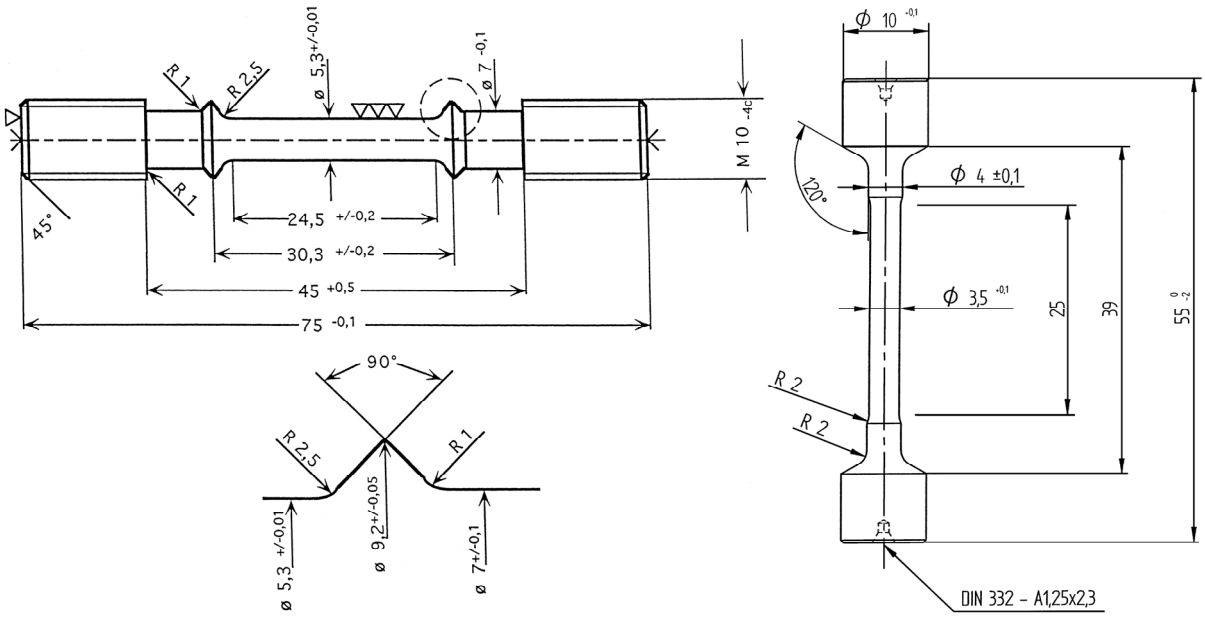

Figure 10 – Final geometry of machined specimens. (a) Tensile creep specimen. (b) Tensile specimen. Dimensions are in millimetres.

4. Feasibility study of alloy variations in pre-alloyed TNB-V5 by using elemental powders

The use of pre-alloyed powders usually yields the best results in powder processing of titanium aluminides because the chemical homogeneity is improved in comparison to using elemental powders. Ideally in the context of alloy development for MIM, the use of gas atomised spherical pre-alloyed powders for each and every composition to be tested would be highly desirable. However this implies excessive costs since each composition would require a separate atomisation run and thus melting of ingots, which is impracticable in reality for small screening batches. Consequently, a combination of using pre-alloyed powder of a master alloy, in this case TNB-V5, and elemental powders was investigated in order to obtain different titanium aluminide alloys. For convenience and to reduce the waste of material, sample preparation was also simplified by uniaxially pressing the feedstock instead of MIM. According to previous investigations [178], in the case of the small specimens studied both preparation methods lead to similar microstructures. The objective of this feasibility study was the characterisation of the sintering behaviour of chemical variations of the base material obtained by adding elemental powders. An understanding of the processes occurring during sintering of powder blends is necessary to develop alloys optimised for MIM processing.

4.1 Experimental procedure

Two groups of specimens were prepared. One series of alloys exhibited varying aluminium contents, Ti-(43-47)Al-5Nb-0.2B-0.2C. The specimens will be named after their aluminium content hereafter, e.g. 43Al, 44Al, etc. The aluminium variations were achieved by adding elemental Ti and Al for the cases of less and more aluminium respectively. Secondly, the feasibility of introducing an additional heavy element to the reference material forming a quaternary alloy was tested. For that purpose the alloy Ti-45Al-5Nb-1.5Mn-0.2B-0.2C was selected. The desired composition was prepared by adding elemental Mn and also small amounts of Al, Nb and B so their relative concentrations remained equal to those of the base alloy. Specimen preparation was conducted by uniaxially pressing of a feedstock as describe in the Materials and Experimental Procedure section. Sintering experiments were conducted at temperatures ranging from 1450 to 1510 °C in vacuum for 2 hours.

4.2 Results and discussion

4.2.1 Variations of aluminium content in TNB-V5

Aluminium variations in TNB-V5 were chosen as starting point for the feasibility study because using TNB-V5 as master alloy to prepare different compositions would inevitably require addition of pure elemental aluminium. Besides, the microstructure and properties of titanium aluminides are highly sensitive to the aluminium content. Since difficulties regarding reactive sintering of mixtures of elemental titanium and aluminium, which could lead to higher porosities, have been previously reported [21,22], it was important to confirm if such effects would also have an influence in mixtures of pre-alloyed and elemental powders. Therefore assessing the feasibility of using elemental powders for the tuning of the compositions based on a master alloy was an important milestone for the entire study.

The sintering behaviour was investigated through various sintering experiments at different temperatures. The porosities as a function of sintering temperatures are shown in Figure 11. There was a significant drop in porosity at 1470 °C for the reference material TNB-V5, which reached less than 1% porosity between 1490 and 1510 °C. In comparison to TNB-V5, additions of aluminium led to less densification at the same sintering temperature. As clearly visible when comparing 46Al and 47Al, the temperature at which the porosity was considerably reduced shifted to higher temperatures by the addition of elemental Al.

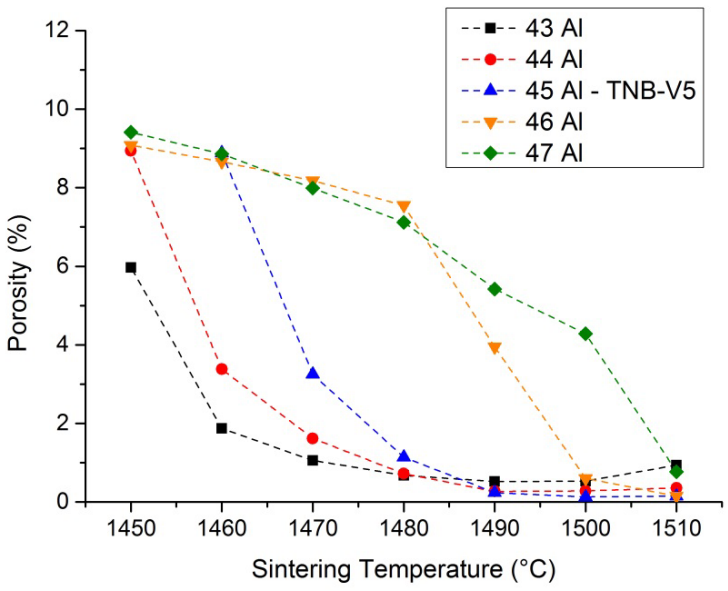

Figure 11 – Porosity as a function of sintering temperature for aluminium variations.

Figure 12 shows the variations of Vickers hardness as a function of aluminium content for different sintering temperatures. There was a trend of increasing hardness with sintering temperature reflecting the corresponding decrease of porosity. It is clearly visible that the hardness decreased as the aluminium content increased, a noticeable trend regardless of the sintering temperature. This fact could be explained by the effect of aluminium on the strength of titanium aluminides. By investigating a series of binary (Ti-Al) and ternary niobium containing alloys, Paul et al. [129] reported that with increasing aluminium content, the number of α_2/γ interfaces in the lamellar colonies was reduced. Since this type of interface is very effective in hindering dislocation motion, it is clear that less aluminium would cause an increase in mechanical strength which is seen in Figure 12 as an increase in hardness. Huang et al. [106] found a very similar result in a study conducted on binary Ti-Al alloys when aluminium was varied in the range between 46-54Al at.%. The authors reported that although the microstructures were either duplex or single-phase (in the case of higher aluminium contents), there was always a decrease of the yield and ultimate tensile stress with increasing aluminium content.

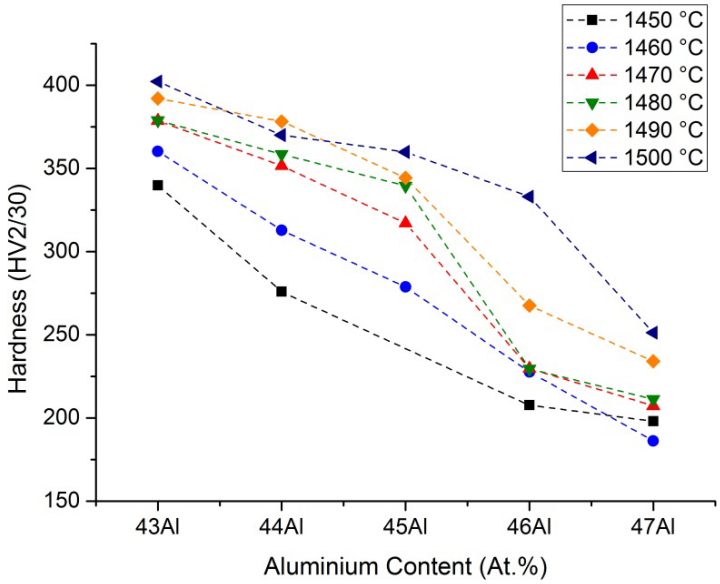

Figure 12 – Hardness as a function of aluminium content for different sintering temperatures.

The microstructures of aluminium variations in TNB-V5 sintered at 1500 °C for 2 hours are shown in Figure 13. In all cases a fully lamellar microstructure could be obtained, however the porosity was severely influenced by the addition of pure aluminium. Besides pores, it was also possible to identify typical microstructural features such as borides and regions of increased niobium content, which originate from segregations arising due to the $\beta \rightarrow \alpha$ phase

transition. The colony sizes and lamellar spacing were larger for specimens with higher aluminium content (46 and 47Al) in comparison to TNB-V5.

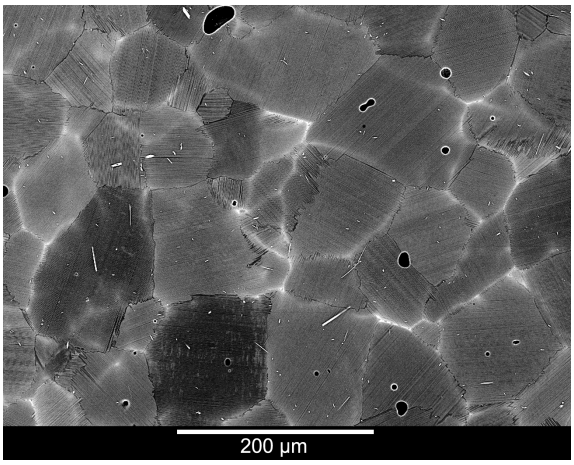

(a) 43Al
Porosity 0.5 ± 0.1% and colony size 73 ± 5 µm

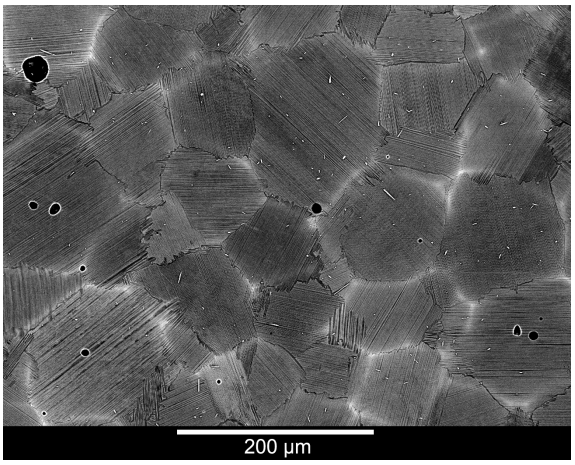

(b) 44Al
Porosity 0.3 ± 0.1% and colony size 74 ± 4 µm

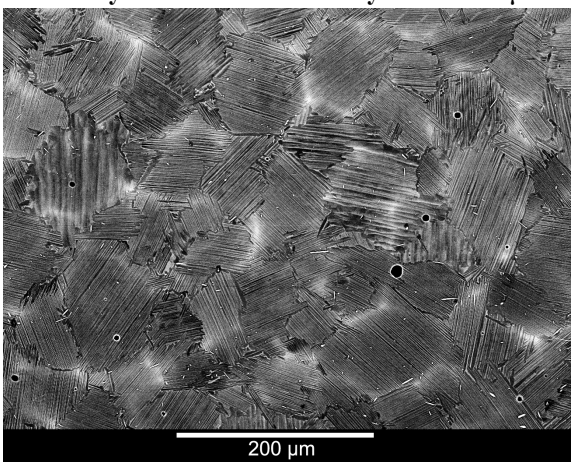

(c) Ti-45Al-5Nb-0.2B-0.2C, TNB-V5
Porosity 0.1 ± 0.1% and colony size 76 ± 7 µm

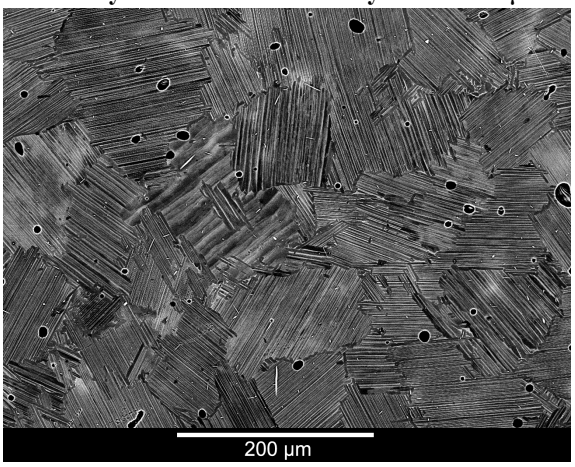

(d) 46Al
0.6 ± 0.3% porosity and colony size 91 ± 8 µm

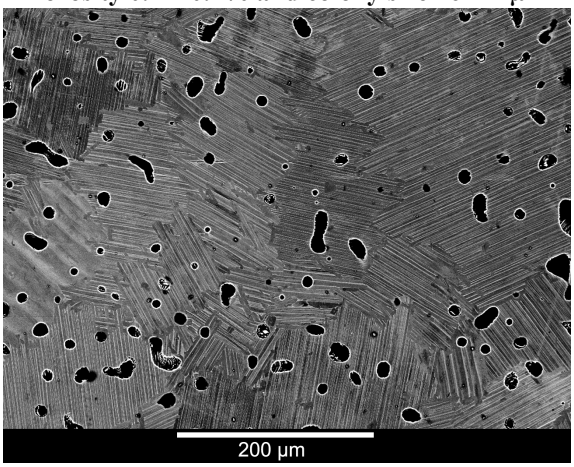

(e) 47Al
Porosity 4.3 ± 0.4% and colony size 101 ± 6 µm

Figure 13 – Microstructures of aluminium variations in alloys sintered at 1500 °C for 2 hours.

The increased colony size with higher aluminium content corresponds to an effect of chemistry rather than heat treatment conditions since all the specimens were cooled down at the same rate after sintering (furnace cooling). The effect of β solidification has already been explained in previous publications [64,66,67,179,180] and although during sintering the specimens are not completely melted, similar transformations take place considering the temperature involved (1500 °C).

The refinement of the colony size for the case of lower aluminium contents takes place because the α phase is directly precipitated from the β phase and therefore follows the Burgers orientation relationship. This leads to 12 possible orientations variants of the α phase and a number of differently oriented α grains can precipitate from one parent β grain, which in turn refines the microstructure. Additionally, with less aluminium the likelihood of coarsening of the α grains during cooling is reduced due to the enlarged α + β phase field.

In contrast, for the case of aluminium rich specimens, the single α phase field is expanded leading to coarsening of the α grains. Furthermore, with more aluminium there is a markedly reduced amount of residual niobium segregations due to the shift of the α phase boundary. As suggested by Imayev et al. [64], these segregations are able to hinder the growth of α grains when passing through the single α phase field. Therefore the α grains in specimens with more aluminium grow unhindered during a larger temperature interval, resulting in a coarser microstructure in comparison to lower aluminium contents.

Figure 14 shows the DSC curves of TNB-V5 and the powder mixtures containing titanium (43Al) and aluminium (47Al) additions. In the case of aluminium addition, there is an endothermic peak around the melting point of aluminium (~660 °C) followed by an exothermic peak, which clearly indicates that a chemical reaction takes place. It is assumed that the molten aluminium reacts with the pre-alloyed powder forming an aluminium rich transient intermetallic phase. In a study conducted by Mirjalili et al. [181] using an aluminium foil and two titanium sheets fixed in a tri-layer sandwich configuration, it was reported that the only observable intermetallic phase that formed during annealing (550-650 °C) of this Ti-Al diffusion couple was $TiAl_3$. The observation agrees with earlier work in which it has been shown by TEM that $TiAl_3$ is the first phase to be formed between pure Ti and Al [182]. Furthermore, a second study [183] revealed that even in sputtered trilayers in which the α_2 or γ phase was sandwiched by pure Ti and Al these phases completely dissolved in favour of $TiAl_3$ during annealing. The authors could explain this result by a quantitative

kinetic model based on the different growth velocities of the involved phases resulting from different diffusion fluxes. Thus, it is concluded that $TiAl_3$ is unambiguously the only phase which is initially formed during the reaction of Al with the pre-alloyed powder.

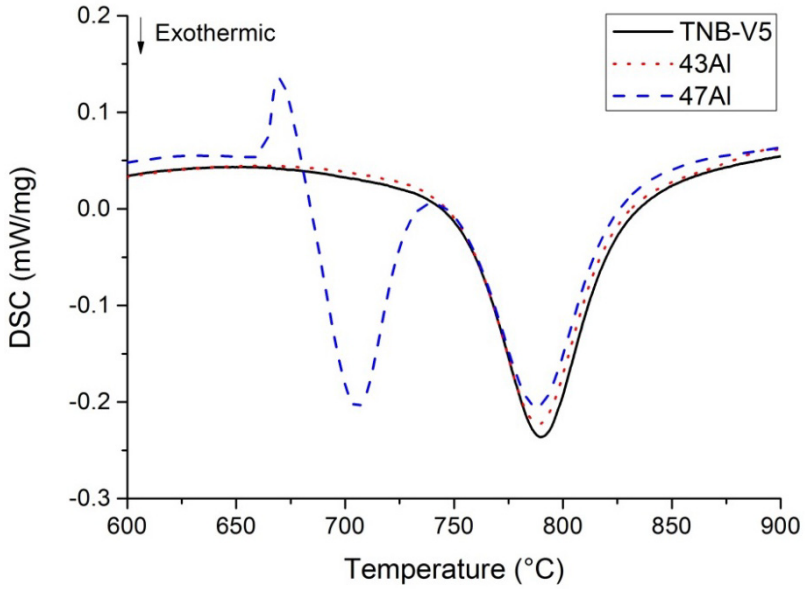

Figure 14 – DSC curves of powder mixtures recorded at a heating rate of 20 °C/min.

The second peak displayed in Figure 14 slightly below 800 °C is assumed to be due to gamma phase precipitation. Considering the fast cooling of the gas atomised powders, the powder particles are composed mostly of metastable phases, which then transform into $\alpha_2 + \gamma$ upon heating. Additionally these peaks occur in a very similar manner for all the alloy variations, confirming that it is an effect originated from the pre-alloyed powder.

At temperatures around 1500 °C the different alloys start to melt, as displayed in Figure 15. The melting peaks are shifted in relation to each other. As it would be expected, there is a decrease in the melting temperature with increasing aluminium content, indicating that significant alloying of the TNB-V5 powder particles with aluminium has already occurred before the melting point is reached. The onsets of the melting peaks were found to be 1512, 1497 and 1477 °C for 43Al, 45Al and 47Al, respectively.

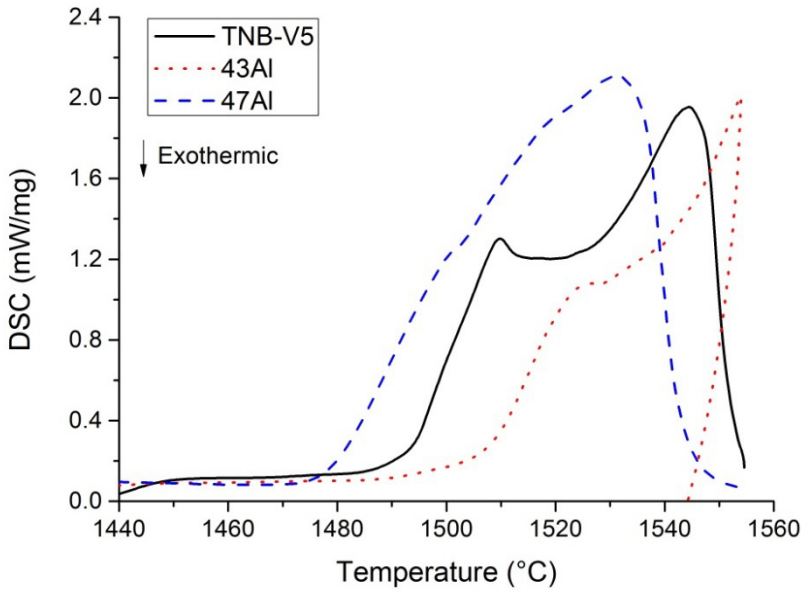

Figure 15 – DSC curves of powder mixtures recorded at a heating rate of 20 °C/min showing the melting peaks.

Simple powder metallurgical processing of mixtures of Ti and Al powders followed by pressureless reaction sintering inevitably leads to porosity due to the fast diffusion of aluminium in titanium (Kirkendall porosity) and the exothermic chemical reaction between the powders [21]**.** As a direct consequence, intermetallic compounds are formed as well as pores. In order to counteract the residual porosity, several possibilities have been used such as hot pressing [19], cold extrusion of powders [20], hot extrusion and hot forging [25,184], etc. Irrespective of the techniques to consolidate elemental powders, a step involving a chemical reaction to obtain the desired intermetallics is always necessary. Different intermediate compounds might form, which in general contribute to an increased final porosity of the sintered part and influence phase homogeneity. In a study of reaction sintering of cold extruded mixtures of titanium and aluminium, Wang et al. [185] showed that the pores formed after the aluminium melting point and the final porosity was proportional to the size of the original aluminium fibres in the as-extruded condition. Since the aluminium powder used in this work was very fine, it is not likely that it would lead to pores as large as shown in Figure 13 (e). Besides, considering the volumetric amounts of aluminium powder used to prepare the feedstock, it would be unlikely that agglomerates would cause such a high amount of porosity. Therefore the pores contained in both specimens with higher aluminium content must have been originated from some reaction between pre-alloyed powder and elemental aluminium, which influenced the densification negatively.

The first reaction when elemental powder mixtures of titanium and aluminium are used in order to obtain titanium aluminides is the formation of an aluminium rich intermetallic phase, as supported by many experimental findings. Therefore in the case of a pre-alloyed powder, such as TNB-V5, it is also possible that through additions of elemental aluminium a chemical reaction would occur, as confirmed by the DSC measurement in Figure 14. Thus, in addition to Kirkendall porosity caused by fast diffusion of aluminium in titanium, another source for pores could be due to the formation of an aluminium rich intermediate phase ($TiAl_3$). Dahms et. al. [21] have shown that in a mixture of extruded elemental powders of the overall composition Ti-49Al (in at.%) two effects happen during the first phase of the sintering heat treatment. Below 660 °C aluminium diffuses into titanium creating Kirkendall porosity. Above 660 °C the remaining aluminium melts and penetrates into the open spaces between the particles, leaving macro-pores behind after sintering. As the aluminium becomes liquid, it could partly or totally cover the pre-alloyed powder particles due to capillary forces, thus forming a layer of $TiAl_3$, as schematically illustrated in Figure 16.

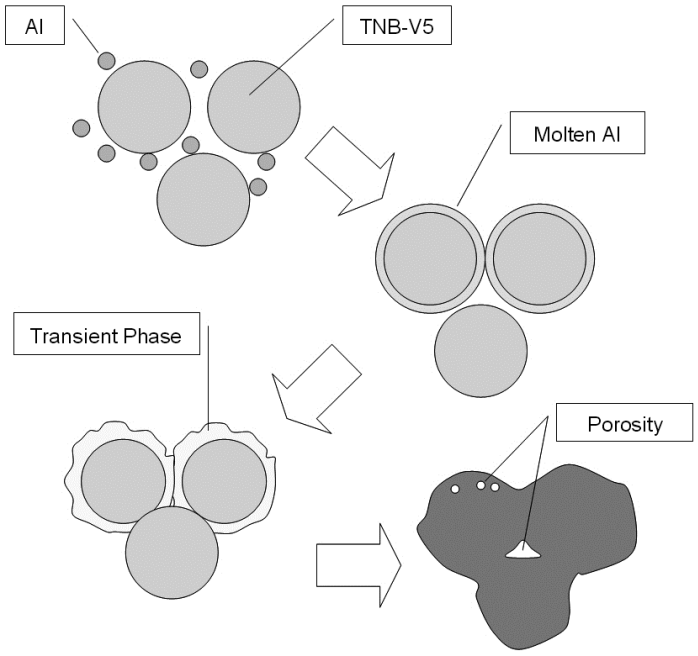

Figure 16 – Formation of pores through addition of elemental aluminium. Adapted from [25].

Assuming that the $TiAl_3$ coating on the pre-alloyed particles remains stable up to high temperatures, necking formation could be slowed down due to the different sinteractivity of

$TiAl_3$. This would therefore hinder the densification in comparison to TNB-V5 without elemental powder additions at the same sintering temperature.

In order to further investigate the formation of an aluminium rich intermetallic phase during sintering, the sintering process was interrupted before final densification in one experiment. Since $TiAl_3$ forms after the aluminium melting point and is consumed during sintering, the process needs to be stopped at a temperature above 660 °C but not so high that the $TiAl_3$ layer was already consumed by subsequent reactions. Unfortunately it is not possible to reliably handle specimens sintered at too low temperatures due to their insufficient mechanical integrity. Therefore 1300 °C with 1 hour of holding time was chosen for this purpose. The same debinding and sintering atmosphere as for the previous specimens were used. The micrographs are shown in Figure 17.

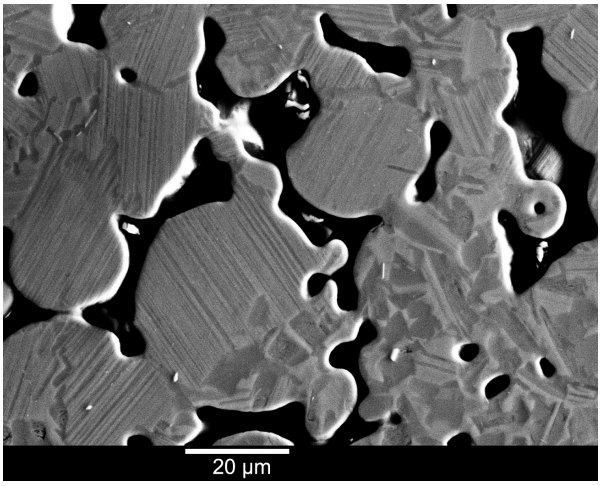

(a) Ti-43Al-5Nb-0.2B-0.2C

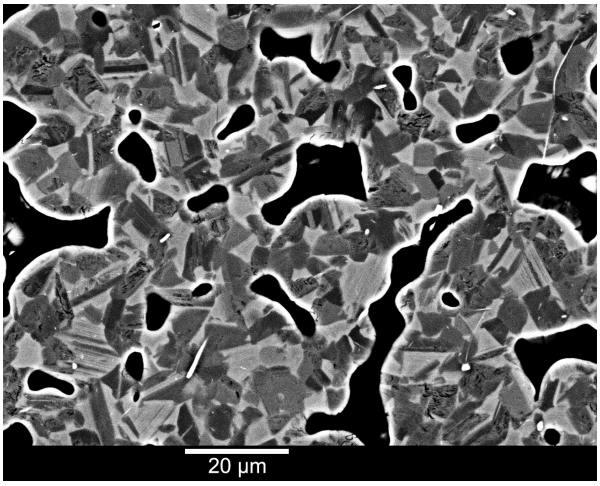

(b) Ti-45Al-5Nb-0.2B-0.2C (TNB-V5)

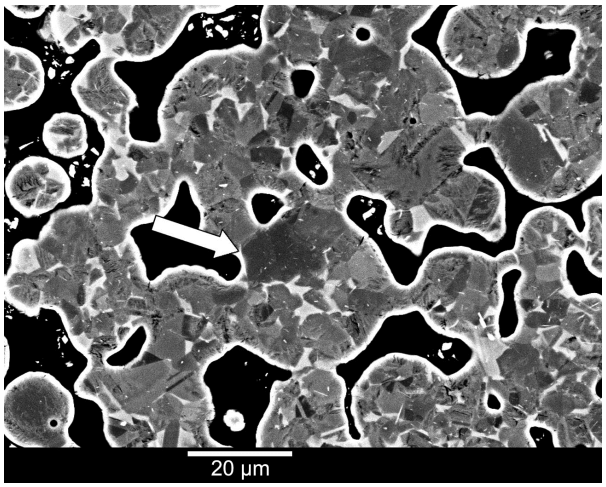

(c) Ti-47Al-5Nb-0.2B-0.2C

Figure 17 – Low temperature sintered powders (1300 °C – 1h) showing neck formation.

The specimen with titanium addition (43Al) showed mostly a lamellar microstructure mixed with a duplex fraction in some regions, Figure 17 (a). At 1300 °C it is likely to be in the α single phase field and the duplex areas were probably developed during cooling. On the other hand, the reference material (TNB-V5) with 45Al seemed to have been completely in the α + γ two phase field, which resulted in a duplex microstructure, Figure 17 (b). The specimen with increased aluminium content (47Al) showed a duplex microstructure as well, however the presence of a smeared darker area of approximately 10 μm (and smaller) in size was identified at the surface of particles and at the sintering necks, Figure 17 (c). This new microstructural feature could not be found in any of the previous specimens. The particular areas of chemistry variation may be regarded as a good indication of a previous aluminium rich intermediate phase. This type of necks occurred obviously not everywhere in the sintered specimen of 47Al, because they were the result of reactions with the largest aluminium particles (~15 μm), considering that the smaller ones would have already been homogenised. Thus, this finding supports that the presence of elemental aluminium creates an intermediate aluminium rich intermetallic phase, which hinders densification.

In order to measure the amount of aluminium variations in the vestigial $TiAl_3$ zone, EDX measurements were carried out in the specimen with aluminium addition. The chemical composition profile is displayed in Figure 18. Dark areas are noticeable in the sintering neck and surface of the particles located at the upper left corner. The compositional line profiles measured showed that the aluminium content in the sintering neck is higher than in the centre of the particles. This difference, however, is not so pronounced due to the sintering parameters used, which allowed to some extent homogenisation to take place. This result supports the idea that an aluminium rich zone was previously present at the interface between the particles and that it dissolved as the sinter process continued. Nonetheless its effect is clearly noticed based in the porosity levels of specimens with aluminium addition after sintering.

It is also possible to identify dark areas inside the particles (in addition to the ones at the surface), which correspond to γ grains of the duplex microstructure resulting from low temperature (1300 °C) sintering. They were smaller in size and fairly equiaxed in comparison to the dark areas at sintering necks.

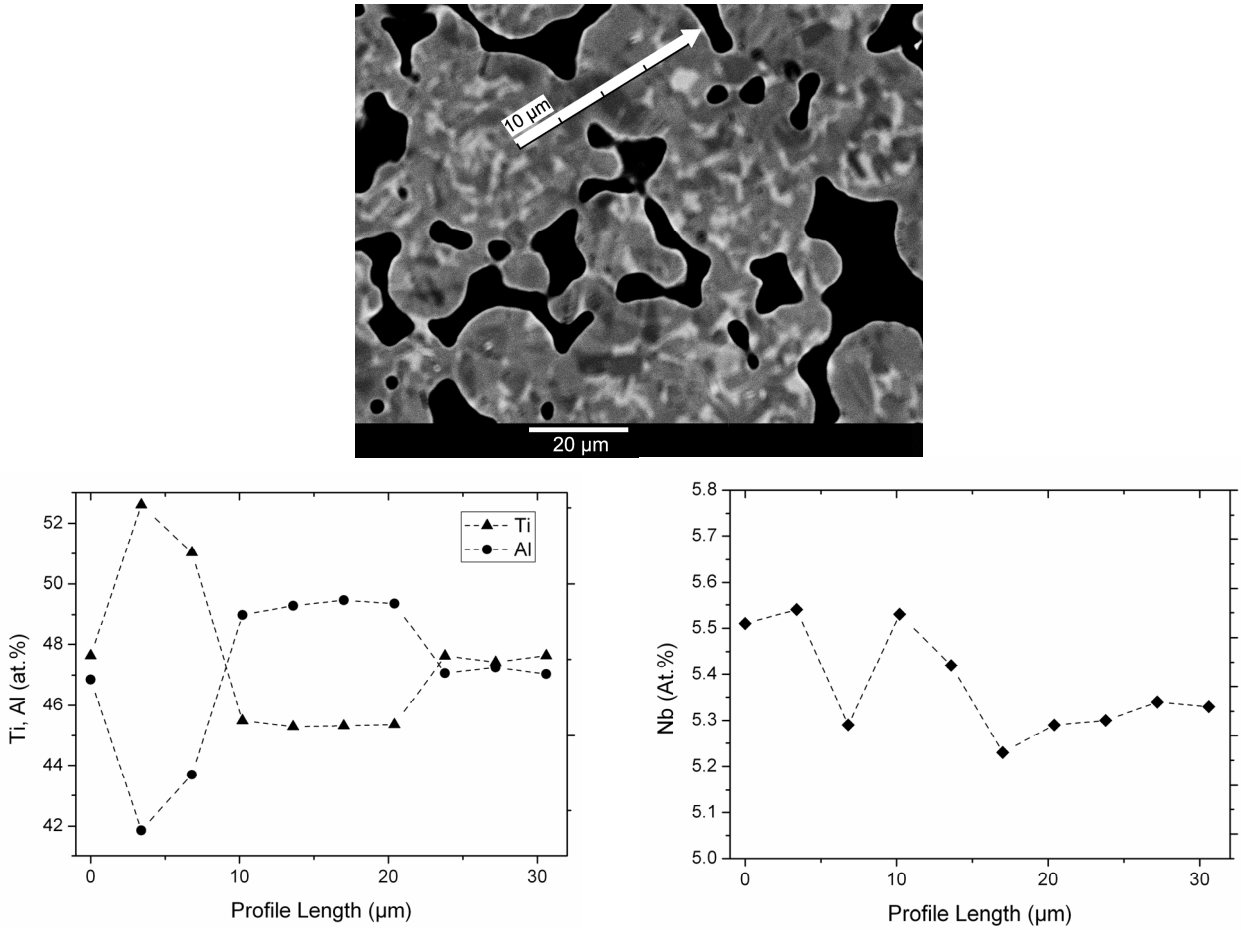

Figure 18 – Variation of chemical composition in a sintering neck of a Ti-47Al-5Nb-0.2B-0.2C specimen.

4.2.2 Introduction of a quaternary heavy element into TNB-V5

A second group of specimens containing a quaternary element was also tested to proof the feasibility of introduction of heavy alloying elements by addition of elemental powder. The alloy Ti-45Al-5Nb-1.5Mn-0.2B-0.2C was prepared by adding elemental Mn, Al, Nb and B and also sintered at different temperatures. The porosity as a function of sintering temperature is shown in Figure 19. As previously seen with the aluminium additions, higher sintering temperatures were necessary in comparison to TNB-V5 due to a shift of the optimum sintering temperature to higher values. Porosities in the order of 1 % could be achieved for temperatures higher than 1490 °C. These porosity values were nonetheless not as low as for pre-alloyed TNB-V5.

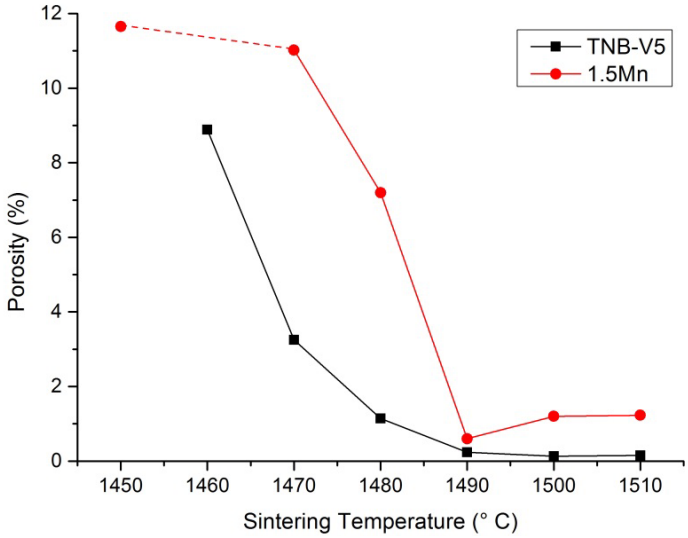

Figure 19 – Porosity as a function of sintering temperature for the Mn-containing alloy.

The microstructures of TNB-V5 and Ti-45Al-5Nb-1.5Mn-0.2B-0.2C are shown in Figure 20. Both specimens were sintered to a fully lamellar microstructure. It is possible to identify pores, boride particles and regions of increased heavy element content. In the case of TNB-V5, these regions were Nb rich, while for the Mn-containing alloy, a combination of Mn and Nb could be found by EDX measurements. Some areas showed the presence of retained β phase, as displayed in Figure 20 (b). This could be expected considering that Mn is a β stabilising element. The addition of Mn also led to a refinement of the colony sizes in comparison to TNB-V5. Even though the microstructure was not completely homogeneous, no regions containing remnants of the Mn powder added could be found.

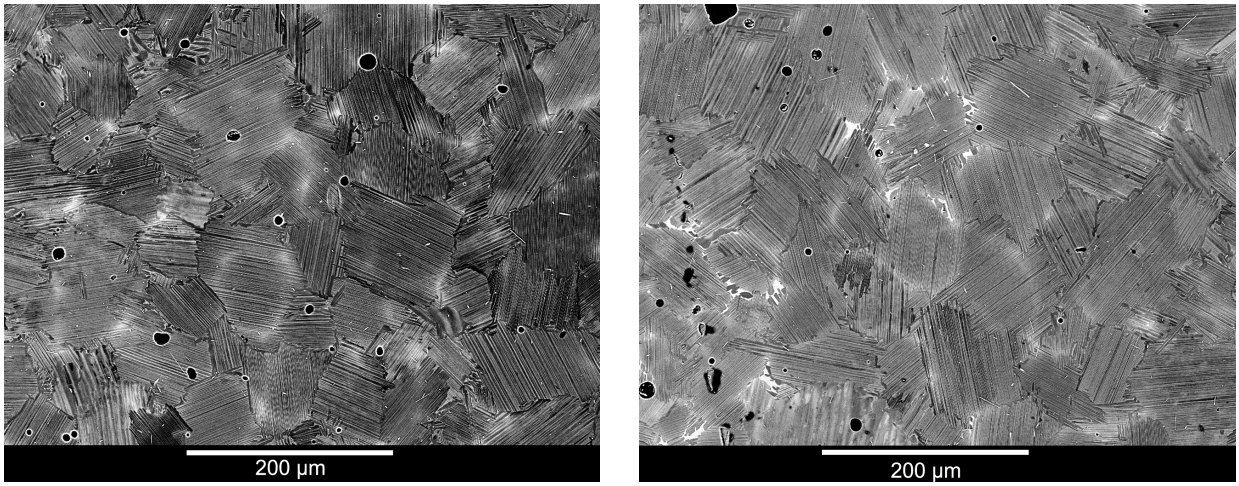

(a) TNB-V5
Porosity 0.3 ± 0.1% and colony size 78 ± 8 µm

(b) Ti-45Al-5Nb-1.5Mn-0.2B-0.2C
Porosity 0.6 ± 0.2% and colony size 65 ± 5 µm

Figure 20 – Microstructures of specimens sintered at 1490 °C for 2 hours.

4.3 Conclusions

In summary, mixing pre-alloyed TNB-V5 and elemental titanium/aluminium in order to prepare different alloys is feasible and porosities lower than 2% can be achieved within the range of aluminium (43-47 at.%) tested. Furthermore, Mn was successfully incorporated into the base alloy via elemental powder addition. However, different sintering temperatures are necessary due to a shift in the optimum sintering temperature. Aluminium additions sharply decreased the sinterability of the base material induced by the formation of an intermetallic layer at the surface of the powder particles during the first stages of sintering.

From this feasibility study it can be concluded that the elemental powder route can be applied for the reliable production of screening specimens in the framework of this thesis. However, small differences to the use of pre-alloyed powders have to be considered for the discussion of the experimental results, especially with respect to porosity and homogeneity of the microstructure.

5. Screening of alloying elements – sintering behaviour and creep resistance

This section contains the results from the initial screening experiments with the arc melting specimens, followed by the powder metallurgy screening of elements (Part I and II). Based on the results of these test series, the most promising candidate compositions for the optimisation of primary creep resistance were selected and further investigated.

The alloys mentioned in the text from now on will be referred based on their main differences to the reference material, TNB-V5 (Ti-45Al-5Nb-0.2B-0.2C). For instance, the composition Ti-45Al-5Nb-**1.5Mo**-0.2B-0.2C will be written as 1.5Mo, as listed in Table 10.

Table 10 – List of compositions and short designations adopted.

	Alloy composition	Short designation
For the arc Melting specimens	Ti-45Al-3Nb-**1.5Mo**-0.2B-0.2C	1.5Mo
	Ti-45Al-5Nb-**1.5Mn**-0.2B-0.2C	1.5Mn
	Ti-45Al-**8Nb**-0.2B-0.2C	8Nb
	Ti-**44Al**-5Nb-0.2B-0.2C	44Al
	Ti-**47Al**-5Nb-0.2B-0.2C	47Al
For specimens from Screening Part I, Screening Part II and Final Alloy Candidates	Ti-44.5Al-**3Nb-0.7W**-0.2B-0.2C	3Nb-0.7W
	Ti-44.5Al-**3Nb-2Ta**-0.2B-0.2C	3Nb-2Ta
	Ti-44.5Al-**3Nb-1Mo**-0.2B-0.2C	3Nb-1Mo
	Ti-44.5Al-5Nb-**1Si**-0.2B-0.2C	1Si
	Ti-44.5-**3Nb-0.2Gd**-0.2B-0.2C	3Nb-0.2Gd
	Ti-44.5-**3Nb-0.5Gd**-0.2B-0.2C	3Nb-0.5Gd
	Ti-44.5Al-5Nb-**1Cr**-0.2B-0.2C	1Cr
	Ti-44.5-**8Nb**-0.2B-0.2C	8Nb
	Ti-44.5Al-5Nb-**1W**-0.2B-0.2C	1W
	Ti-44.5Al-5Nb-**3Ta**-0.2B-0.2C	3Ta
	Ti-44.5Al-5Nb-**1.5Mo**-0.2B-0.2C	1.5Mo
	Ti-44.5Al-**8Nb-1Cr**-0.2B-0.2C	8Nb-1Cr
	Ti-44.5Al-**3Nb-1Mo-1Si**-0.2B-0.2C	3Nb-1Mo-1Si
	Ti-44.5Al-**3Nb-1Mo-0.2Gd**-0.2B-0.2C	3Nb-1Mo-0.2Gd
	Ti-44.5Al-**3Nb-1Mo-1Si-0.2Gd**-0.2B-0.2C	3Nb-1Mo-1Si-0.2Gd

5.1 Arc melting specimens

Specimens prepared by arc melting were used for a preliminary screening of alloying elements and as reference for fast cooled cast microstructures. Modifications of the elements that were already present in the reference material were tested (Nb and Al), as well as the introduction of new elements (Mo and Mn) in order to form quaternary alloys.

The microstructures obtained in the arc melted specimens are shown in Figure 21. In the reference material, TNB-V5, the presence of fully lamellar colonies, boride particles and regions of increased niobium content (Nb microsegregations) can be distinguished. Similar features were observed in all alloy variations, however with some additional characteristics.

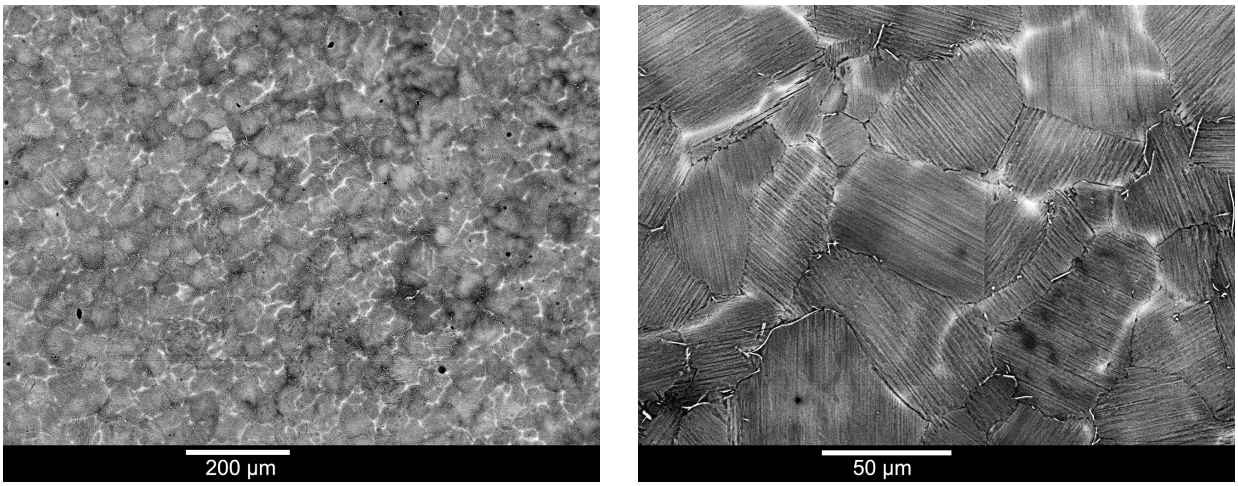

(a) **(b)**

Figure 21 – TNB-V5 prepared by arc melting. (a) Low magnification showing the typical dendritic microstructure. (b) High magnification depicting the fully lamellar colonies.

The quaternary alloys, Figure 22 (a) and (b), showed the presence of retained β phase mainly located at the colony boundaries (brightest phase in BSE pictures). Aluminium variations caused a qualitative change in the Nb microsegregations, which seemed to be less pronounced in the case of 47Al. Although no phase analysis was conducted, it is assumed that the brighter phase in the BSE picture is in fact retained β phase, which is supported by microstructural characterisation of similar alloys [186,187].

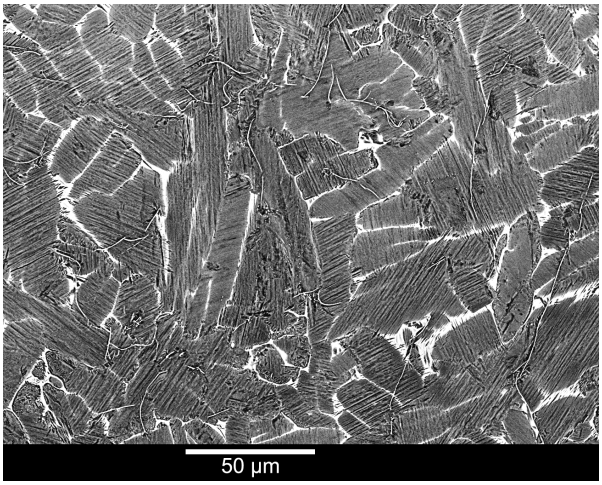

(a) 1.5Mo

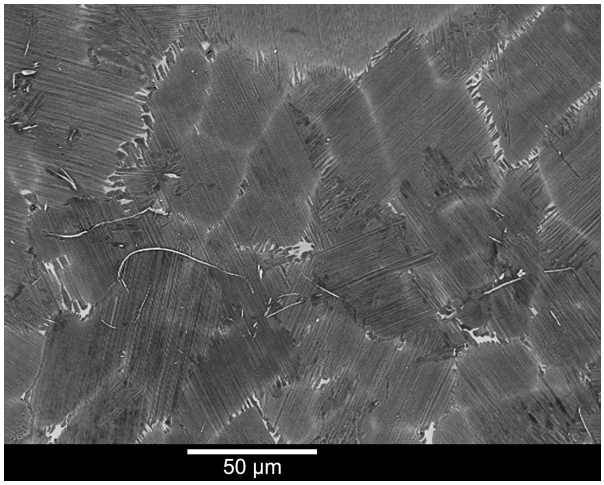

(b) 1.5Mn

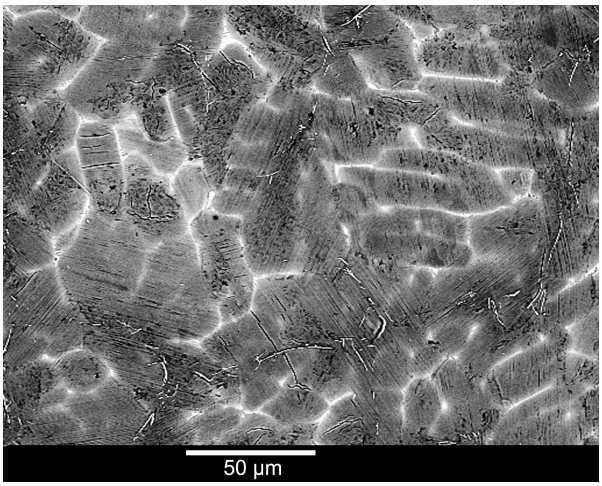

(c) 8Nb

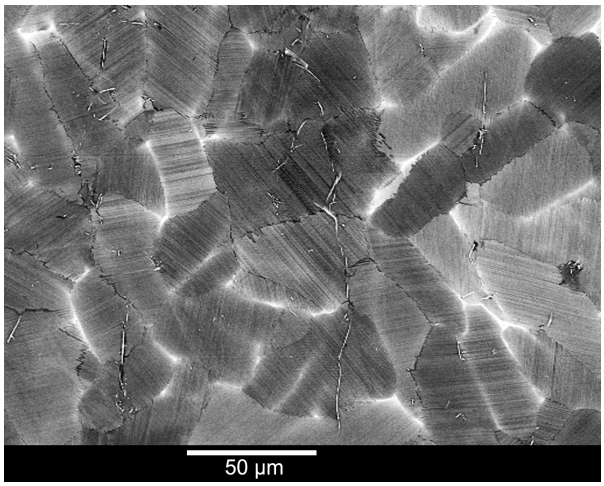

(d) 44Al

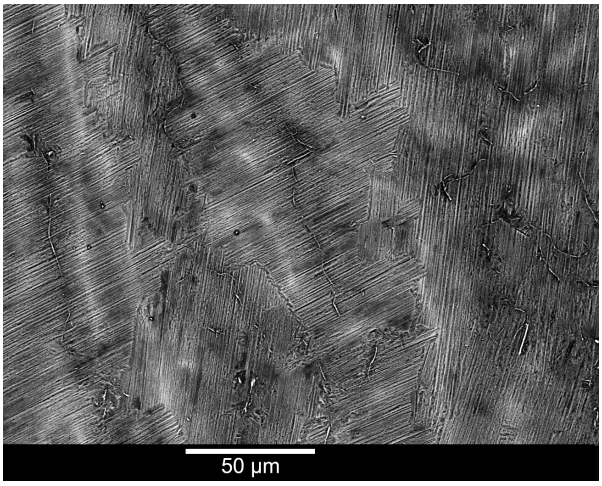

(e) 47Al

Figure 22 – Microstructures of alloy variations prepared by arc melting.

A significant change in colony sizes took place as a function of composition, as displayed in Figure 23. With the exception of 47Al that showed colony sizes in the range of 200 µm, all alloy variations led to colonies smaller than 50 µm in average. The strongest effect in colony size was caused by aluminium variations. In the case of higher aluminium contents, there was an increase from 35 µm (TNB-V5) to 200 µm (47Al).

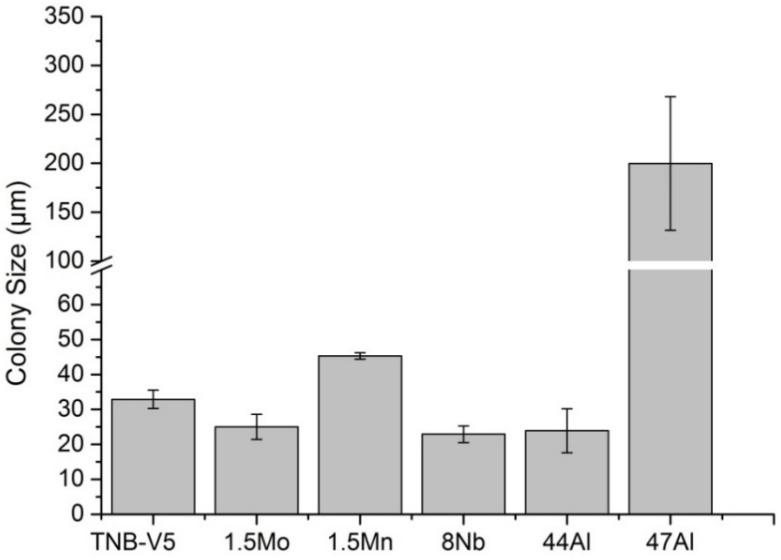

Figure 23 – Colony sizes of the arc melted specimens.

The oxygen and nitrogen contents measured in the specimens prepared by arc melting are shown in Table 11. The high purity of these alloys can be clearly noticed. The oxygen levels achieved were 400 µg/g and below, while nitrogen was around 200 µg/g in average.

Table 11 – Oxygen and nitrogen levels of the arc melted specimens.

Alloy	Oxygen (µg/g)	Nitrogen (µg/g)
TNB-V5	369 ± 14	68 ± 19
1.5Mo	212 ± 17	209 ± 15
1.5 Mn	252 ± 7	174 ± 15
8Nb	213 ± 15	202 ± 19
44Al	438 ± 64	340 ± 194
47Al	198 ± 19	100 ± 6

Figure 24 shows the Vickers hardness obtained with the arc melting specimens. The hardness of 8Nb and 44Al was statistically the same as TNB-V5 (around 440 HV), while 1.5Mn and 47Al showed significantly lower values. The only composition that exhibited a higher hardness was 1.5Mo achieving roughly 470 HV.

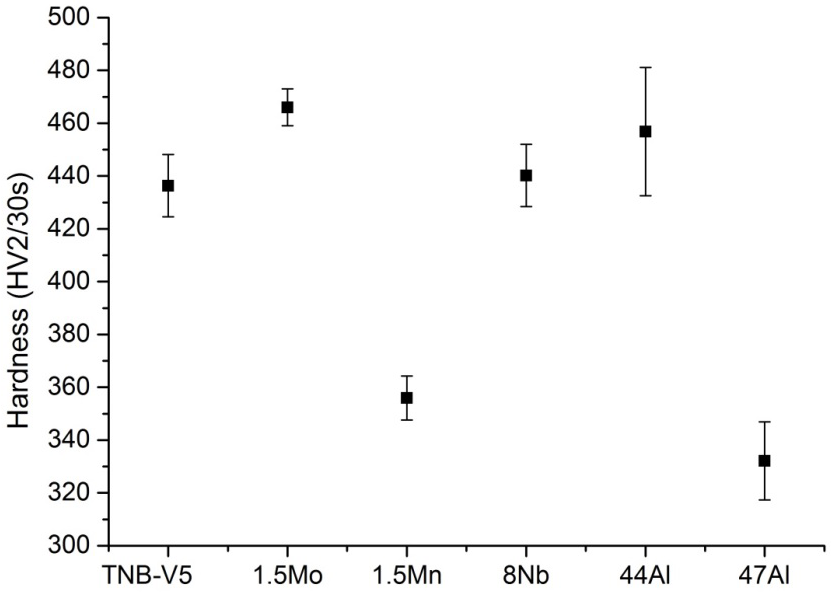

Figure 24 – Vickers hardness of the specimens prepared by arc melting.

The compression creep measurements of the arc melting specimens are displayed in Figure 25. Compression creep at 800 °C and 350 MPa load showed a wide range of primary creep resistance, as displayed in Figure 25 (b). With the exception of 1.5Mn and 44Al, the first percentage of plastic deformation was contained entirely in the primary creep region. TNB-V5 was the third least resistant alloy under the creep conditions applied. The composition 47Al took the longest time to reach 1% plastic deformation (about 23 hours), while the least creep resistant composition was 1.5Mn reaching the same deformation in less than 2 hours.

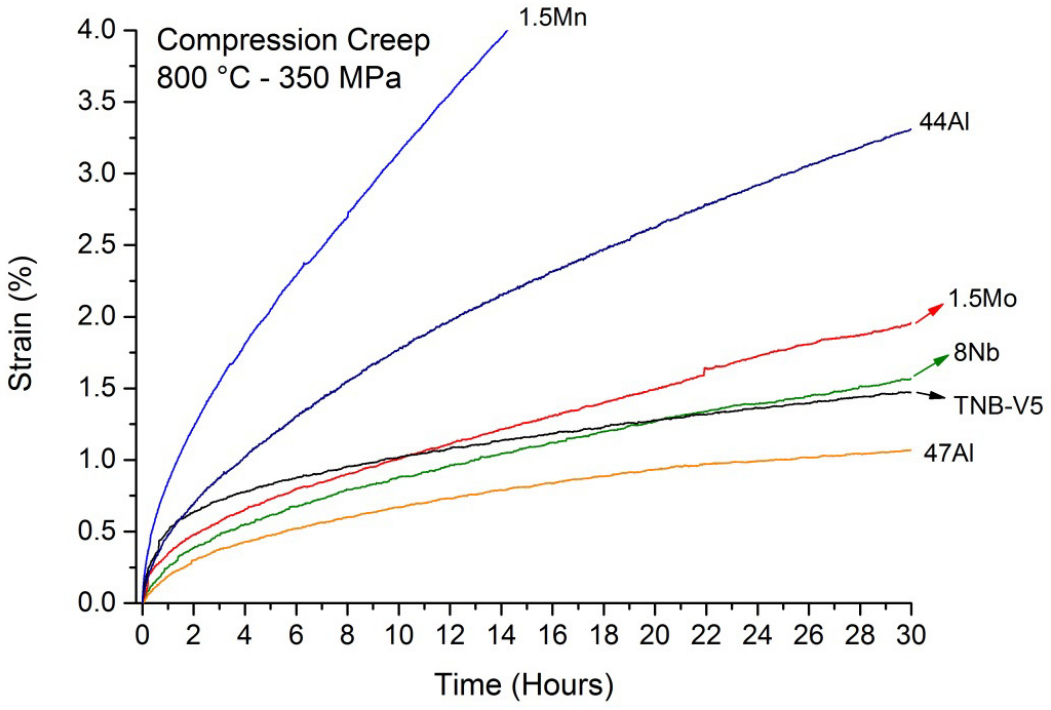

(a)

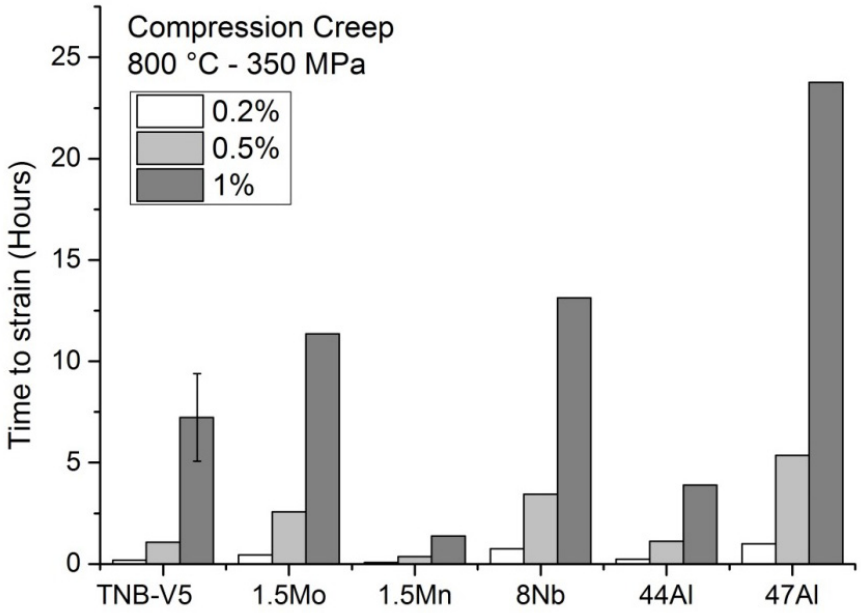

(b)

Figure 25 – Compression creep measurements of arc melted specimens. (a) Creep strain versus time. (b) Time for a specific amount of plastic deformation. Two TNB-V5 specimens were measured and the average of the time to 1% strain is plotted with the error bar representing the time of each individual measurement.

5.2 Sintering behaviour of TNB-V5

The sintering behaviour of TNB-V5 was investigated by dilatometry and DSC using specimens prepared from pre-alloyed powder. The dilatometry specimen was pre-sintered to remove the binder, while DSC was conducted using only the pre-alloyed powder without addition of binder. Typical curves are displayed in Figure 26 and Figure 27.

In Figure 26, from room temperature until 1050 °C (pre-sintering temperature) only dilatation could be noticed, which is characterised by a positive ΔL. After 1050 °C the specimen shrunk almost linearly until the end of the isotherm at 1500 °C. The presence of two inflections that correspond to phase transformations can be noticed. At approximately 255 minutes (1300 °C) the single α phase field was crossed ($\alpha + \gamma \rightarrow \alpha$), while at 390 minutes (1485 °C) the $\alpha \rightarrow \alpha + \beta$ transformation took place. At the isotherm a small fraction of liquid phase was expected to be present considering the onset of the melting peak (1497 °C).

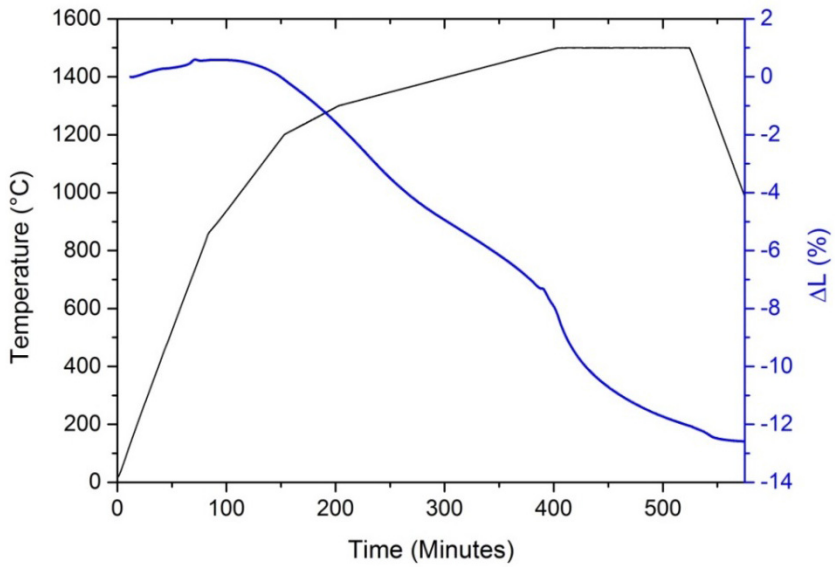

Figure 26 – Dilatometry measurement of TNB-V5 pre-sintered at 1050 °C. The isothermal segment was 1500 °C for 2 hours.

The DSC curve is shown in Figure 27. All the expected phase transformations could be identified. Firstly at about 1230 °C the eutectoid reaction takes place: $\alpha_2 + \gamma \rightarrow \alpha + \gamma$, which is followed by crossing the single α phase field at 1300 °C: $\alpha + \gamma \rightarrow \alpha$. At higher temperatures the phase transformation $\alpha \rightarrow \alpha + \beta$ takes place and lastly the melting peak can

be identified. The isotherm at the sintering temperature (1500 °C) was slightly higher than the onset of the melting peak.

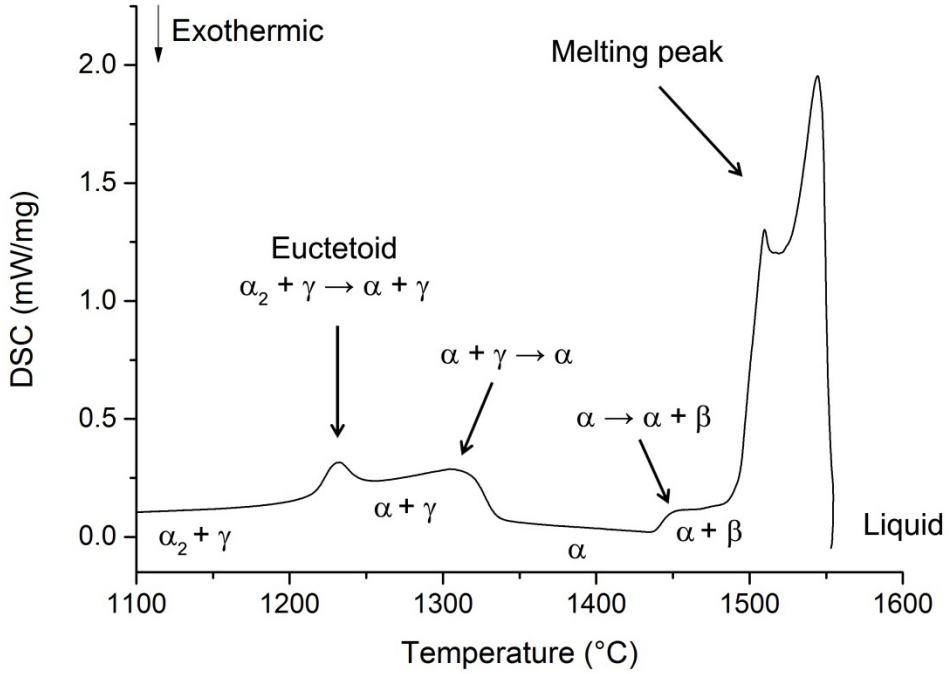

Figure 27 – DSC measurement of TNB-V5 powder conducted with the heating rate of 20 °C/min.

Additionally, in order to have a better overview of the sintering behaviour of TNB-V5 under the actual sinter furnace conditions (atmosphere, temperature gradient, sintering substrate, etc.), a series of sintering experiments with varying temperatures were carried out.

Independent of the final sintering temperature, the heating profile prior to that was the same as the one used for dilatometry. The sintering experiments were conducted with cylinders of approximately 10 mm in length and 8 mm in diameter prepared by Uniaxial Pressing (UP) of feedstock.

The porosity decreased drastically by increasing the sintering temperature from 1460 to 1480 °C, as can be seen in Table 12. A further increase in temperature did not significantly improve the densification and little change could be found between 1500 and 1510 ° C. The colony sizes were approximately the same between 1480 and 1510 ° C in case of 2 hours of sintering time.

Table 12 – Sintering behaviour of TNB-V5. The sintering time was always 2 hours.

Sintering temperature (°C)	Porosity (%)	Sintered density (g/cm^{-3})	Colony size (µm)
1460	8.9 ± 0.6	3.81	41 ± 2
1470	3.3 ± 0.3	3.93	71 ± 6
1480	1.1 ± 0.1	4.06	79 ± 6
1490	0.24 ± 0.04	4.12	79 ± 6
1500	0.13 ± 0.1	4.13	76 ± 7
1510	0.15 ± 0.04	4.12	71 ± 5

5.3 Screening of alloying elements Part I

In this section, results involving specimens prepared with TNB-V5 as master alloy are presented. Following the previous exploratory experiments via arc melting with Mo and Mn as quaternary elements, the effect of W, Ta, Nb, Mo, Si and Gd additions to TNB-V5 were investigated in specimens prepared by powder metallurgy. Two main groups of compositions can be distinguished based on the amounts of β stabilising elements present, the low β and high β series.

5.3.1 Sintering behaviour

The previous experiments from the feasibility study and the investigation of sintering behaviour of TNB-V5 showed that conducting sintering at temperatures between 1500 and 1510 °C for 2 hours was sufficient to achieve porosities in the order of 1% and less. Therefore the specimens for Screening Part I were sintered using the same parameters.

The porosities achieved are displayed in Figure 28 (a). Except for the specimen 3Nb-0.7W, in average all alloys achieved porosities lower or in the order of 5%, which is nonetheless still considerably higher than the values obtained in the feasibility study experiments. Specimens with Gd and Si additions melted slightly at the area in contact with the sintering substrate and consequently showed low porosities due to the presence of higher fractions of liquid phase during sintering. The specimens that required the largest additions of pure aluminium powder in order to reach the desired composition such as 3Nb-0.7W, 3Nb-1Mo and 3Nb-2Ta showed the poorest densifications. This indicates that actually for cases of larger elemental

aluminium additions, the loss in densification was more pronounced than expected from the results from the feasibility studies.

Considering that some specimens with larger amounts of heavy elements showed poor microstructural homogeneity, they were additionally sintered at 1500 °C for 4 hours. The resulting porosities are shown in Figure 28 (b). All specimens achieved lower porosities when sintered for longer times.

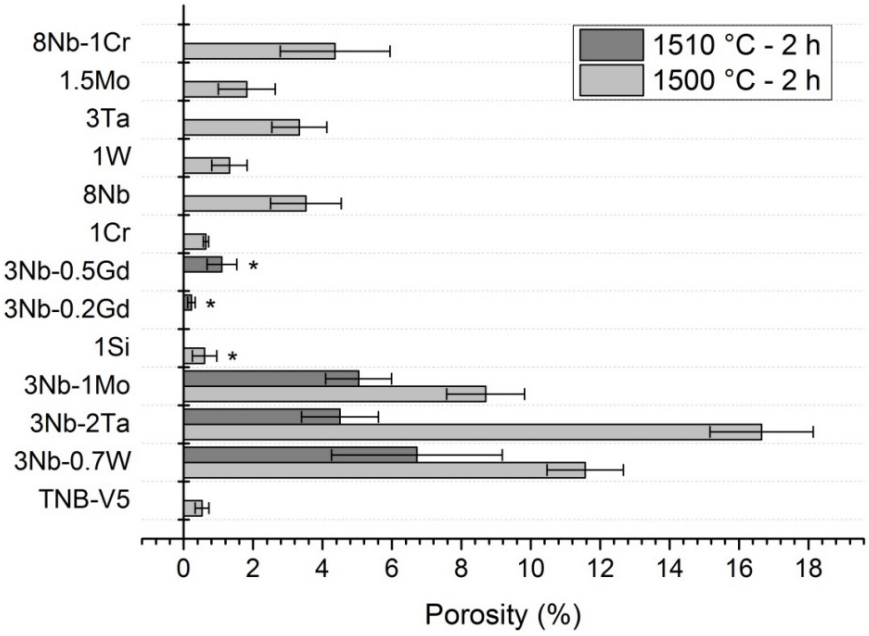

(a)

*** Specimens were lightly melted during sintering**

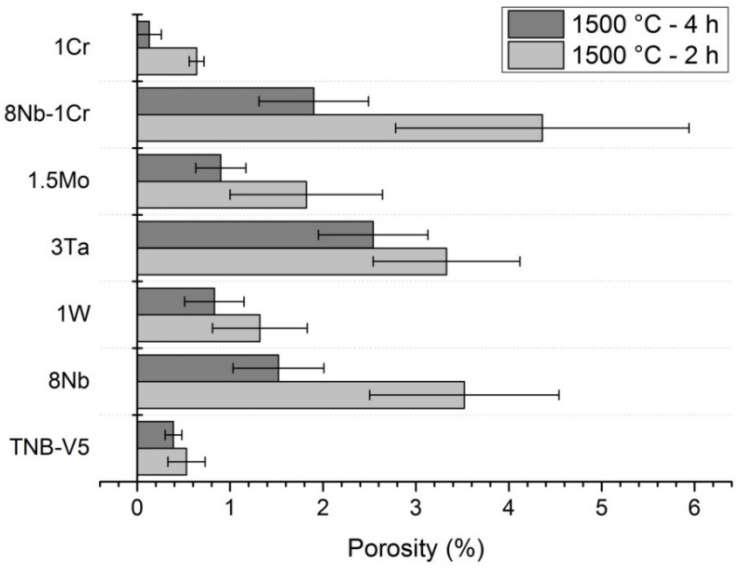

(b)

Figure 28 – Screening Part I, porosities. (a) Porosity of the alloy variations with different sintering temperatures. (b) Porosity of the alloy variations with different sintering time.

The oxygen and nitrogen levels measured in the sintered specimens are displayed in Table 13. It is noticeable that the oxygen content of the low β series was similar to the reference material (around 2000 µg/g). The exceptions were specimens with Gd addition that also showed the largest amounts of oxygen after sintering. The intake of oxygen was proportional to the amount of Gd added indicating that this elemental powder in particular was a strong source of oxygen pick-up. On the other hand, the high β series showed in average lower oxygen levels (below 2000 µg/g) than the reference material and the low β series. The nitrogen levels were seemingly unaffected by the different elemental powder additions and remained around 300 µg/g and below. These values are in the same range as for the arc melted specimens.

Table 13 – Screening Part I, oxygen and nitrogen levels of the specimens that were used for mechanical testing.

	Sintering parameters	**Alloy**	**Oxygen (µg/g)**	**Nitrogen (µg/g)**
Reference	1500 °C – 2h	TNB-V5	2329 ± 67	137 ± 11
Low β	1510 °C – 2h	3Nb-0.7W	2489 ± 259	333 ± 10
	1510 °C – 2h	3Nb-2Ta	2114 ± 50	223 ± 6
	1510 °C – 2h	3Nb-1Mo	2347 ± 197	314 ± 23
	1500 °C – 2h	1Si	1803 ± 2	155 ± 4
	1510 °C – 2h	3Nb-0.2Gd	3504 ± 335	240 ± 24
	1510 °C – 2h	3Nb-0.5Gd	5370 ± 227	261 ± 13
	1500 °C – 2h	1Cr	2320 ± 142	136 ± 37
High β	1500 °C – 2h	8Nb	1876 ± 8	139 ± 22
	1500 °C – 4h	1W	1621 ± 87	219 ± 37
	1500 °C – 4h	3Ta	1400 ± 37	176 ± 13
	1500 °C – 2h	1.5Mo	1876 ± 8	139 ± 22
	1500 °C – 2h	8Nb-1Cr	1569 ± 69	281 ± 31

5.3.2 Microstructures

5.3.2.1 Low β series

Selected microstructures obtained with the reference material and the low β series that achieved the lowest porosities are displayed in Figure 29 and Figure 30. All microstructures were fully lamellar and contained common features such as pores and boride particles. Additionally, TNB-V5 showed the presence of Nb microsegregations, while the alloys with heavy element additions contained retained β phase.

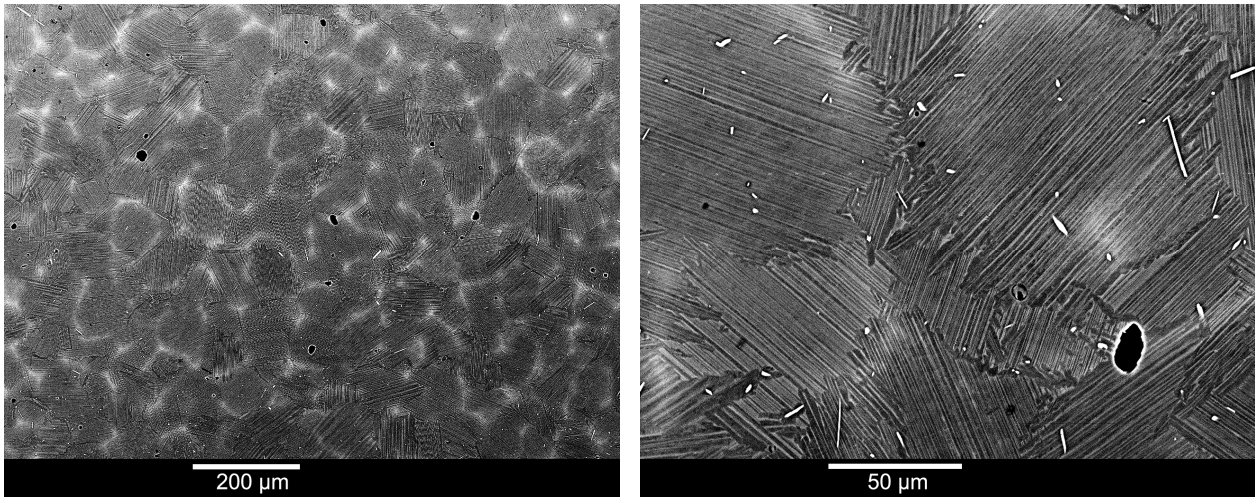

(a) **(b)**

Figure 29 – Microstructures of sintered pre-alloyed TNB-V5 prepared by Uniaxial Pressing (UP). Sintering was conducted at 1500 °C for 2 hours. (a) Low magnification picture displaying the homogeneous powder metallurgy microstructure. (b) High magnification showing the fully lamellar colonies.

Even after sintering at 1510 °C the specimens 3Nb-0.7W, 3Nb-1Mo and 3Nb-2Ta still present fairly inhomogeneous microstructures containing islands of increased porosity and simultaneously depletion of heavy elements, as depicted in Figure 30. On the other hand, specimens containing additions of Cr, Si and Gd achieved reasonably homogeneous microstructures.

The compositions 3Nb-0.7W, 3Nb-1Mo and 1Cr showed the presence of retained β phase present mostly at the colony boundaries. Despite the lack of a detailed microstructural investigation, alloys containing strong β stabilisers are assumed to contain retained β phase. Specimens containing additions of Si, Gd and Ta showed the presence of a network of

segregations, similarly to TNB-V5, instead of retained β phase based on the SEM micrographs.

Si additions led to the formation of precipitates with a wide range of sizes and shapes that were typically located at the colony boundary and its vicinities. Only small colonies were found to contain these particles throughout their whole volume. In contrast, Gd additions formed predominantly elongated particles that were randomly distributed. The addition of 0.5 at.% Gd led to the formation of larger precipitates in comparison to 0.2 at.% Gd.

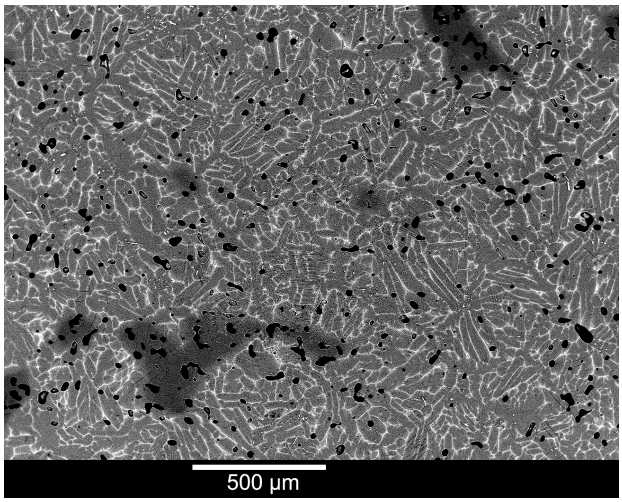

(a) 3Nb-0.7W sintered at 1510 °C for 2 hours.

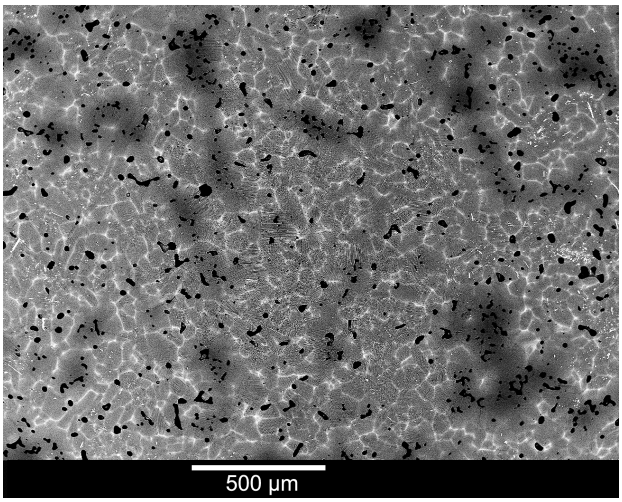

(b) 3Nb-2Ta sintered at 1510 °C for 2 hours.

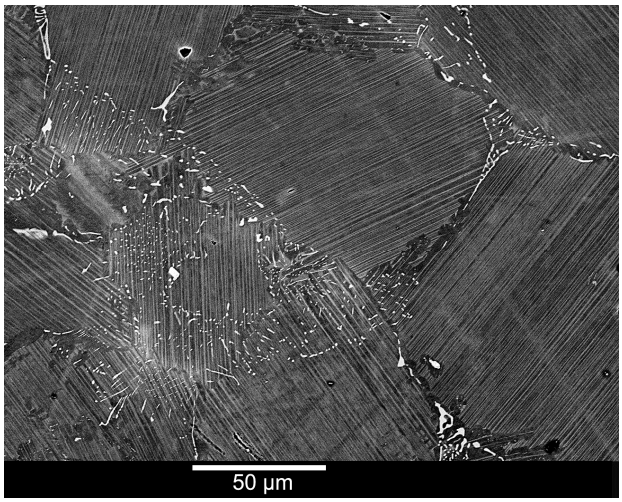

(c) 1Si sintered at 1500 °C for 2 hours.

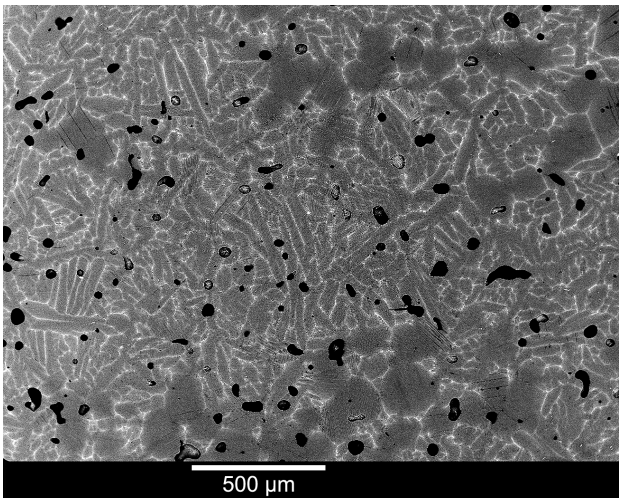

(d) 3Nb-1Mo sintered at 1510 °C for 2 hours.

Figure 30 – Screening Part I, microstructures of the low β series sintered with different parameters.

Independent of the sintering parameters, TNB-V5 showed colony size of 80-90 µm. Except for the alloy 3Nb-0.2Gd, all materials showed a similar or smaller colony size than TNB-V5, as shown in Figure 31.

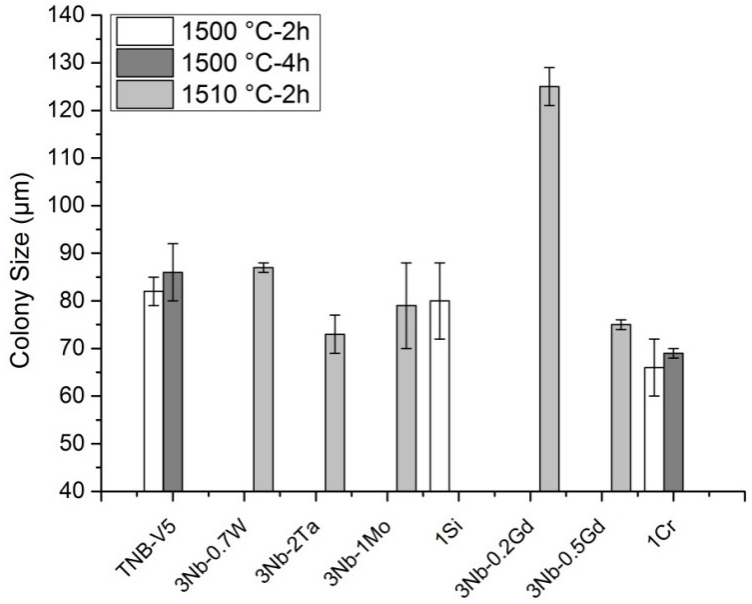

Figure 31 – Screening Part I, colony size of the low β series.

5.3.2.2 High β series

The microstructures obtained with the high β series that achieved the lowest porosities are shown in Figure 32. All microstructures were fully lamellar, independent of the sintering parameters and common features such as pores and borides were found in all alloys. Additionally retained β phase is also present in all specimens mostly at the colony boundaries (bright phase). Qualitatively the amount of β phase appeared to be largest in the case of the W and Mo additions, while it was lower for Ta addition.

Every alloy variation showed to some degree an inhomogeneous microstructure containing islands of increased porosity that were simultaneously depleted in heavy elements. In the cases of 8Nb, 1.5Mo and 8Nb-1Cr, increasing the sintering time led to a significant improvement in the microstructural homogeneity. Nevertheless 1W and 3Ta showed no difference between 2 and 4 hours of sintering.

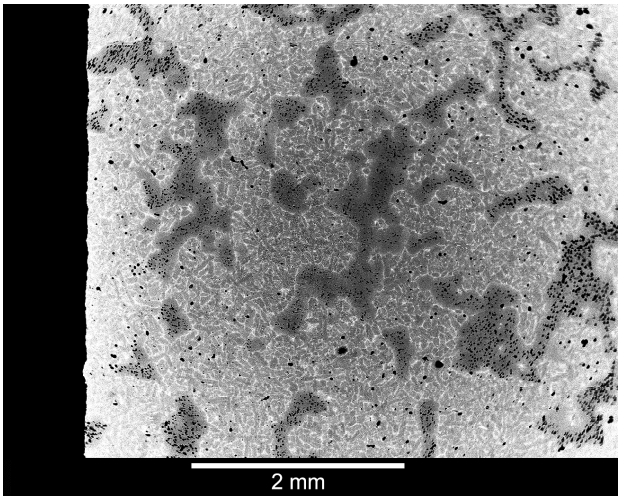

(a) 8Nb sintered at 1500 °C for 4 hours

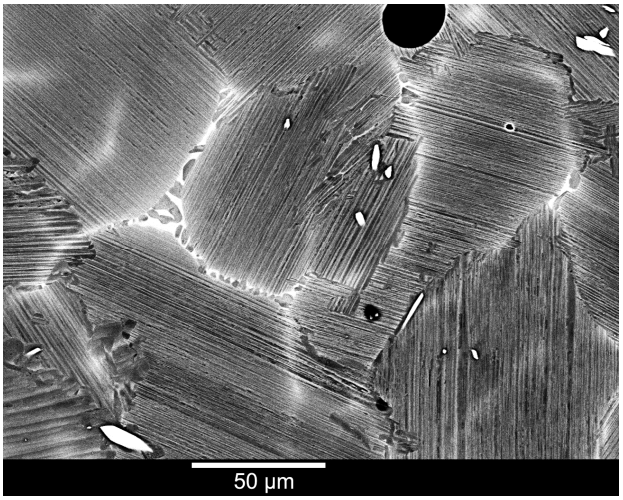

(b) 8Nb sintered at 1500 °C for 4 hours

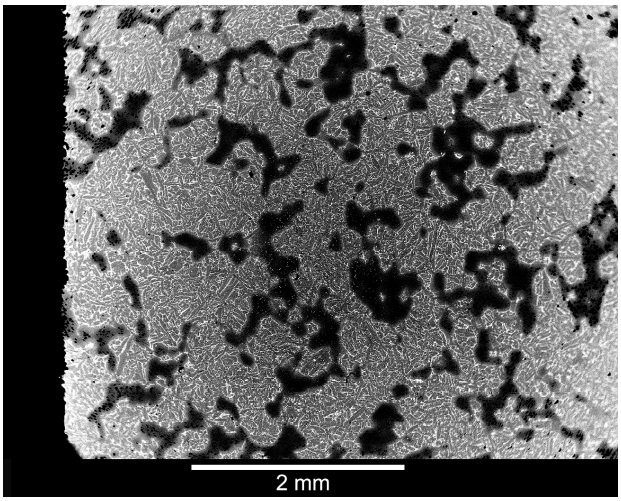

(c) 1W sintered at 1500 °C for 4 hours

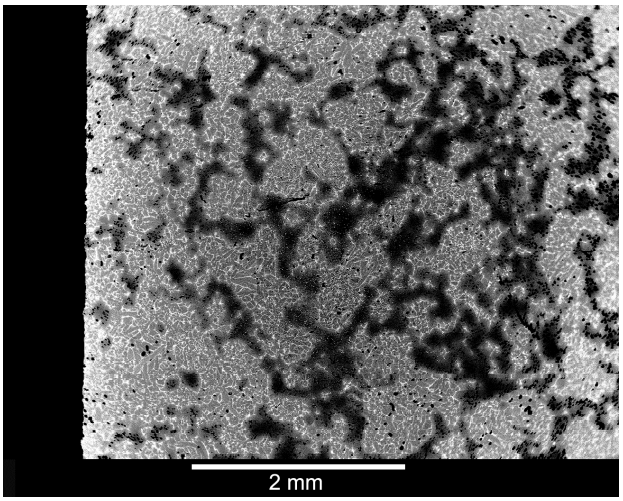

(d) 3Ta sintered at 1500 °C for 4 hours

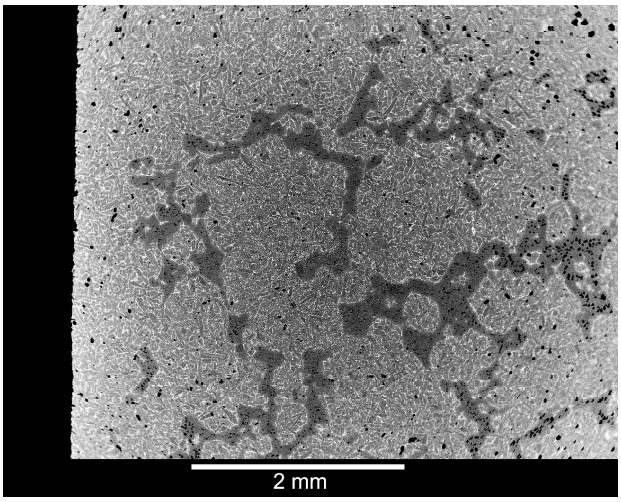

(e) 1.5Mo sintered at 1500 °C for 4 hours

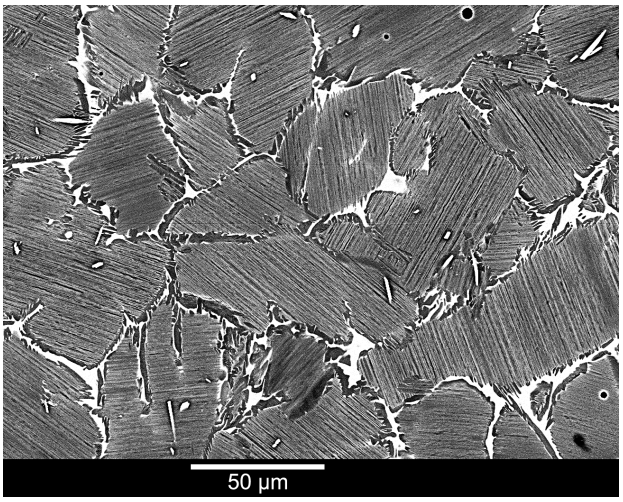

(f) 1.5Mo sintered at 1500 °C for 4 hours

Figure 32 – Screening Part I, selected microstructures of the high β series.

A refinement of the microstructure was found to take place with every element added and/or varied in this series when compared to TNB-V5, as displayed in Figure 33. The finest colony size (approximately 45 μm) was achieved with the 1.5Mo alloy, which was roughly half the size obtained with the reference material.

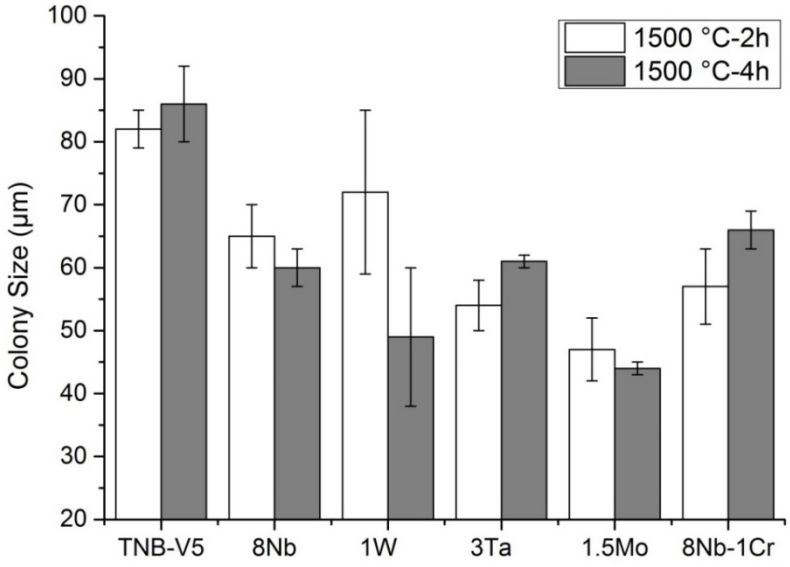

Figure 33 – Screening Part I, colony size of the high β series.

5.3.3 Mechanical properties

5.3.3.1 Low β series

The hardness of the low β series at room temperature is shown in Figure 34. There was a slight change in the hardness as a function of composition. Most of the hardness values were around 340 HV (same as TNB-V5), however even considering the scatter, 1Si (370 HV) and 1Cr (390 HV) showed in fact higher hardness values.

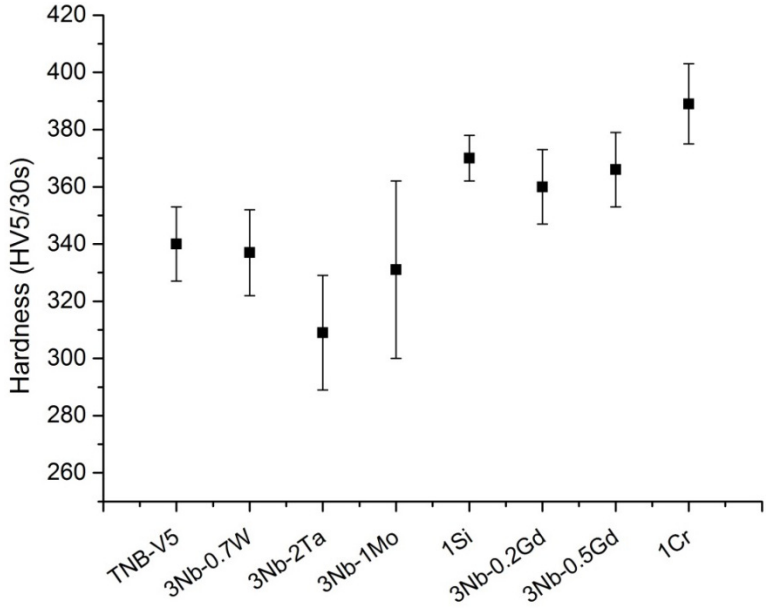

Figure 34 – Screening Part I, hardness of the low β series.

The compression creep tests at 800 °C and 350 MPa loading are depicted in Figure 35 (a) and (b). The creep curves showed a wide range of creep resistance and it is clearly visible that most of the primary creep deformation was comprised within the first percentage of plastic deformation. A significant higher creep resistance than the reference material was achieved by 4 alloy variations: 1Si, 3Nb-0.7W, 3Nb-1Mo and 3Nb-0.2Gd.

The compositions 1Cr and 3Nb-2Ta were the least resistant reaching 1% of plastic deformation in nearly 3 hours, while 3Nb-1Mo and 3Nb-0.2Gd achieved the same deformation in approximately 11 hours. 3Nb-0.7W and 1Si followed as second best candidates. Remarkably there were potential candidate alloys from both concepts, the slow diffusing additions (3Nb-0.7W and 3Nb-1Mo) and the precipitation hardening (1Si and 3Nb-0.2Gd).

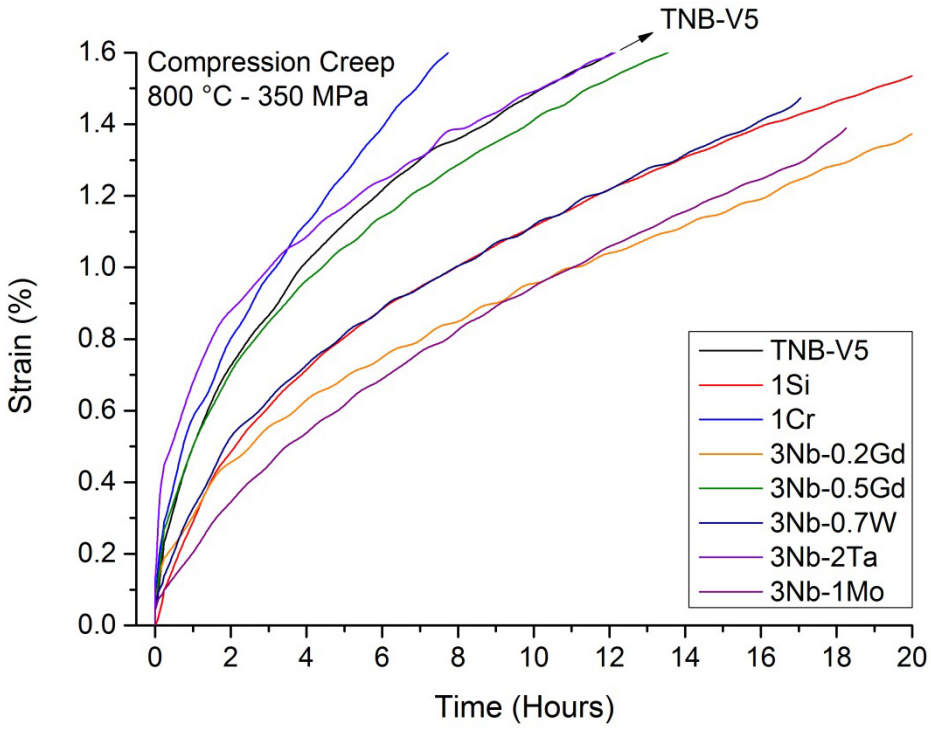

(a)

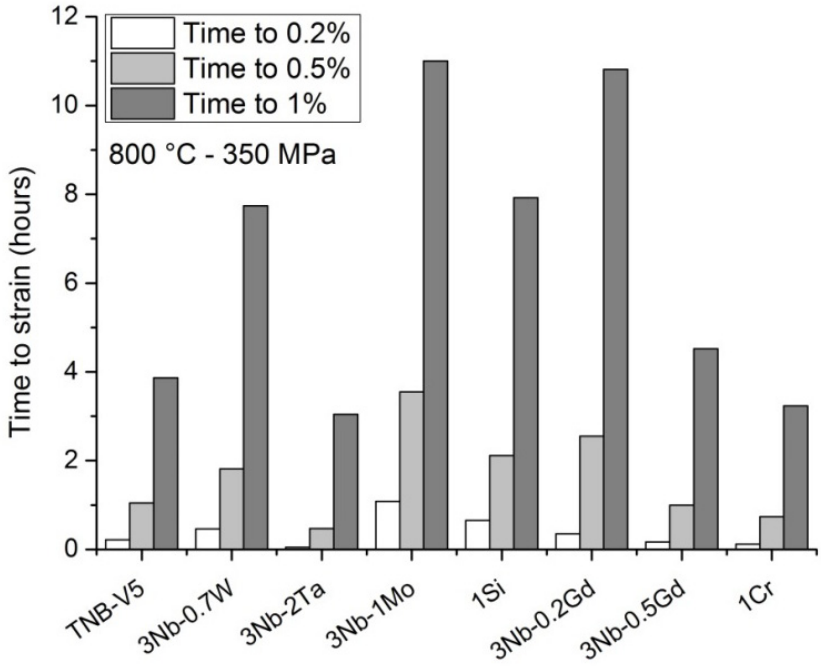

(b)

Figure 35 – Screening Part I, compression creep results of the low β series. (a) Creep strain versus time. (b) Time for a specific amount of plastic deformation.

5.3.3.2 High β series

The hardness of the high β series at room temperature is displayed in Figure 36. There was a trend of increasing hardness for some elements but in general the values were fairly similar. Alloys that statistically showed an improvement in hardness when compared to TNB-V5 (340 HV) were 1W and 1.5Mo (390 HV).

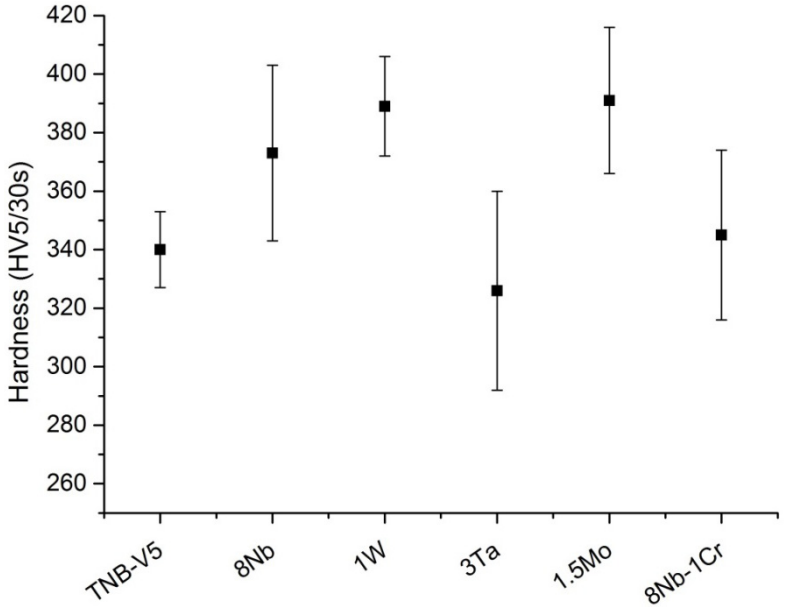

Figure 36 – Screening Part I, hardness of the high β series.

The results of compression creep tests are plotted in Figure 37 (a) and (b). Only 2 alloys showed an improved performance in regard to the time to reach 1% of plastic deformation, 1W and 3Ta. However, only the composition 3Ta showed the same creep resistance level as the best low β alloys (approximately 11 hours). The sinusoidal profile of some of the curves corresponds to the result of small temperature variations caused by the furnace temperature control device. In the case of high β specimens, as previously observed, primary creep deformation was comprised within the first percentage of plastic deformation.

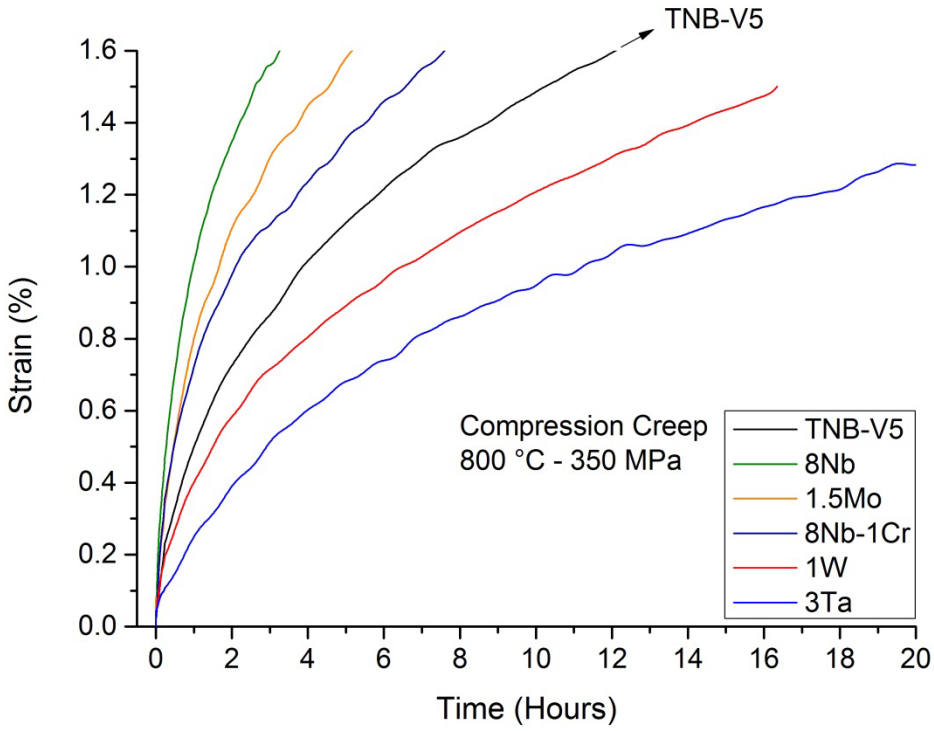

(a)

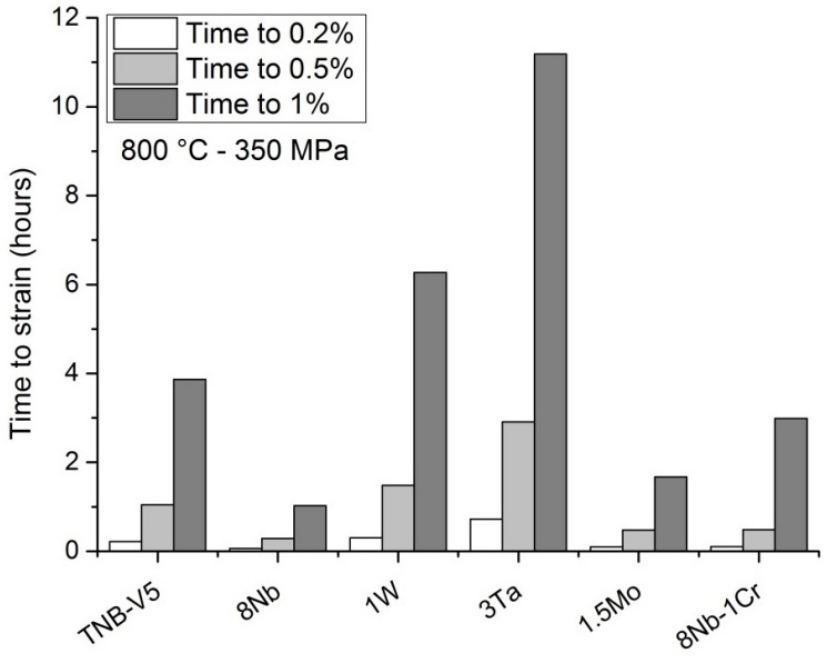

(b)

Figure 37 – Screening Part I, compression creep results of the high β series. (a) Creep strain versus time. (b) Time for a specific amount of plastic deformation.

5.3.4 Summary of Screening Part I

Due to the large variety of properties of this first series of alloy variations, the most important results will be briefly summed up here and compared to the reference material. The time to 1% strain was the main screening parameter but other factors that were taken into account for the selection of the alloy candidates are shown qualitatively. The qualitative variations mean simply if the compared quantity increased or decreased in comparison to TNB-V5. For instance, a "+" sign in regard to porosity means that the porosity was higher than the reference material.

Table 14 – Screening Part I, comparative table for the selection of the alloy candidates.

Alloy	Time to 1% strain (hours)	Microstructural homogeneity	Colony Size	Porosity
TNB-V5	4	Reference	Reference	Reference
3Nb-0.7W	8	-	0	+
3Nb-2Ta	3	-	-	+
3Nb-1Mo	11	-	-	+
1Si	8	0	0	0
3Nb-0.2Gd	11	0	+	0
3Nb-0.5Gd	4	0	-	0
1Cr	3	0	-	0
8Nb	1	-	-	+
1W	6	-	-	+
3Ta	11	-	-	+
1.5Mo	1.5	-	-	+
8Nb-1Cr	3	-	-	+

5.4 Screening of alloying elements Part II

In this section the results of alloys prepared using Ti-48Al-3Nb-0.2B-0.2C and Ti-48Al-5Nb-0.2B-0.2C as master alloys are presented. This change in the base alloy to higher aluminium and different niobium contents was thought as means to decrease the residual porosity by reducing the amounts of elemental powder additions necessary and avoiding the addition of elemental aluminium at all. Based on the previous results of compression creep testing, most alloys were ruled out and were not further investigated, while three new compositions were designed. Their composition is based on the results of the previous screening round combining promising alloying concepts: 3Nb-1Mo-1Si, 3Nb-1Mo-0.2Gd and 3Nb-1Mo-1Si-0.2Gd. Additionally a new way of introducing Gd to the master alloy was evaluated ($GdSi_2$).

5.4.1 Sintering behaviour

Considering that the sintering parameters used in Screening Part I could be improved in case of some of the compositions tested, a more careful estimate of the sintering temperatures was performed based on Differential Scanning Calorimetry (DSC) measurements. The sintering temperatures were chosen as to be higher than the onset of the melting peaks with the intention to aid the sintering process by liquid phase formation, therefore enhancing densification. The difference between onset of melting peak and actual sintering temperature were determined from previous sintering experiments conducted with each alloy. The results are displayed in Table 15. All alloys showed densities similar or slightly lower than TNB-V5, except 3Ta.

With the exception of Ta, all elements added led to a decrease of the onset of melting peaks. This effect allowed in some cases sintering at lower temperatures than used for TNB-V5. As TNB-V5 was prepared from pre-alloyed powder, it did not require a large difference between onset of melting peak and actual sintering temperature to achieve porosities lower than 1%.

Table 15 – Screening Part II, onset of melting peaks and actual sintering temperature applied.

Alloy	Onset of melting peak (°C)	Sintering temperature (°C)
TNB-V5	1497	1500
3Nb-1Mo	1492	1510
3Nb-0.2Gd	1488	1510
1Si	1452	1480
3Nb-1Mo-1Si	1461	1480
3Nb-1Mo-0.2Gd	1490	1510
3Nb-1Mo-1Si-0.2Gd	1446	1470
3Ta	1506	1520

The porosities obtained with the sintering temperatures from Table 15 are plotted in Figure 38. Despite the fairly large standard deviation of some specimens, the porosity values found were rather small (in average lower than 2%). In the case of 3Nb-1Mo that previously required a large amount of elemental aluminium addition (Screening Part I), the porosity level decreased from 5% to nearly 1% with the same sintering parameters. The use of Ti-48Al-3Nb-0.2B-0.2C and Ti-48Al-5Nb-0.2B-0.2C as master alloys led in general to lower porosities in comparison to using TNB-V5 when large elemental aluminium additions were required.

The porosities of the specimens prepared with different types of Gd containing additions are indicated in Figure 38. Using the same sintering parameters, employing $GdSi_2$ led to a larger standard deviation in comparison to pure Gd, however no indication of a change in densification could be found since the sintered porosity was nearly the same. Nevertheless, the use of pure Gd led to a considerable amount of pores that were partially filled with Gd rich particles. This effect could not be observed when $GdSi_2$ was used. A common feature of both kinds of specimens, independent of the type of Gd addition, was the presence of very large pores >100 μm, which were not observed in any other composition.

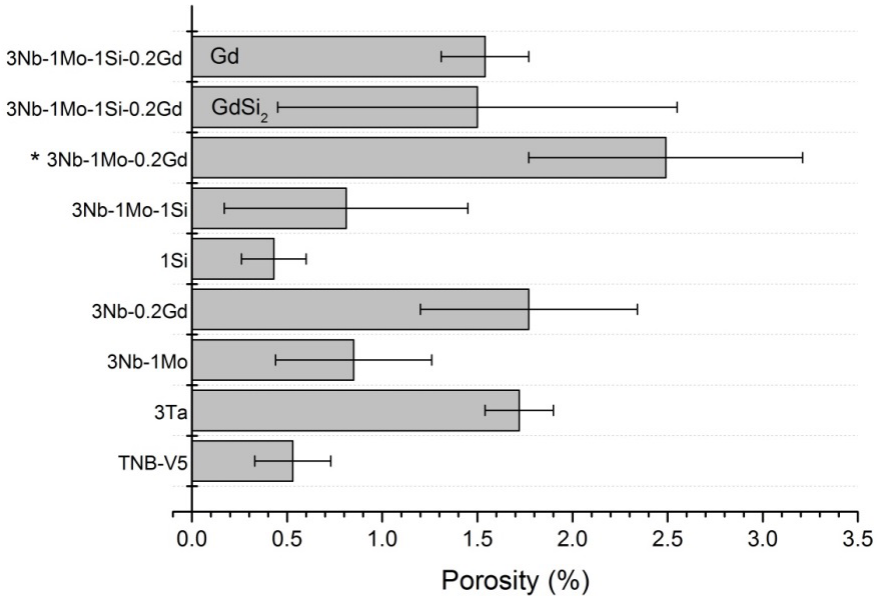

*** Specimen was lightly melted during sintering**

Figure 38 – Screening Part II, porosities obtained with the different alloys prepared with Ti-48Al-3-Nb-0.2B-0.2C and Ti-48Al-5-Nb-0.2B-0.2C as master alloys sintered at various temperatures for 2 hours.

The oxygen and nitrogen levels measured in the sintered specimens are displayed in Table 16. The specimens with addition of pure Gd showed the highest values for oxygen of about 3000 µg/g supporting the assumption that this powder was a strong source of contamination. Using $GdSi_2$ as Gd source for the same alloy reduced the oxygen content below 2000 µg/g. Other alloys that did not contain Gd in their compositions showed oxygen values below 2000 µg/g as well. Nitrogen levels were unaffected by the addition of different elemental powders and remained around 200 µg/g. On the other hand, an oxygen pick-up of at least 800 µg/g took place during specimen preparation.

Table 16 – Screening Part II, oxygen and nitrogen levels of the specimens that were used for mechanical testing.

Alloy	Oxygen (µg/g)	Nitrogen (µg/g)
TNB-V5	2329 ± 67	137 ± 11
3Nb-1Mo	1620 ± 15	169 ± 3
3Nb-0.2Gd	3225 ± 67	203 ± 21
1Si	1529 ± 8	193 ± 4
3Nb-1Mo-1Si	1634 ± 51	187 ± 22
3Nb-1Mo-0.2Gd	2898 ± 56	197 ± 13
3Nb-1Mo-1Si-0.2Gd/Gd	2997 ± 42	225 ± 11
3Nb-1Mo-1Si-0.2Gd/$GdSi_2$	1830 ± 96	145 ± 8
5Nb-3Ta	1253 ± 23	186 ± 2

5.4.2 Microstructures

Selected microstructures obtained with the different alloys are shown in Figure 39, Figure 40 and Figure 41. All microstructures were fully lamellar and shared some common features such as the presence of pores, boride particles and in some cases regions of increased heavy element content. According to EDX measurements, in TNB-V5, these regions are enriched in Nb. In case of compositions with further elemental additions, they are enriched in Nb and the β stabilising elements added (Mo or Ta). The majority of the alloys also showed the presence of the β phase at the colony boundaries (brighter phase). In fact, besides the reference material, only in the specimens 1Si and 3Mo-0.2Gd the retained β phase was not observed.

All the alloy variations showed to some extent inhomogeneous microstructures, even though the sintering temperatures applied were chosen closely to the melting point. A further increase in sintering temperature leads to loss of shape due to extensive formation of liquid phase. In contrast to the porosity levels, the use of Ti-48Al-3Nb-0.2B-0.2C and Ti-48Al-5Nb-0.2B-0.2C as master alloys did not show considerable improvements in the microstructural homogeneity in comparison to employing TNB-V5. For instance, comparing Figure 30 and Figure 39.

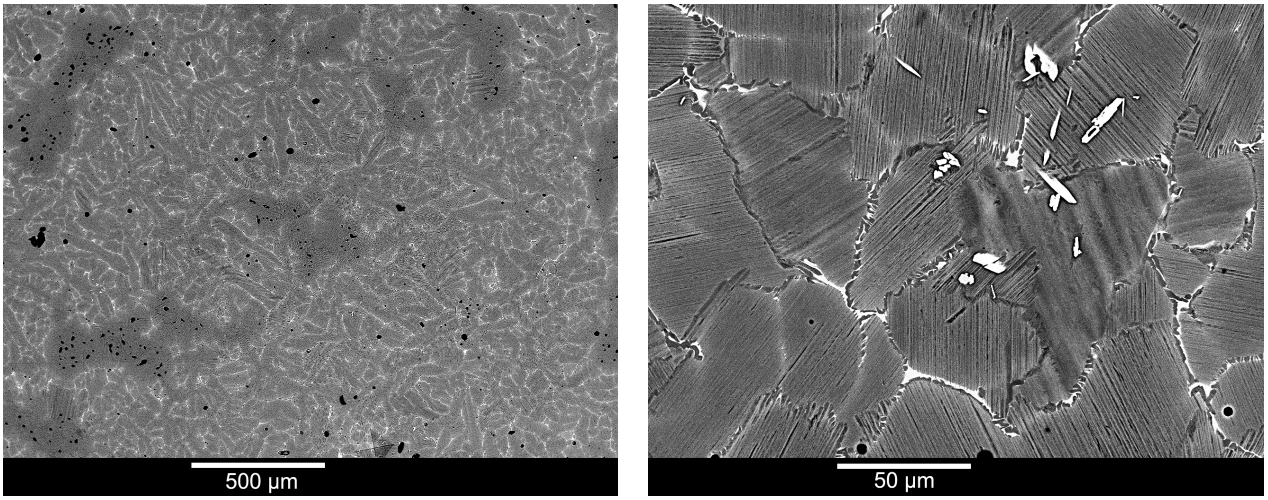

Figure 39 – Screening Part II, microstructure of 3Nb-1Mo sintered at 1510 for 2 hours.

The combination of Nb, Mo and Si in 3Nb-1Mo-1Si (Figure 40), led to a refinement of the microstructure in comparison to TNB-V5, as shown in Figure 42. It also induced the formation of retained β phase mainly at colony boundaries. The Si precipitates were fine and found to be randomly distributed in the microstructure. Similarly, combining Nb, Mo and Gd, as in 3Nb-1Mo-0.2Gd, led to a finer microstructure and formation of retained β phase, as well as smaller precipitates compared with the specimen without Mo.

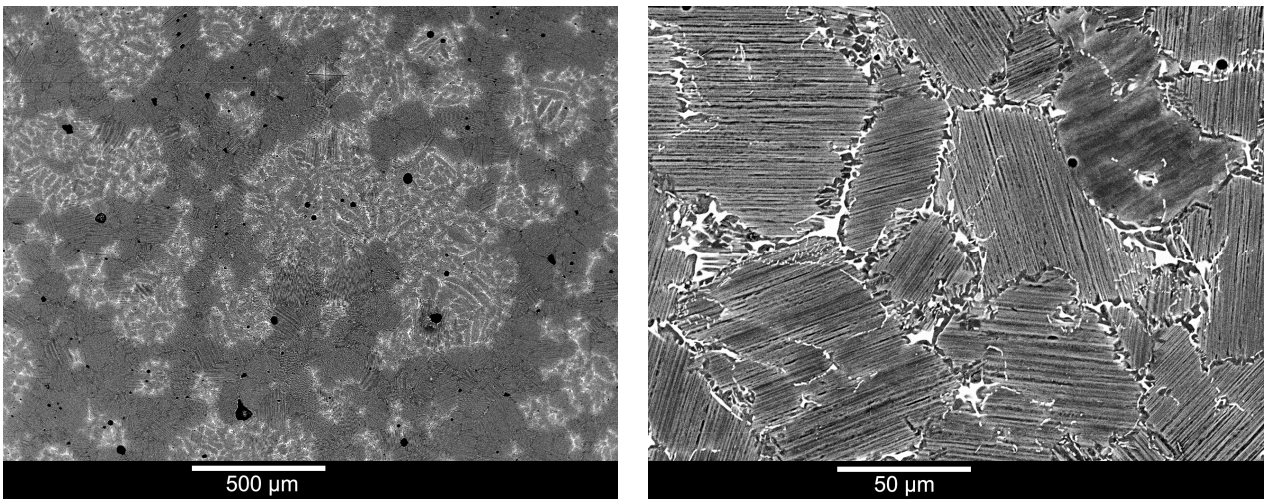

Figure 40 – Screening Part II, 3Nb-1Mo-1Si sintered at 1480 °C for 2 hours.

The alloy containing the largest overall amount of alloying elements was 3Nb-1Mo-1Si-0.2Gd, Figure 41. It was also prepared using two different ways of introducing Gd: pure Gd and a compound containing Si and Gd (gadolinium silicide, $GdSi_2$). The alloy prepared with $GdSi_2$ showed smaller precipitates and also the absence of pores partly filled with Gd rich

particles. Additionally, the Gd precipitates were also more homogeneously distributed. A thickening of the colony boundaries could be identified, indicating a larger amount of γ phase that appears darker in the BSE image due to the lower Ti content than α_2.

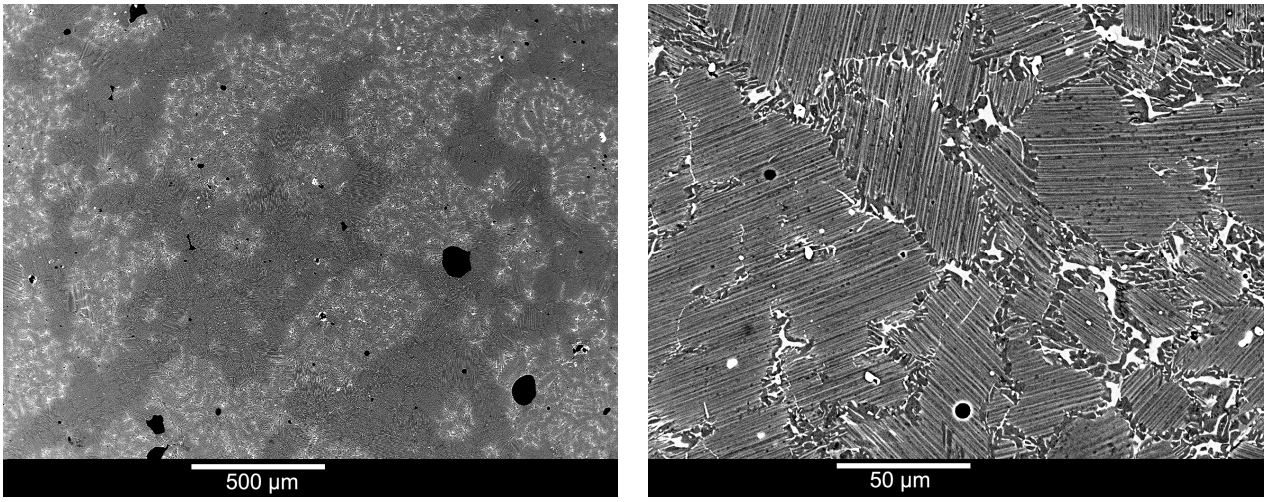

Figure 41 – Screening Part II, 3Nb-1Mo-1Si-0.2Gd prepared with $GdSi_2$ sintered at 1470 °C for 2 hours.

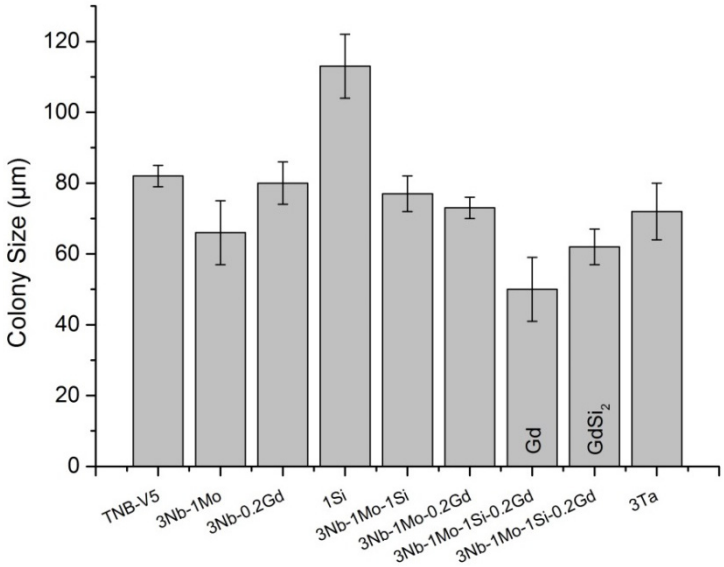

Figure 42 – Screening Part II, colony sizes of alloy variations.

5.4.3 Mechanical properties

The hardness of specimens prepared with Ti-48Al-3Nb-0.2B-0.2C and Ti-48Al-5Nb-0.2B-0.2C as master alloy are displayed in Figure 43. In comparison to TNB-V5, there was a slight increase in hardness with the different alloy variations (with the exception of 3Nb-1Mo-1Si-0.2Gd/$GdSi_2$), however the increment was only marginal and the standard deviations were large.

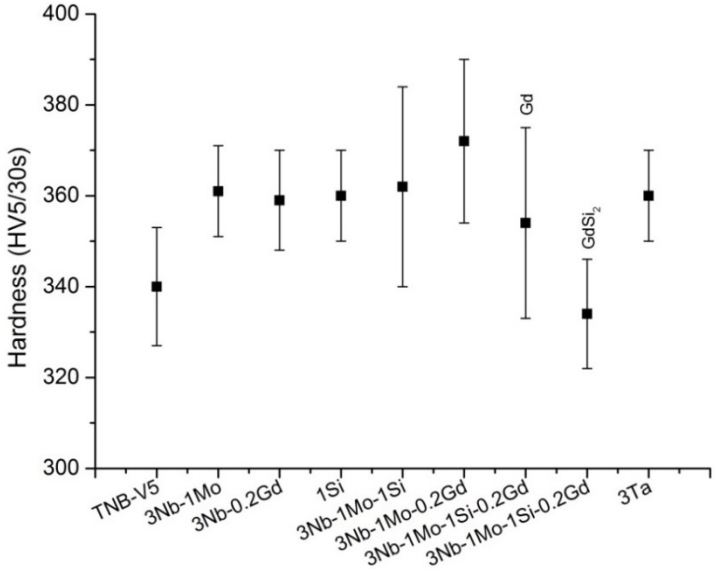

Figure 43 – Screening Part II, hardness values of the different alloy candidates.

The compression creep curves are shown in Figure 44 (a). There was a significant difference of the creep resistance of the alloy candidates in comparison to TNB-V5. The first percentage of plastic deformation occurred in most of the cases completely inside the primary creep regime. However, in the case of the most creep resistant alloys 3Nb-1Mo-1Si and 3Nb-1Mo-1Si-0.2Gd, the secondary creep region already started before reaching 1% deformation.

Figure 44 (b) shows the time to reach a specific plastic deformation under creep conditions. In Screening Part II, two measurements were carried out for each composition in order to assess the experimental deviation. Each extreme of the error bar corresponds to the exact time to 1% strain from each measurement and the columns are the average of both times. Despite the large deviations between the creep tests, it is possible to identify three alloy candidates, 3Nb-1Mo, 3Nb-1Mo-1Si and 3Nb-1Mo-1Si-0.2Gd/$GdSi_2$, with improved primary creep resistance. These compositions were selected for further investigation. Obviously, the error bars were large and often overlapped. Nevertheless, if the averaged times are analysed; the

same outcome as considering the longest times to 1% strain is achieved. Since all alloys were based on variations of 3Nb-1Mo, a new master alloy was chosen for preparing new specimens that is very close to these compositions, namely Ti-44.5Al-3Nb-1Mo-0.2B-0.2C.

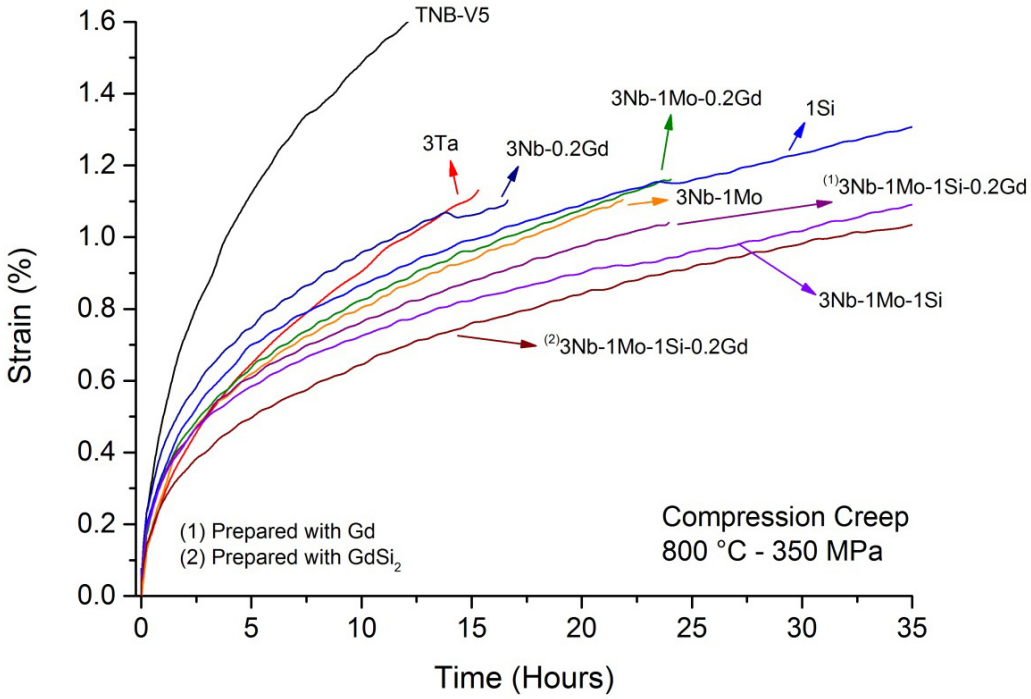

(a)

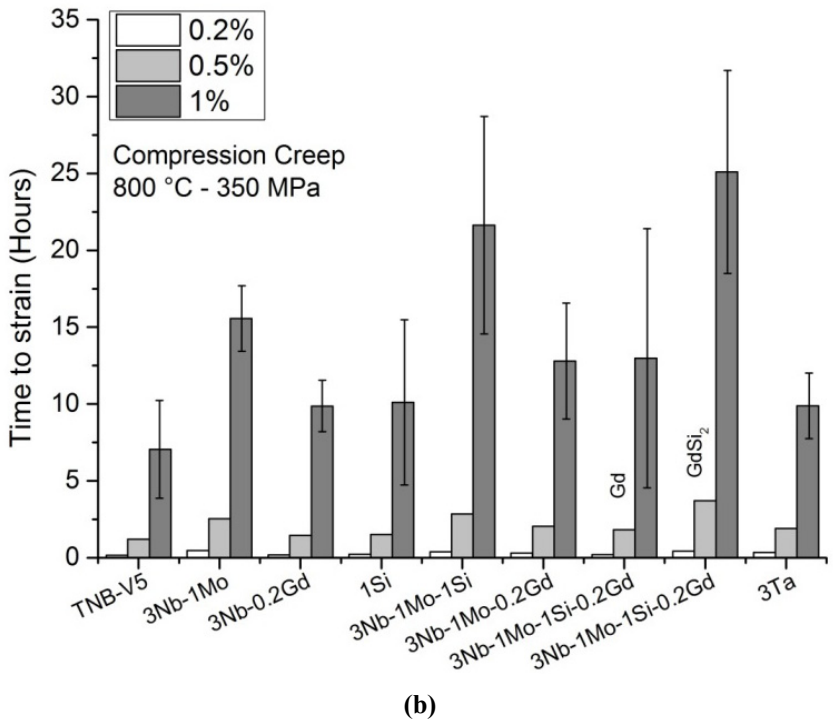

(b)

Figure 44 – Screening Part II, mechanical properties of alloy variations prepared with Ti-48Al-3Nb-0.2B-0.2C and Ti-48Al-5Nb-0.2B-0.2C. (a) Creep strain versus time. (b) Time for a specific amount of plastic deformation.

5.4.4 Summary of Screening Part II

A comparison summarising the most important results from the alloys of Screening Part II is shown in Table 17. Similarly to Screening Part I, the time to 1% strain was the main screening parameter. Notice that for this time the average of two measurements is taken.

Table 17 – Screening Part II, comparative table for the selection of the alloy candidates. A "+" sign means that the quantity evaluated is higher/larger than the reference material.

Alloy	Time to 1% strain (hours)	Microstructural homogeneity	Colony Size	Porosity
TNB-V5	7.5	Reference	Reference	Reference
3Nb-1Mo	15	-	-	0
1Si	10	-	+	0
3Nb-0.2Gd	10	-	0	+
3Ta	10	-	0	+
3Nb-1Mo-1Si	22	-	0	0
3Nb-1Mo-0.2Gd	12.5	-	0	+
3Nb-1Mo-1Si-0.2Gd/Gd	12.5	-	-	+
3Nb-1Mo-1Si-0.2Gd/$GdSi_2$	25	-	-	0

5.5 Final Alloy Candidates

In this section, the results of specimens prepared with the new base system Ti-44.5Al-3Nb-1Mo-0.2B-0.2C are presented. After the careful screening of alloying elements based mainly on the primary creep resistance in compression, three final candidate alloys were selected for further investigation: 3Nb-1Mo, 3Nb-1Mo-1Si and 3Nb-1Mo-1Si-0.2Gd. In addition to Uniaxial Pressing (UP), these alloys were also prepared by Metal Injection Moulding (MIM).

5.5.1 Sintering behaviour

In order to make a better estimate of the sintering temperatures, DSC measurements were conducted to identify the onset of the melting peaks of the different alloys. As previously

done in Screening Part II, sintering was conducted at temperatures above the onset of the melting peaks, shown in Table 18.

The difference between the actual sintering temperature and the onset of the melting peak was lower than in Screening Part II, in which more elemental additions were necessary. The sintering temperatures were chosen based on preliminary sintering experiments with each alloy. The onsets of melting peaks were also found to be slightly higher than the ones obtained with Ti-48Al-3Nb-0.2B-0.2C and Ti-48Al-5Nb-0.2B-0.2C, respectively, as master alloys.

Table 18 – Final Alloy Candidates, onset of melting peaks and actual sintering temperatures applied.

Alloy	Onset of melting peak (°C)	Sintering temperature (°C)
TNB-V5	1497	1500
3Nb-1Mo	1502	1510
3Nb-1Mo-1Si	1462	1470
3Nb-1Mo-1Si-0.2Gd	1460	1465

The porosities obtained with the sintering temperatures from Table 18 are displayed in Figure 45. In all materials the porosities were considerably low porosities (smaller than 1% in average), which further supports the finding that there is a direct relationship between the amount of elemental powders added and the residual porosity in sintered parts (similar to Screening Part II).

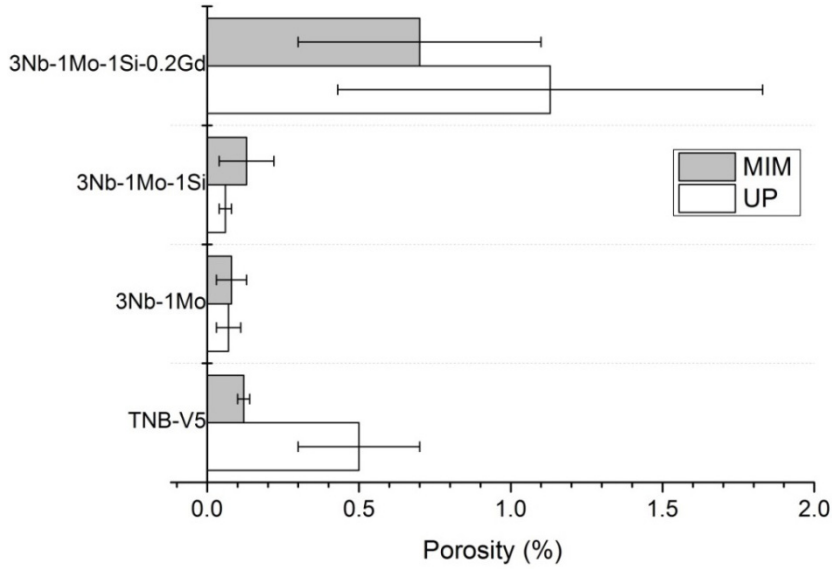

Figure 45 – Final Alloy Candidates, porosities of specimens prepared with Ti-44.5Al-3Nb-1Mo-0.2B-0.2C as master alloy sintered at various temperatures for 2 hours. Uniaxial Pressing (UP) and Meltal Injection Molding (MIM).

The oxygen and nitrogen levels of sintered specimens are shown in Table 19. Specimens prepared by MIM showed lower oxygen values (around 1500 μg/g) in comparison to Uniaxial Pressing (above 2000 μg/g). The nitrogen levels were in most cases around 200 μg/g and it seems that MIM also delivered lower values than UP.

The carbon contents are difficult to control in the powder metallurgical techniques used to prepare the specimens (MIM and UP) due to the presence of the organic binder required for shaping. Consequently, the values were presented only for the MIM specimens in order to give an idea about the final carbon contents. The starting carbon value (0.2 at.%) accounts for 600 μg/g, therefore it is clear that carbon pick-up occurred during the process.

Table 19 – Final Alloy Candidates, oxygen, nitrogen and carbon levels of specimens that were used for mechanical testing.

Alloy		Oxygen (µg/g)	Nitrogen (µg/g)	Carbon (µg/g)
MIM	TNB-V5	1780 ± 28	258 ± 5	751 ± 87
	3Nb-1Mo	1555 ± 42	150 ± 24	1192 ± 8
	3Nb-1Mo-1Si	1536 ± 53	165 ± 9	1237 ± 64
	3Nb-1Mo-1Si-0.2Gd	1409 ± 322	205 ± 6	926 ± 96
UP	TNB-V5	2329 ± 67	137 ± 11	--
	3Nb-1Mo	2619 ± 32	199 ± 4	--
	3Nb-1Mo-1Si	2230 ± 40	431 ± 40	--
	3Nb-1Mo-1Si-0.2Gd	2518 ± 140	412 ± 10	--

5.5.2 Microstructures

Figure 46 displays microstructures obtained with sintered MIM specimens. The microstructural homogeneity was markedly improved in comparison to the specimens prepared previously. The main difference was the amount of elemental powders added, which was larger in the case of Screening Part I and II. In the Final Alloy Candidates, only the additions of Si and $GdSi_2$ in the form of elemental powders were necessary.

All alloys showed a fully lamellar microstructure with the presence of borides and pores. TNB-V5 also exhibited the presence of Nb microsegregations, as previously observed. All alloy variants showed a refined microstructure in comparison to TNB-V5 with 3Nb-1Mo-1Si displaying the smallest colonies in the order of 40 µm. There was statistically no difference in colony size comparing MIM and UP, as shown in Figure 47. The Final Alloy Candidates also showed the presence of retained β at colony boundaries.

The specimens containing Si and Gd, as previously observed, exhibited homogeneously distributed precipitates of various sizes. The colony boundaries, however, showed distinct morphologies due to the presence of retained β phase and colony boundary γ grains. On the specimen with $GdSi_2$ addition, very large pores >100 µm were again formed, as observed in Screening Part II.

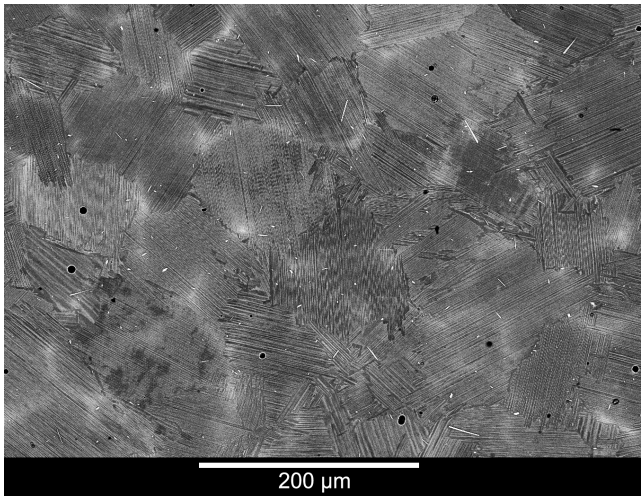

(a) TNB-V5 sintered at 1500 °C for 2 hours.

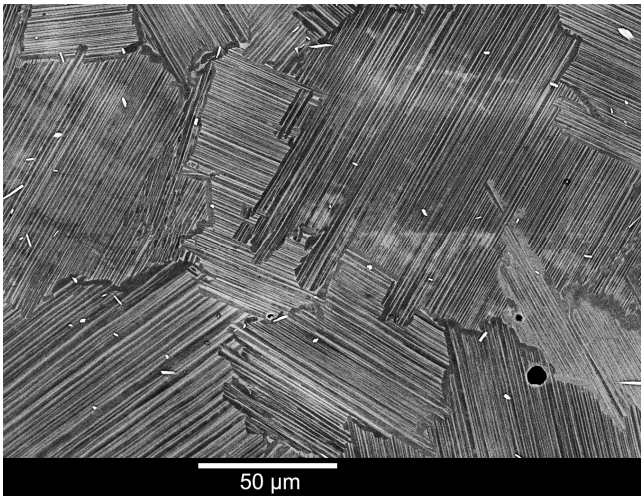

(b) TNB-V5 sintered at 1500 °C for 2 hours.

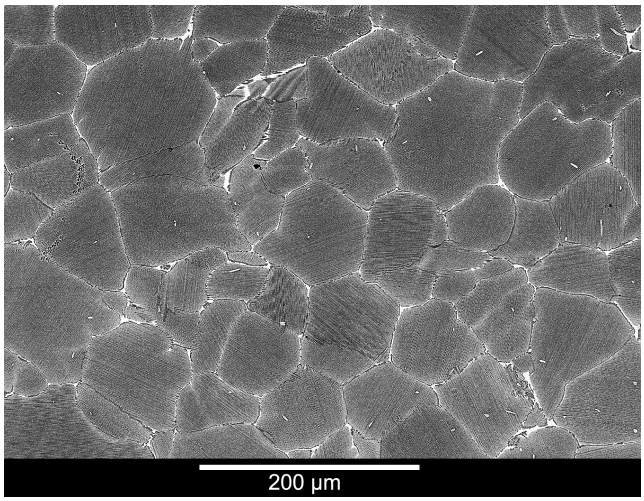

(c) 3Nb-1Mo sintered at 1510 °C for 2 hours.

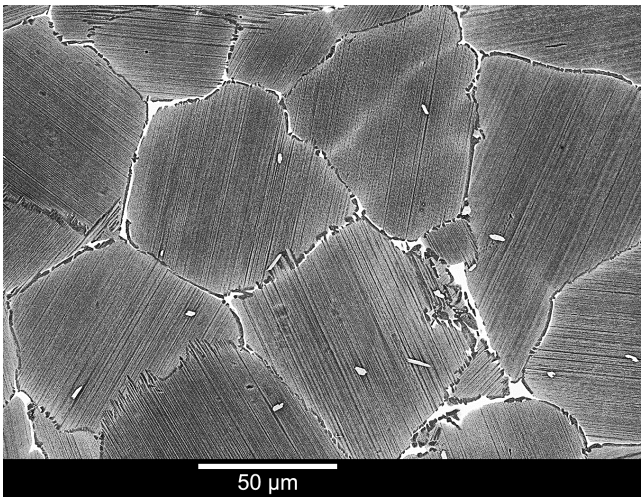

(d) 3Nb-1Mo sintered at 1510 °C for 2 hours.

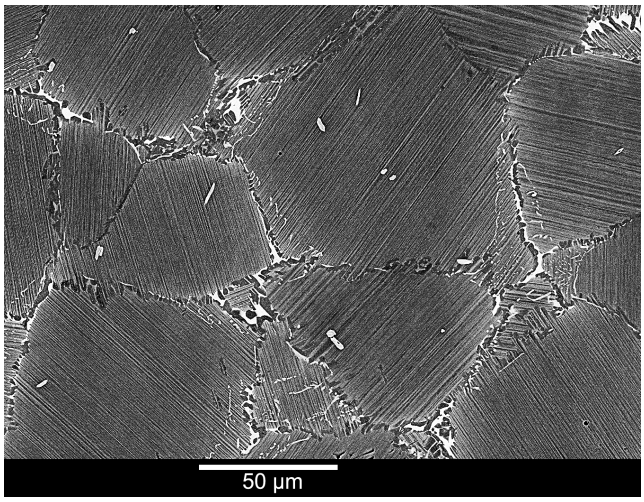

(e) 3Nb-1Mo-1Si sintered at 1470 °C for 2 hours.

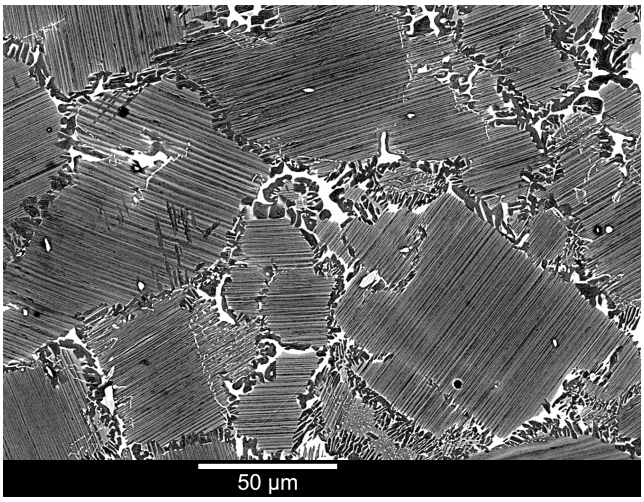

(f) 3Nb-1Mo-1Si-0.2Gd sintered at 1465 °C for 2 hours.

Figure 46 – Final Alloy Candidates, microstructures of specimens prepared by MIM.

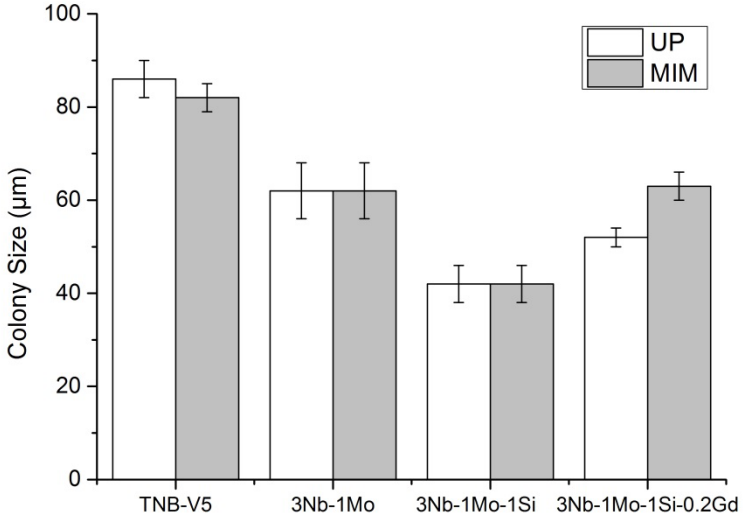

Figure 47 – Final Alloy Candidates, colony size of the different alloys prepared by Uniaxial Pressing (UP) and Metal Injection Moulding (MIM).

5.5.3 Mechanical properties

5.5.3.1 At room temperature

The Vickers hardness of the Final Alloy Candidates is shown in Figure 48. In both conditions (MIM and UP) all alloy candidates achieved in average higher values than TNB-V5. The improvement was however limited to about 10%. In comparison to the measurements from Screening Part II, the hardness values in general improved for each particular composition, which arises as a direct effect of the reduced porosity and improved microstructural homogeneity.

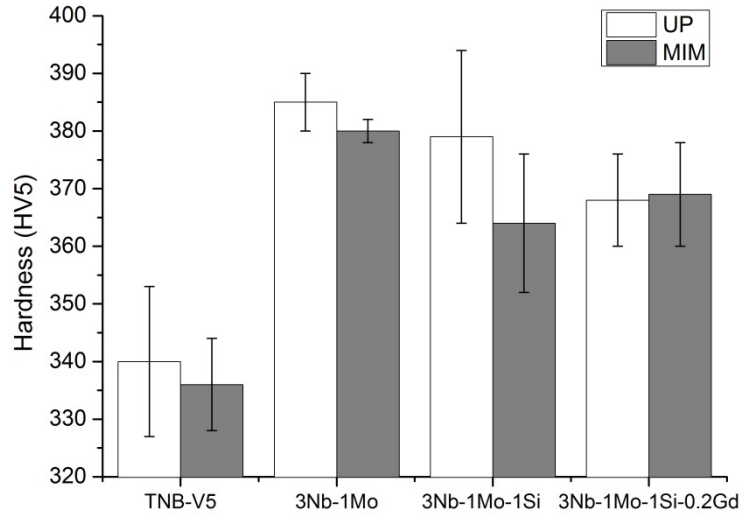

Figure 48 – Final Alloy Candidates, hardness values.

The tensile properties of the Final Alloy Candidates are displayed in Table 20. The alloy 3Nb-1Mo-1Si showed the highest ultimate tensile stress, while TNB-V5 and 3Nb-1Mo displayed overlapping error bars. On the other hand, 3Nb-1Mo-1Si-0.2Gd showed the lowest UTS at room temperature and the lowest strain to failure, which indicates an embrittlement due to the precipitates and the large pores. The plastic strain was highest for TNB-V5 followed by 3Nb-1Mo. Addition of precipitates only decreased the plastic strain and the alloy 3Nb-1Mo-1Si-0.2Gd showed no measurable plastic elongation.

Table 20 – Tensile properties at room temperature from Final Alloy Candidates. The plastic strain of 3Nb-1Mo-1Si-0.2Gd could not be determined.

Alloy	UTS (MPa)	Strain at fracture (%)	Plastic Strain (%)
TNB-V5	570 ± 1	0.5 ± 0.01	0.12 ± 0.01
3Nb-1Mo	571± 17	0.5 ± 0.01	0.10 ± 0.03
3Nb-1Mo-1Si	607± 10	0.5 ± 0.0	0.08 ± 0.02
3Nb-1Mo-1Si-0.2Gd*	445	0.25	0

*** Result of a single measurement.**

5.5.3.2 Creep measurements at 800 °C – 350 MPa

Compression creep behaviour of alloys prepared with the new base system is displayed in Figure 49. The alloy candidates showed a modest increase in compression creep resistance in comparison to TNB-V5. With the exception of 3Nb-1Mo-1Si-0.2Gd possibly as an effect of the presence of large pores, the same trend as in Screening Part II was observed. The alloys 3Nb-1Mo and 3Nb-1Mo-1Si showed improved primary creep resistance in comparison to the reference material.

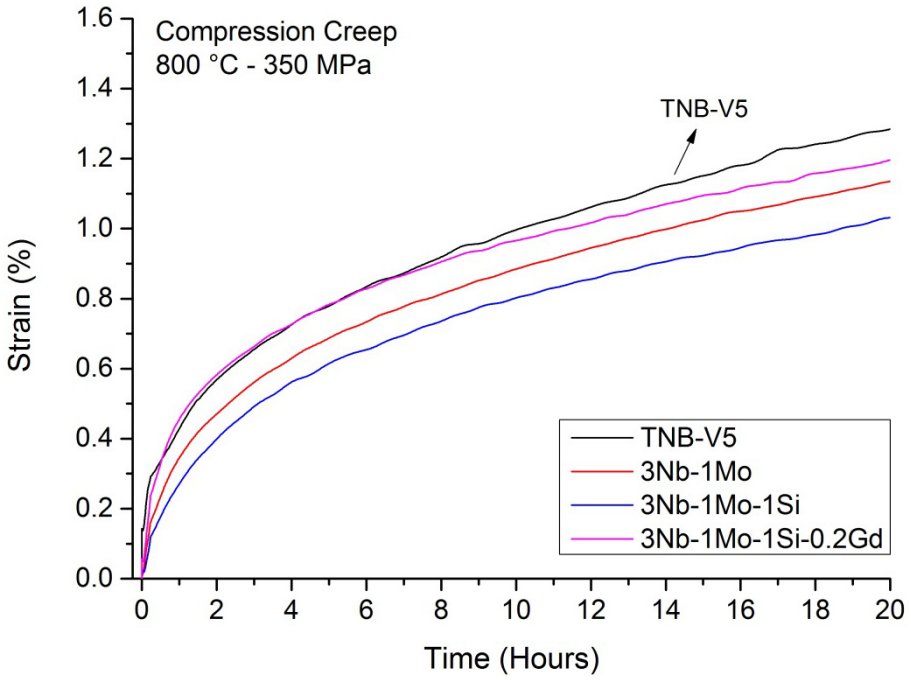

(a)

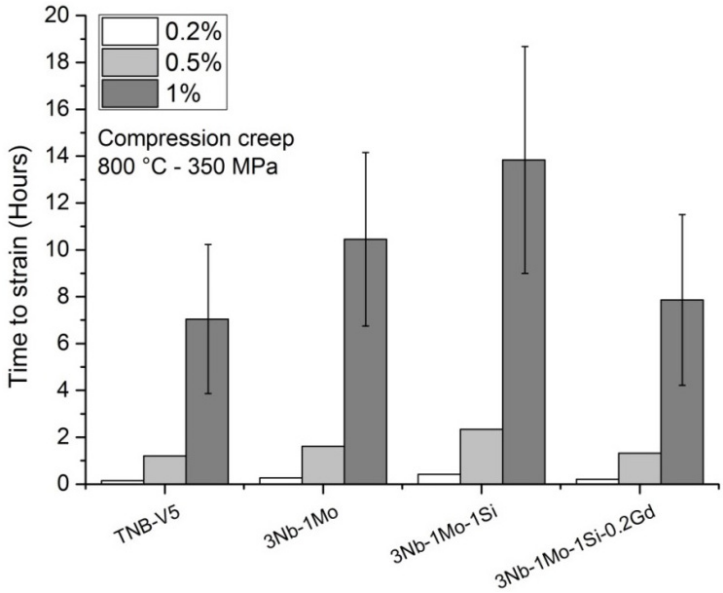

(b)

Figure 49 – Final Alloy Candidates, (a) Creep strain versus time. (b) Time for a specific amount of plastic deformation.

Tensile creep behaviour of MIM specimens is displayed in Figure 50. There was a great difference in creep life between TNB-V5 and 3Nb-1Mo-1Si, which took double as much time for rupture. 3Nb-1Mo and 3Nb-1Mo-1Si-0.2Gd showed shorter creep lives than 3Nb-1Mo-1Si but longer than TNB-V5. The lowest minimum creep rate of about $2x10^{-7}$ 1/s was measured with the composition 3Nb-1Mo-1Si. TNB-V5 showed the highest value for the minimum creep rate of around $5x10^{-7}$ 1/s.

In regard to primary creep resistance, an improvement was achieved by all alloy candidates. 3Nb-1Mo-1Si-0.2Gd showed a factor 2 in comparison to TNB-V5 for the time to reach 1% plastic strain. The amount of plastic deformation contained in the primary creep region was lowest for 3Nb-1Mo-1Si-0.2Gd (1%) and highest in the case of 3Nb-1Mo and 3Nb-1Mo-1Si (2.5%).

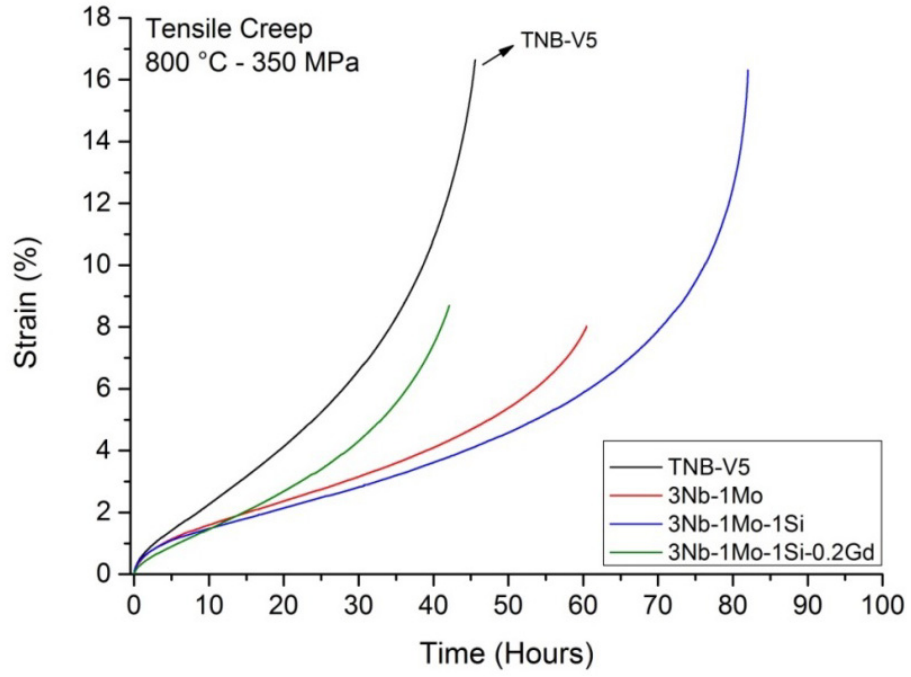

(a)

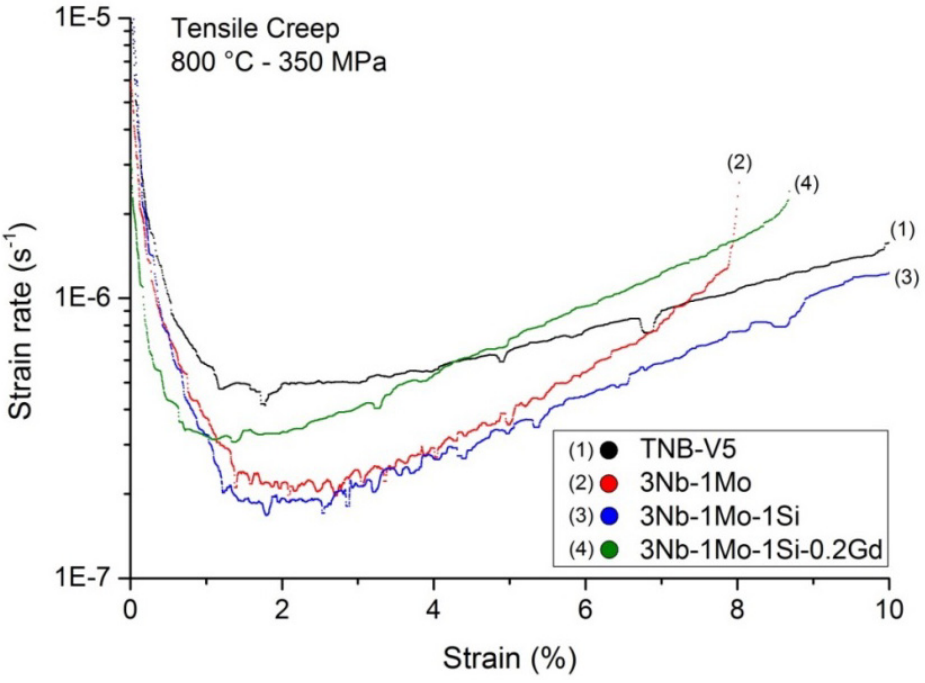

(b)

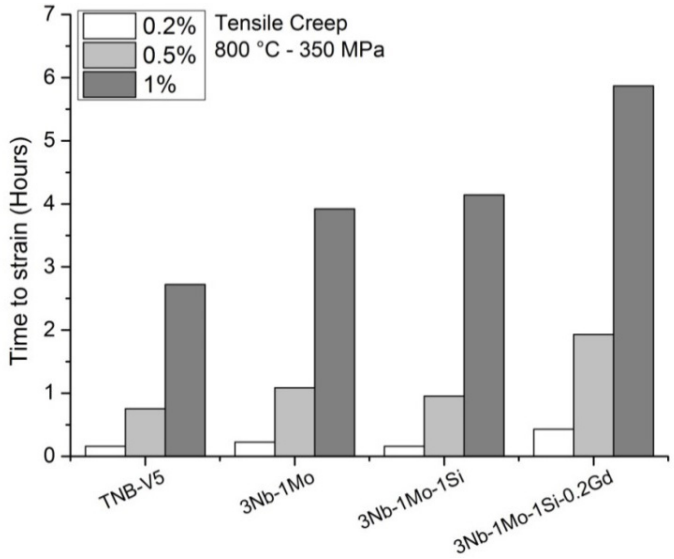

(c)

Figure 50 – Final Alloy Candidates, tensile creep test at 800 °C and 350 MPa. (a) Creep strain versus time. (b) Creep rate as a function of creep strain determined from the creep curves. (c) Time for a specific amount of plastic deformation.

5.5.3.3 Creep measurements at 900 °C – 100 MPa

The creep behaviour at 900 °C and 100 MPa is displayed in Figure 51. The creep life of TNB-V5 was the longest with 300 hours until rupture, while 3Nb-1Mo-1Si broke after about 160 hours. 3Nb-1Mo-1Si showed the lowest minimum creep rate of about $9x10^{-8}$ 1/s.

With respect to primary creep, 3Nb-1Mo-1Si was the most resistant alloy followed by TNB-V5 by only a small difference. The alloys 3Nb-1Mo and 3Nb-1Mo-1Si-0.2Gd at these creep testing conditions showed lower performance than the reference material. The amount of plastic deformation contained in the primary creep region was lowest for 3Nb-1Mo-1Si-0.2Gd (1.2%) and highest in the case of TNB-V5 (3.3%).

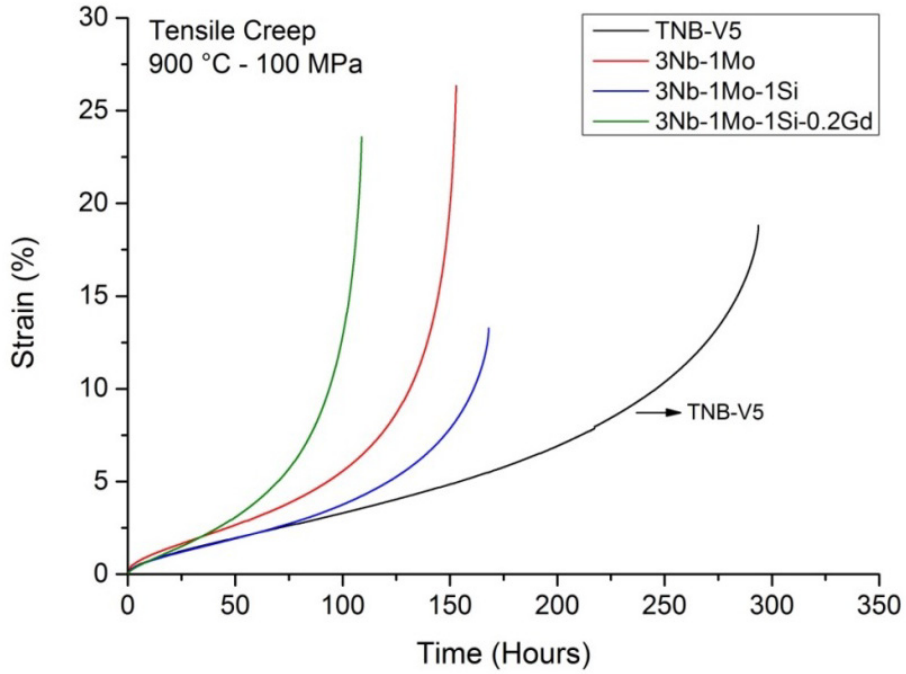
Tensile Creep
900 °C - 100 MPa
TNB-V5
3Nb-1Mo
3Nb-1Mo-1Si
3Nb-1Mo-1Si-0.2Gd
TNB-V5
Strain (%)
Time (Hours)
0
5
10
15
20
25
30
0
50
100
150
200
250
300
350

(a)

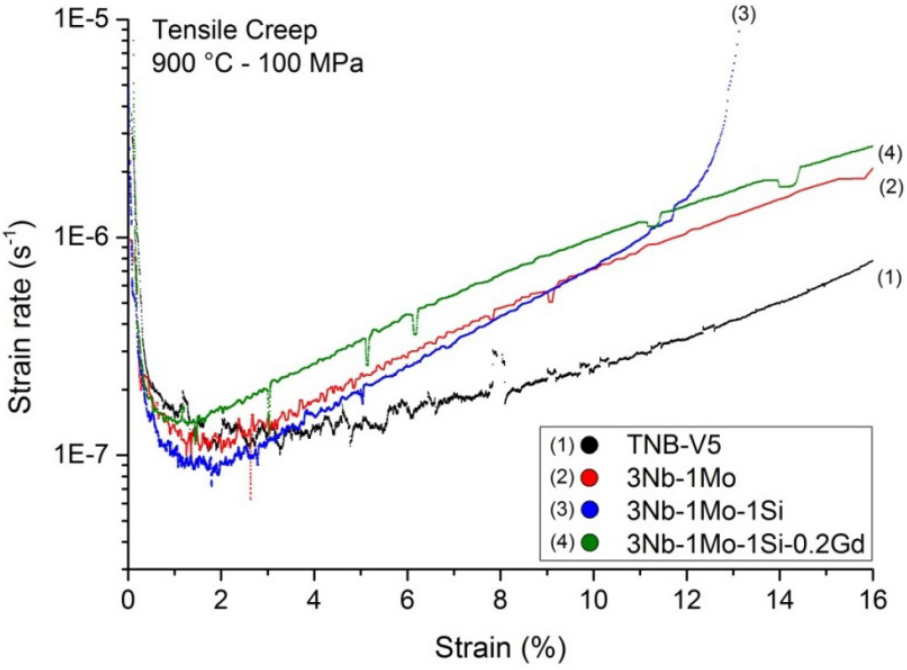
Tensile Creep
900 °C - 100 MPa
(1) TNB-V5
(2) 3Nb-1Mo
(3) 3Nb-1Mo-1Si
(4) 3Nb-1Mo-1Si-0.2Gd
Strain rate (s-1)
Strain (%)
1E-5
1E-6
1E-7
0
2
4
6
8
10
12
14
16

(b)

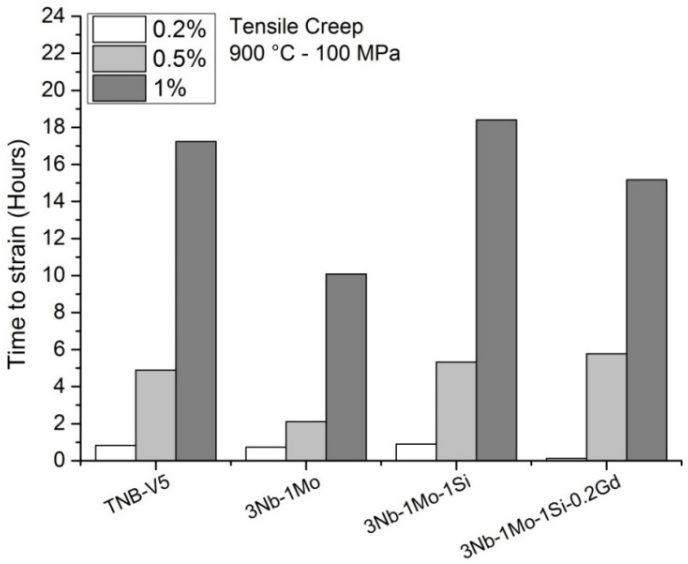

(c)

Figure 51 – Final Alloy Candidates, creep behaviour at 900 °C and 100 MPa. (a) Creep strain versus time. (b) Creep rate as a function of creep strain determined from the creep curves. (c) Time for a specific amount of plastic deformation.

5.5.3.4 Creep measurements at 950 °C – 200 MPa

The creep behaviour at 950 °C and 200 MPa loading is shown in Figure 52. The creep curves of TNB-V5 and 3Nb-1Mo-1Si were similar and overlapped at the end of the creep life. The compositions 3Nb-1Mo and 3Nb-1Mo-1Si-0.2Gd showed shorter creep life than the reference material. The lowest minimum creep rate of about $5x10^{-6}$ 1/s was measured with the composition 3Nb-1Mo-1Si.

The primary creep resistance of all alloys was fairly similar with the exception of 3Nb-1Mo-1Si-0.2Gd that crept twice as fast until 1% plastic strain. 3Nb-1Mo-1Si took the longest time to reach 1% plastic deformation, which was about 0.4 hours. The amount of plastic deformation accumulated in the primary creep region was lowest for 3Nb-1Mo-1Si-0.2Gd (1%), while TNB-V5, 3Nb-1Mo and 3Nb-1Mo-1Si were in the same range of about 1.3-1.5%.

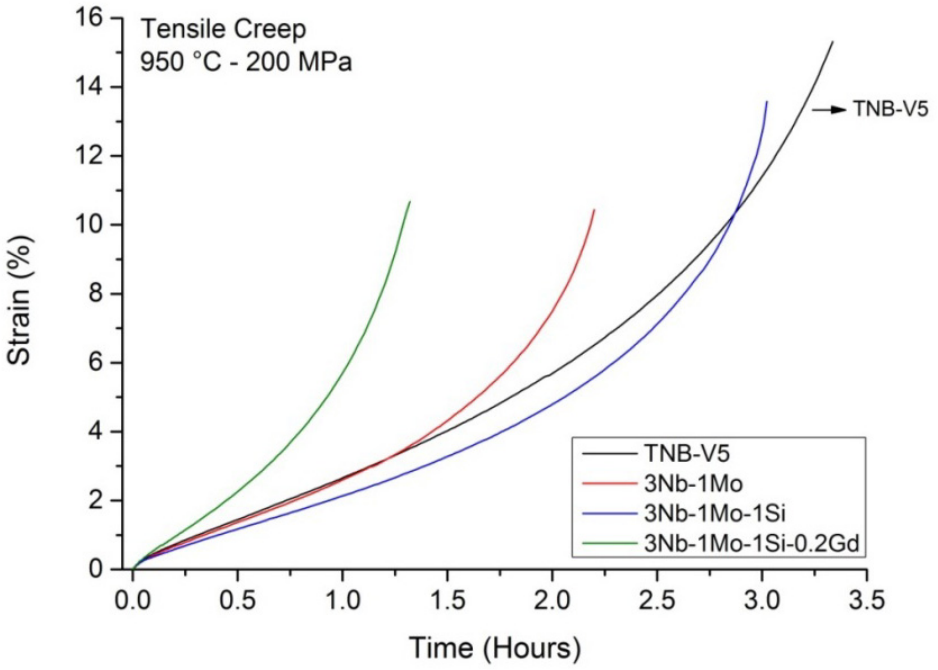
Tensile Creep
950 °C - 200 MPa
TNB-V5
Strain (%)
Time (Hours)
TNB-V5
3Nb-1Mo
3Nb-1Mo-1Si
3Nb-1Mo-1Si-0.2Gd

(a)

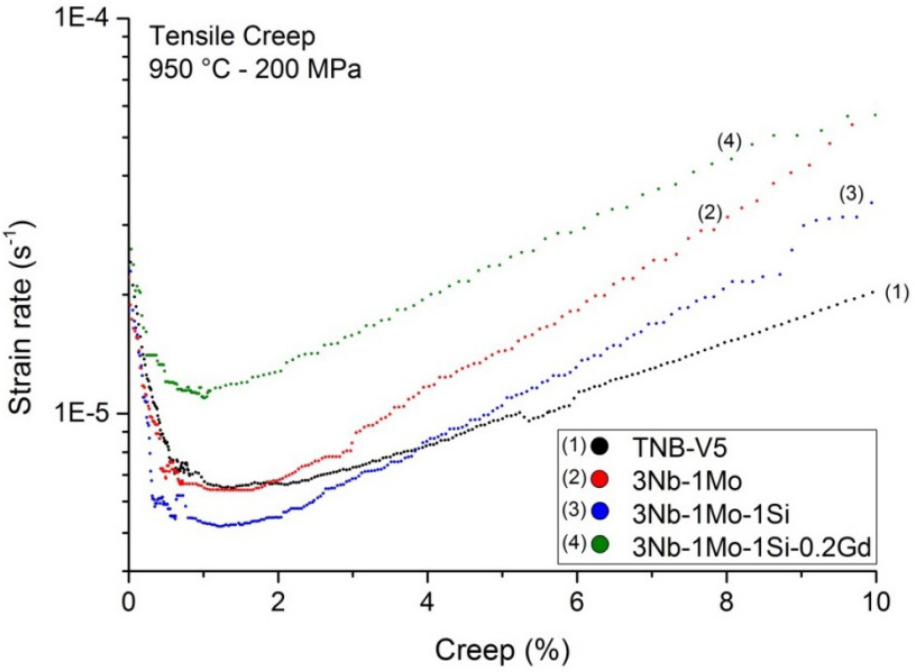
Tensile Creep
950 °C - 200 MPa
Strain rate (s-1)
Creep (%)
(1) TNB-V5
(2) 3Nb-1Mo
(3) 3Nb-1Mo-1Si
(4) 3Nb-1Mo-1Si-0.2Gd

(b)

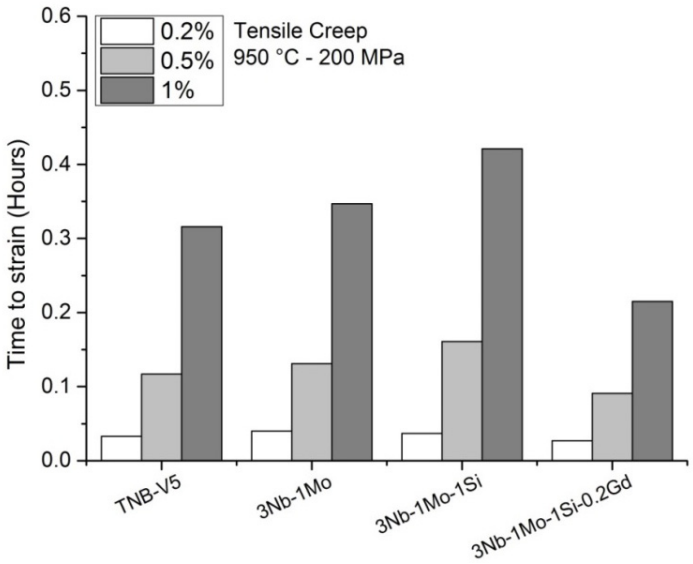

(c)

Figure 52 – Final Alloy Candidates, creep behaviour at 950 °C and 200 MPa. (a) Creep strain versus time. (b) Creep rate as a function of creep strain determined from the creep curves. (c) Time for a specific amount of plastic deformation.

6. Structural characterisation

6.1.1 Final Alloy Candidates

X-Ray diffraction patterns of the different alloys measured in the as-sintered condition are displayed in Figure 53. TNB-V5 and 3Nb-1Mo show peaks of γ and α_2, while 3Nb-1Mo-1Si and 3Nb-1Mo-1Si-0.2Gd also contain peaks corresponding to a titanium silicide (Ti_5Si_3) and the β phase.

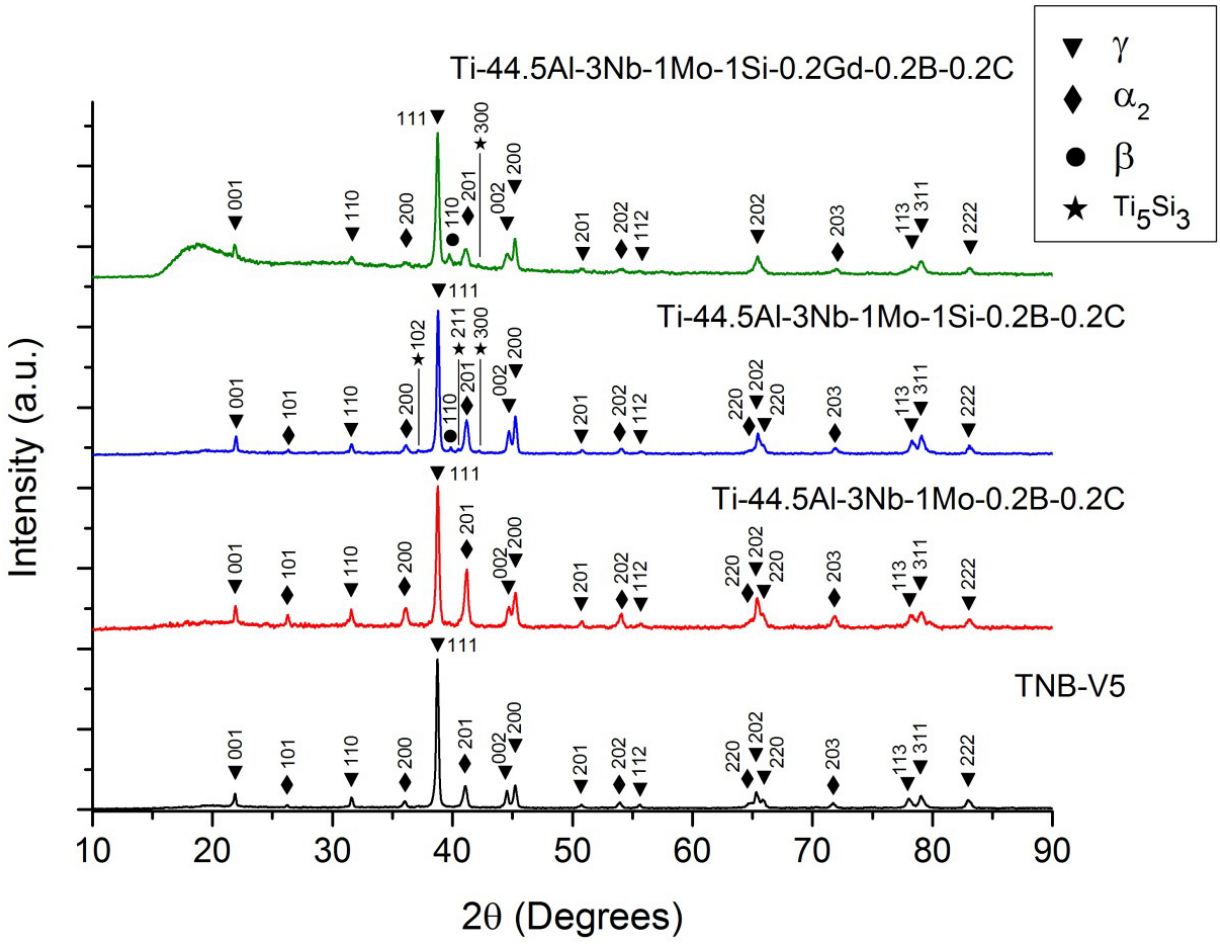

Figure 53 – Final Alloy Candidates, XRD patterns from the different alloys measured in the as-sintered condition.

Phase fractions of as-sintered specimens determined from the XRD patterns are shown in Table 21. TNB-V5 showed the highest fraction of γ phase, while 3Nb-1Mo showed the highest amount of α_2 phase. The additions of Si and Gd induced the formation of small amounts of Ti_5Si_3 and β phase, which were formed at the expense of the γ phase. The α_2 phase fraction remained similar to TNB-V5.

Table 21 – Phase fractions of Final Alloy Candidates in percentage of the different alloys determined from the XRD patterns.

Alloy	α_2	γ	β	Ti_5Si_3
TNB-V5	18	82	-	-
3Nb-1Mo	31	69	-	-
3Nb-1Mo-1Si	19	77	2	3
3Nb-1Mo-1Si-0.2Gd	19	69	8	5

6.1.2 Specimens after creep test

In order to have a rough idea of the phase transformations taking place during creep testing, ruptured specimens were also examined with XRD. The phase fractions determined from the diffraction patterns are shown in Table 22.

TNB-V5 showed an increase of the α_2 phase fraction at the expense of the γ phase in both creep testing conditions analysed. In contrast, 3Nb-1Mo remained fairly similar and only a slight increase in the β phase fraction was noticeable as a function of the creep temperature. However, a significant decrease in the α_2 phase fraction took place. In comparison to the as-sintered condition it decreased from 31 to 23-24%.

3Nb-1Mo-1Si showed a considerable decrease in the α_2 fraction as a function of the creep temperature, which is associated with an increase in the β and Ti_5Si_3 phase fractions. A similar phase transformation could be seen with the specimen 3Nb-1Mo-1Si-0.2Gd, indicating the dynamic precipitation of Ti_5Si_3.

Table 22 – Phase fractions of Final Alloy Candidates in percentage from the different alloys measured after creep testing.

Creep testing condition	800 °C – 350 MPa				900 °C – 100 MPa			
Alloy/Phase	**α_2**	**γ**	**β**	**Ti_5Si_3**	**α_2**	**γ**	**β**	**Ti_5Si_3**
TNB-V5	21	79	-	-	30	70	-	-
3Nb-1Mo	23	75	1	-	24	72	3	-
3Nb-1Mo-1Si	17	76	3	4	13	74	4	9
3Nb-1Mo-1Si-0.2Gd	21	72	4	3	12	76	6	6

6.1.3 Precipitates

To measure the peaks corresponding to the precipitates in higher resolution, HEXRD was conducted. The results are shown in Figure 54. Two different specimens containing additions of Si and Si+Gd were analysed. Peaks corresponding to the α_2, γ and β phases were found in both cases, however some additional peaks were also present.

In the case of Si addition, Figure 54 (a), the additional peaks could be successfully indexed as the ζ phase, Ti_5Si_3. With Gd and Si additions, in addition to the ζ phase, peaks corresponding to Gd oxides were also found. The oxides particles could not be indexed as a single phase but rather as a mixture of oxides of Gd_2TiO_5 and GdTiO type.

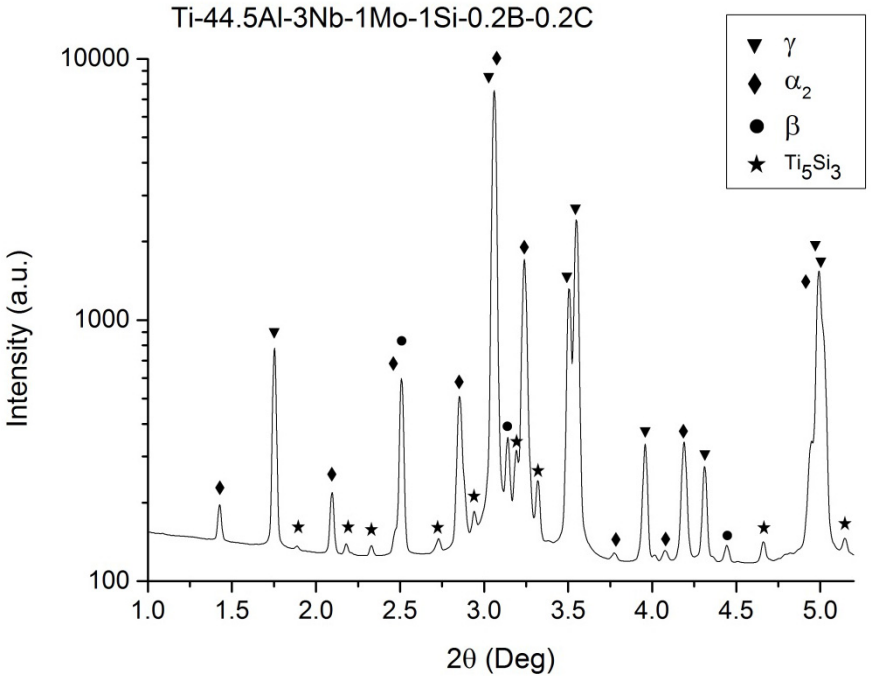

(a)

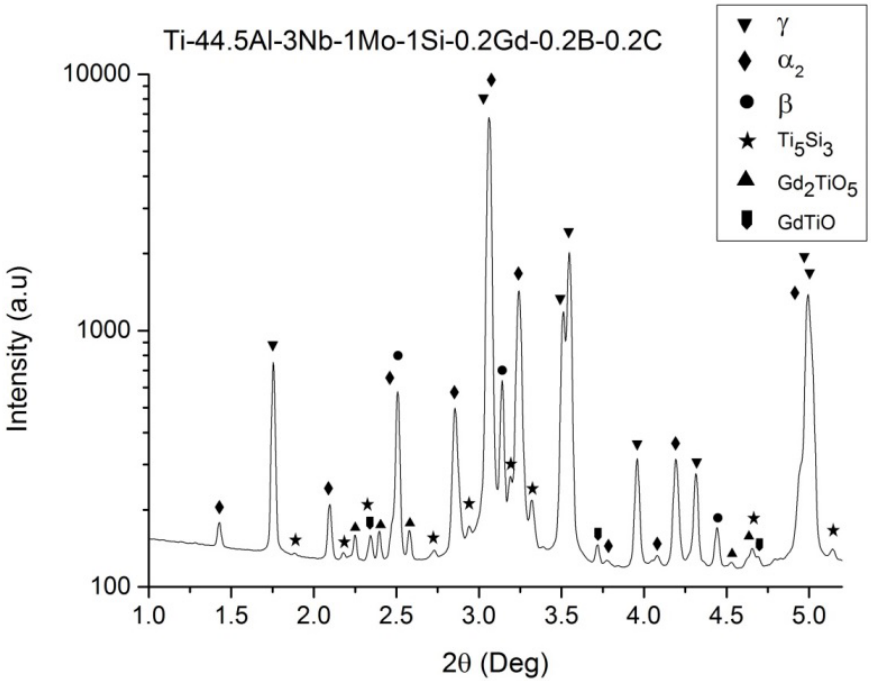

(b)

Figure 54 – HEXRD for the characterisation of precipitates. (a) Specimen with Si addition. (b) Specimen with Si and Gd addition.

7. Discussion

In this section the important aspects of the results will be discussed and compared with the available literature. Considering that the alloys investigated are intended for MIM processing, the discussion is focused at first on the sintering behaviour and different approaches for the reduction of residual porosity. Lastly the primary creep resistance is related to the achievable as-sintered microstructures via MIM and the effects of the alloying elements in the most promising alloy candidates are discussed.

7.1 Some aspects of processing titanium aluminides by powder metallurgy

7.1.1 Microstructure formation during sintering

In the green condition, the MIM specimens contain powder particles that are held together by the binder, which provides some mechanical strength necessary for handling. As the specimen is chemical and thermally debinded, the fine powder particles start to connect. As the temperature is further increased, the sintering process proceeds and, in the case of TNB-V5, ultimately leads to a nearly fully dense microstructure. Titanium aluminides undergo all three stages of sintering. Firstly the powder particles come together forming necks, then the necks grow and finally the part becomes dense with only little residual porosity left [188]. However, simultaneously with the heating and cooling stages of the sintering process, the various solid state transformations described in the binary phase diagram take place [59], which can critically affect the sintered microstructure, especially during cooling.

As can be seen in Figure 26, for the case of TNB-V5, the beginning of the downward slope in the length change curve (ΔL) started at relatively low temperatures that were close to the pre-sintering temperature. This indicates that the initial stage of sintering already took place at the pre-sintering temperature. Consequently, the change in length as a function of temperature can only be considered after that point.

Even though the precise discrimination between each stage of sintering is difficult, it is feasible to assume that at temperatures around 1300 °C the intermediate stage is reached. Pores at the intermediate stage become smooth but remain interconnected and the initial shape of the necks is lost [188]. As displayed in Figure 17 from the feasibility study, the pore structure and the size of the necks formed during pre-sintering at 1300 °C support that fact.

The slight change in the slope of the shrinkage curve between 1250 and 1300 °C could have originated due to the changes of the heating rate (sinter profile) and due to the eutectoid reaction ($\alpha_2 + \gamma \rightarrow \alpha + \gamma$) and subsequent crossing of the single α phase field ($\alpha + \gamma \rightarrow \alpha$).

The analysis of the sintered density in Table 12 shows that the porosity changes from 8.9% to 3.3% for specimens sintered at 1460 °C and 1470 °C, respectively. A change in the pore structure from smooth interconnected to isolated and closed ones followed by residual porosities in the order of 5% characterises the start of final stage sintering [188]. Consequently, at temperatures around 1460 °C the final stage sintering is reached. The greatest change in the shrinkage curve at around 1450 °C occurs due to the phase transformation $\alpha \rightarrow \alpha + \beta$ and followed possibly by the transition into the single β phase field. Diffusion in β titanium is faster than in the α or γ phases [189], therefore the shrinkage rate was also considerably increased.

Table 12 additionally shows that little change in the densification of TNB-V5 takes place between 1480 °C and 1510 °C. In fact, the mechanical properties of TNB-V5 sintered at 1480 °C would probably suffice for many load bearing applications. However, sintering at higher temperatures, e.g. 1500 °C, leads to the formation of rounder pores, which further improves the mechanical properties due to a decrease in local stress concentration at pore rims.

The roundness of pores can be evaluated by a parameter called shape factor, which corresponds to a numeric comparison between the actual pore shape and a circle. It assumes the values of 1 for a circle and 0 in case of a line. An analysis of the residual porosity from the sintering experiments of TNB-V5 (Table 12) indicates that the higher the sintering temperature applied, the larger the shape factor for the same value of cumulative frequency, as shown in Figure 55. Therefore, despite the similar values of porosity of specimens sintered at 1490 °C and 1510 °C, the pore shape was actually different.

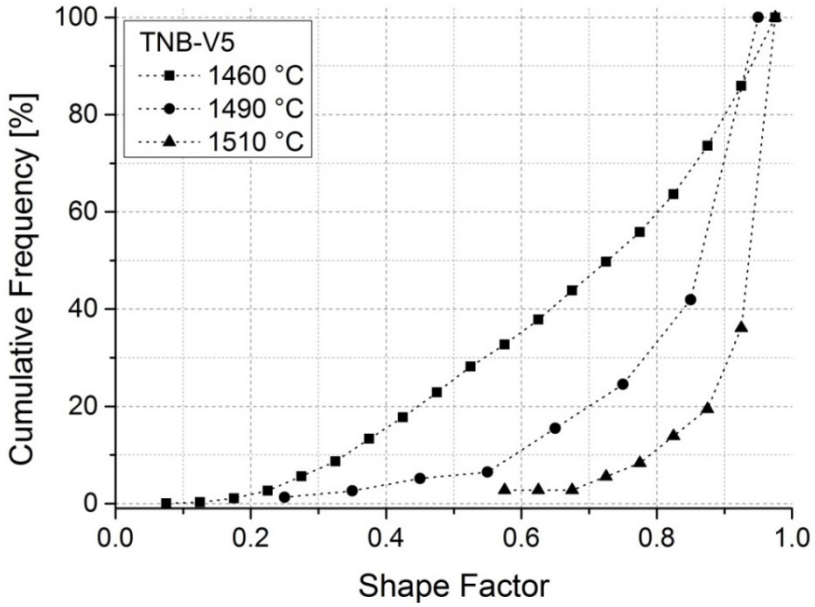

Figure 55 – Shape factor of porosity of TNB-V5 sintered at different temperatures for 2 hours.

In case of TNB-V5 (Figure 27), the final sintering temperature was slightly above the onset of the melting peak (solidus line). It is quite possible that small amounts of liquid phase were present. Consequently, the phase transformations during cooling from the sintering temperature (in equilibrium) would probably be:

$$L + \beta \rightarrow \beta \rightarrow \alpha + \beta \rightarrow \alpha \rightarrow \alpha + \gamma \rightarrow \alpha_2 + \gamma$$

This series of phase transformations is most probably in principle also true for the majority of alloys investigated in this work considering that the main elements added were β stabilising elements, which should basically enlarge the β phase field. In the case of higher amounts of β stabilising elements, the phase formation during cooling could be slightly modified to include the formation of retained β phase (β_r):

$$L + \beta \rightarrow \beta \rightarrow \alpha + \beta \rightarrow \alpha + \beta_r \rightarrow \alpha + \gamma + \beta_r \rightarrow \alpha_2 + \gamma + \beta_r$$

As the sintered part was cooled down after the isotherm, it crossed the single β phase field followed by the α + β and later the single α phase field. At this point the solid state transformation β → α is the same as in the case of pure titanium [56]. The material underwent a transformation from the bcc β to the disordered hcp α, which is characterised by the Burgers orientation relationship [56,60]. The β solidification has been proven to be an

efficient method for microstructure refinement in the case of cast titanium aluminides [66,179,180] leading also to more homogeneous microstructures than the peritectic solidification. Cooling from the β phase field after sintering is believed to have the same effect: nucleation of more α grains from the same parent β with a larger number of possible orientation variants of the α phase, as well. Additionally, borides (present in all alloys studied) can serve as heterogeneous nucleation sites for the α phase [113,190] contributing to further microstructural refinement. Another important phenomenon that takes place at these temperatures is the formation of Nb microsegregations (also including other β stabilising elements, when present), which appear as a network with bright contrast in BSE pictures, for example in Figure 29. These regions arise due to the β → α phase transition, when the β stabilising elements are rejected to the β phase and remain at the former α/β phase boundaries [64]. In the case of alloys containing stronger β stabilising elements, which increase the overall effective contents of β stabilisers, such as 3Nb-1Mo and its variants, the β phase was retained at room temperature, remaining mostly at the colony boundaries and triple points.

Noteworthy to mention is that coarsening of the microstructure is fastest and therefore most critical in the single α phase field. Additionally, the size of α grains determines the final size of the lamellar α_2 + γ colonies, showing the importance of the cooling rate while in this range of temperatures. In fact, TNB-V5 sintered with the same parameters and cooled down from the sintering temperature at three different rates of 100, 50 and 10 °C/min showed colony sizes in the order of 80, 95 and 185 μm, respectively [178].

The final sintered microstructures of the titanium aluminides alloys in the compositional ranges studied here were always fully lamellar. This happened because the sintering temperatures were always in the range of the β + L phase field, consequently inevitably passing through the α phase field while cooling. Moreover the cooling rates possible with the sinter furnace used for the experiments were in the order of 100 °C/min or lower (from sintering temperature down to 1000 °C). At the mentioned cooling rate, the lamellar structure forms as the α + γ phase field is crossed, which happens progressively with the γ precipitating from the α phase [10]. Further cooling leads to the ordering of the hexagonal α phase changing it to the α_2 phase [69]. The final sintered microstructure of TNB-V5 was composed of fully lamellar colonies of alternating α_2 and γ platelets, microsegregations of Nb, boride particles and residual porosity, as shown in Figure 29. The major microstructural differences between TNB-V5 and the different alloy variations tested were the presence of

retained β phase and of precipitates (Figure 46), which were also formed upon heating and/or cooling from the sintering temperature. Consequently, alloys such as 3Nb-1Mo-1Si showed the same fully lamellar microstructure as TNB-V5 with boride particles and pores, however with the additional presence of Ti_5Si_3 precipitates and retained β phase (instead of the Nb microsegregations).

It is noticeable when comparing Figure 21 and Figure 46 (a) and (b) that the microstructure originating from fast cooling of molten TNB-V5 is fairly similar to the sintered version at the microscale. This would be expected since the same solid state transformations took place. The arc melted microstructure is however finer because the single α phase field was crossed at much higher cooling rates. At the macroscale, specimens prepared by arc melting contained macrosegregations due to the dendritic solidification during the arc melting process, Figure 21 (a).

7.1.2 The effect of different master alloys as starting materials

The specimen preparation throughout this research work was conducted using two different approaches in regard to the starting materials. Initially using pre-alloyed powder with fairly large additions of elemental powders and later, once the most prominent alloy candidates had been selected, using pre-alloyed powder with only minor additions of elemental powder. The pre-alloyed + elemental powder approach was also tested with different master alloys: firstly TNB-V5 (Screening Part I) and later Ti-48Al-5Nb-0.2B-0.2C and Ti-48Al-3Nb-0.2B-0.2C (Screening Part II). The starting materials showed a considerable influence in the sintering behaviour and microstructure formation, especially in regard to residual porosity and homogeneity. The measured bulk compression creep results might however be considered as representative for the different compositions tested, given some considerations.

As displayed in Figure 28, the addition of elemental powders to TNB-V5 had a severe impact on the residual porosity. In some cases, even sintering at higher temperatures (low β series) or for longer times (high β series) could not significantly improve the densifications to the same level as the reference pre-alloyed material (porosities <1%). The only exceptions were the specimens that melted slightly in contact with the sintering substrate (3Nb-0.5Gd, 3Nb-0.2Gd and 1Si) and 1Cr. The former were less porous due to extensive formation of liquid during sintering, and the latter probably was due to the smaller difference in atomic number between Cr and Ti, which could have facilitated its incorporation into the matrix. A similar effect

could also be seen with Mn additions, as in Figure 19. However, combinations of Cr and Nb as in 8Nb-1Cr significantly increased the residual porosity.

The specimens 3Nb-1Mo, 3Nb-2Ta and 3Nb-0.7W from the low β series showed the largest residual porosity of all alloys. They also required the largest amounts of elemental aluminium addition for the adjustment of the composition. In fact, for the same amount of feedstock prepared (20 g), the amount of elemental aluminium required increased by a factor of 6 in the case of 3Nb-1Mo when compared to TNB-V5+Al (Ti-47Al-5Nb-0.2B-0.2C). As discussed in Chapter 4, additions of elemental aluminium caused a shift in the optimum sintering temperature. Yet, in the case of the specimens mentioned above, the reduced sinterability was much stronger than with small additions of elemental aluminium to TNB-V5. This phenomenon was caused by a combination of the following effects:

- an intermediate intermetallic layer formed in the early stages of sintering at the surface of the pre-alloyed powders due to elemental aluminium addition;
- non-optimised sintering parameters; and
- the presence of heavy diffusing elements such as Ta, W, Nb and Mo in elemental form.

In order to minimise the amounts of elemental powders added and to completely eliminate the necessity to add elemental aluminium, the master alloys Ti-48Al-5Nb-0.2B-0.2C and Ti-48Al-3Nb-0.2B-0.2C were designed. Two different Nb contents were necessary due to the high β and low β concepts. In general, the porosity levels were smaller in comparison to using TNB-V5 as master alloy, Figure 38. The sintering temperatures were also optimised based on the DSC measurements of the melting peaks. Consequently by switching the master alloy, two factors were improved that played a significant role when TNB-V5 was used as master alloy: the amounts of elemental additions and the sintering parameters.

In case of 3Nb-1Mo, it is possible to clearly separate the effect of decreasing elemental additions in the residual porosity. The same composition was prepared using TNB-V5 and Ti-48Al-3Nb-0.2B-0.2C as master alloys, which required large and small elemental powder additions, respectively. Both specimens were sintered with the same parameters at 1510 °C for 2 hours. The final residual porosity decreased from 5% to nearly 1% indicating the

pronounced influence of the elemental powder additions on the densification and indirectly the effect of the starting master alloy.

A further step into optimisation of residual porosity was made by switching the master alloy to a new system based on 3Nb-1Mo, namely Ti-44.5Al-3Nb-1Mo-0.2B-0.2C, thus eliminating the large addition of heavy elements (Mo) in the form of elemental powders. Figure 45 shows that the porosity of all alloy variations prepared with Ti-44.5Al-3Nb-1Mo-0.2B-0.2C were in the same range as pre-alloyed TNB-V5. Additions of Si and Gd were still in the form of elemental powder or a compound powder of $GdSi_2$; nonetheless their influence in porosity is negligible based on Figure 38 and Figure 45.

The microstructure homogeneity was a severe issue when TNB-V5 was employed as master alloy. As discussed in Chapter 4, addition of elemental Mn to TNB-V5 was successfully conducted with the proper sintering parameters. Nonetheless, after adding other elements than Mn the microstructural inhomogeneity seen in Figure 30 and Figure 32 was much more pronounced than expected from the preliminary trials during the feasibility study. Even when decreasing the gross amounts of elemental powder additions by preparing specimens with Ti-48Al-5Nb-0.2B-0.2C and Ti-48Al-3Nb-0.2B-0.2C, the microstructure homogeneity could not be improved, as depicted in Figure 39, Figure 40 and Figure 41.

The unambiguous cause for the microstructural inhomogeneities was the addition of heavy elements such as W, Ta, Mo, Nb in the form of elemental powders. All these elements are slow diffusers and consequently need plenty of time at high temperatures in order to be homogenised. Specimens containing Mo and Nb as added elemental powders became more homogeneous after increasing the sintering time from 2 to 4 hours, but in case of the heaviest elements W and Ta, no qualitative difference could be found after 4 hours of sintering. Completely homogeneous sintered microstructures were only possible by preparing Mo-containing specimens with pre-alloyed powder (Ti-44.5Al-3Nb-1Mo-0.2B-0.2C), supporting the fact that the microstructure homogeneities were really caused by the addition of heavy elements. The effect is quite evident comparing the microstructures of 3Nb-1Mo from Figure 39 and Figure 46.

7.1.3 The influence of composition on sintering behaviour

It is clear from Table 15 and Table 18 that the sintering behaviour and especially the sintering temperatures show a strong dependency on the composition. Independent of the method by which the alloying elements were introduced, their intrinsic effect was always the same. Whether the alloying elements were elemental powders or if they were already present in the pre-alloyed powder, a change in the optimum sintering temperature in all compositions could be observed. The optimum sintering temperature is highly dependent on the absolute melting point of the alloy [188]; however, the difference between the onset of the melting peaks and the optimum sintering temperature is larger in the case of pre-alloyed + elemental powders (Table 15) than in the case of pre-alloyed powder (Table 18).

The alloy 3Nb-1Mo was prepared by different methods and sintered with the same parameters (1510 °C – 2 hours) achieving porosities smaller than 1%. 3Nb-1Mo prepared with Ti-48Al-3Nb-0.2B-0.2C as master alloy showed an onset of the melting peak at 1492 °C, while made from pre-alloyed powder the onset was at 1502 °C. This difference was most probably caused by the presence of elemental Mo in the former case. Elemental Mo has a rather high melting point; therefore it is quite feasible that as the powder mixture was heated, Mo powder was not completely and homogeneously dissolved in the alloy matrix. Since the melting point of the master alloy (Ti-48Al-3Nb-0.2B-0.2C) was lower than that of the target alloy composition (3Nb-1Mo), the onset of the melting peak was shifted to lower temperatures. The required sintering temperature for achieving adequate porosity levels was nonetheless the same (1510 °C). In case of the Si-containing specimen, a similar effect was observed. However, since Si has a lower melting point than the master alloy, the onset of the melting peak was shifted to even lower values than in the case of only Mo addition. The difference between the onset of the melting peak and the optimum sintering temperature is narrowed as the amount of elemental powders added is decreased.

The most severe practical consequence of using the pre-alloyed + elemental powders approach corresponds to the control of the liquid phase fraction present at the sintering temperature. The dimensional stability might be compromised even by a small variation of temperature in this range. Despite the fact that specimens with low residual porosities can be prepared by both approaches, using pre-alloyed powder seems far more advantageous especially considering microstructural homogeneity.

7.1.4 Considerations about the oxygen, nitrogen and carbon levels after sintering

The pick-up of impurities is inevitable in any powder metallurgy processing technique [191]. Before the finished consolidated part is achieved, several steps involving powder handling are necessary, which usually contribute to increased levels of oxygen, carbon and nitrogen, in addition to the impurities already present in the starting powders. The MIM process contains a further source of impurities due to the presence of organic binders and thus the required debinding processes. As in the case of α + β titanium alloys [192], impurities play an important role in the final mechanical properties of titanium aluminides [117]; therefore carefully conducting all steps during processing in order to minimise contamination is essential to ensure impurity levels within tolerable ranges. If the solubility limit of interstitial elements is exceeded, precipitation of oxides, carbides and nitrides takes place [52,115,117,158,163].

Table 13, Table 16 and Table 19 show the oxygen values obtained by different specimens that were prepared in various sintering runs. The oxygen levels achieved were roughly around 1500-2500 µg/g, which corresponds to a considerable increase in comparison to the starting values (Table 3). The only exceptions were the specimens prepared with pure Gd addition, indicating that the Gd powder was a strong source of oxygen. This is supported by the fact that specimens prepared with $GdSi_2$ showed levels in the order of 2000 µg/g.

The strong scatter in the oxygen contents resulted in great part due to variations in the sinter furnace. Small differences in the cleanliness of the atmosphere might happen from batch to batch, which could cause the impurity levels to change even with the same sintering parameters. Additionally, specimens prepared by Uniaxial Pressing showed a much larger scatter in oxygen values than the ones produced by MIM. Shaping by uniaxially pressing of feedstock (including heating, pressing and cooling of the feedstock) takes considerably longer than MIM. Therefore it is understandable that larger variations in the oxygen content of specimens prepared by UP could arise.

Oxygen has a relatively high solubility in the α_2 phase, which is believed to be > 2.1 at.% (~9000 µg/g), while the γ phase only dissolves about 250 at. ppm (100 µg/g) [193–196]. It is well known that once the solubility limit of the γ phase is exceeded, the excess oxygen is taken by the α_2 phase, as suggested by Menand et al. [193]. Even though the phase fraction of α_2 is normally smaller than γ, if the solubility of both phases is averaged considering a fraction of 30% α_2 and 70% γ, the mean value calculated is roughly 1400 µg/g of oxygen

solubility. The precipitation of oxides should take place as soon as both phases get saturated; therefore considering the average oxygen levels in the specimens investigated, it is likely that oxides were present in the microstructure. Kawabata et al. [117] systematically studied the effect of oxygen addition in single phase binary titanium aluminides and found that excess of oxygen precipitated in the form of α-Al_2O_3. The presence of alumina could not be confirmed by XRD in the as-sintered MIM specimens (Figure 53), indicating that if oxides were present, their volume fraction was small.

Nitrogen and carbon partition preferentially into the α_2 phase [193]. The solubility of these elements is however different than oxygen. Kawabata et al. [158] reported overall solubilities of nitrogen and carbon to be lower than 0.1 at.% (~400 µg/g) in binary Ti-(48-52)Al because carbides and nitrides were always found in the microstructure within the range studied (0.1-1 at.% C and 0.1-4 at.% N). Karadge et al. [160] also found carbides with 0.1 at.% C in a quaternary alloy K5SC (Ti-46Al-2Cr-3Nb-0.2W-0.2Si-0.1C), while Gabrisch et al. [162] studied different additions of carbon (0-1 at.%) in Ti-45Al-5Nb prepared by HIP and estimated the carbon solubility to be not higher than 0.5%. Below this value the strengthening effect was attributed to solid solution hardening. Nonetheless small P carbides could be found by TEM and were detected by HEXRD. Pietzka et al. [197] also reported that the solubility of carbon in the two-phase titanium aluminides should be < 0.6 at.%. Additionally, the solubility of nitrogen was reported to be < 0.5 at.% [163,198].

The nitrogen values obtained with the alloy variations studied are shown in Table 13, Table 16 and Table 19. In comparison to the initial values (Table 3), the nitrogen pick-up was considerably small and most of the specimens contained nitrogen levels below 300 µg/g. Given the solubility range of nitrogen, it is quite feasible that nitrogen was in solid solution mostly in the α_2 phase. On the other hand, the presence of carbides is highly probable, considering that carbon was already present in the starting powder at the concentration of 0.2 at.% and that its content was even further increased after sintering. Carbides and nitrides precipitate either as the perovskite P phase (Ti_3AlX) or hexagonal H phase (Ti_2AlX), X=C or N [159,163]. According to Kawabata et al. [158] they precipitate on line faults such as dislocations and planar faults (grain boundaries, phase boundaries, twin boundaries and stacking faults). These precipitates were reported to increase yield and fracture stresses [115,158], as well as creep resistance [52,53,115,118,199].

The effects of impurities (C, N, O) on the mechanical properties as well as their solubility limits and precipitation mechanisms are beyond the scope of this work. However, since the presence of C, N and O usually involves an increase in the creep resistance due to solid solution hardening and precipitation strengthening, it is reasonable to assume that their effect in the alloys studied was in principle not detrimental. Yet, the ductility of the materials might be deteriorated by high amounts of these impurities. There are still other aspects to the presence of these impurities such as the phase equilibria at high temperature since C, N and O are α stabilisers. Nonetheless considering that the majority of the alloys tested contained strong β stabilisers, it is quite possible that their effect was insignificant.

7.1.5 Validation of compression creep measurements as screening parameter

Despite the variations in porosity and microstructural homogeneity of specimens from Screening Part I and II, the compression creep measurements can still be considered representative for each of the compositions tested.

Firstly, the porosity levels were below or in the order of 5%, (except 3Nb-0.7W that exhibited 6.7%), which usually characterises a threshold value for open porosity, and therefore more severe degradation of the mechanical properties. For example, 3Nb-1Mo and 3Nb-2Ta showed significantly different times to reach 1% plastic deformation, 11 and 3 hours respectively, under the same compression creep conditions, as displayed in Figure 35. These alloys contained qualitatively the same degree of microstructural inhomogeneity (Figure 30) and also the same porosity levels, 5% in case of 3Nb-1Mo and 4.5%, 3Nb-2Ta (Figure 28). Consequently, it is reasonable to assume that the compression creep results are mainly determined by the differences in alloy composition, despite the microstructural inhomogeneities and the relatively high porosity.

Secondly, the compression creep measurements conducted with the specimen 3Nb-1Mo in different microstructural conditions and porosity levels led to reasonably comparable outcomes (Table 23), given the scatter in the measurements. Obviously, the more significant differences in porosities (for example 3Nb-0.7W, 6.7% and 1Si, 0.5%), in addition to the microstructure inhomogeneities, might have played a role in the measured primary creep resistance and also contributed to scatter in the data.

Table 23 – Comparison of 3Nb-1Mo alloy prepared with different master alloys. The compression creep measurement was carried out at 800 °C and 350 MPa.

Microstructural Condition	Master alloy	Sintering parameters	Porosity (%)	Time to 1% strain (hours)
Inhomogeneous	TNB-V5	1510 °C-2h	5 ± 1	11
Inhomogeneous	Ti-48Al-3Nb-0.2B-0.2C	1510 °C-2h	0.8 ± 0.4	15
Homogeneous	Pre-alloyed 3Nb-1Mo	1510 °C-2h	0.1 ± 0.04	10

In summary, considering that only the alloy 3Nb-0.7W could not be sintered with porosity lower than 5% (threshold value), it is reasonable to conclude that this specimen was the most affected by the deterioration of the mechanical properties due to porosity, while the remainig specimens should lead to representative creep results. Therefore, the differences in performance of the remaining specimens used for screening of alloying elements can be plausibly taken as mostly compositional dependent.

7.2 Mechanical properties

7.2.1 Hardness

Hardness measurements are a quick and easy method for a rough estimate of the mechanical properties at room temperature. In the case of sintered parts, ideally the porosity should be closed (<5%) and the measurements conducted on a pore free area. However, as in most cases, it is likely that pores were lying below or in the vicinities of the measured surface. Depending on their size, a change on the indent and consequently in the hardness value might have taken place. Figure 56 shows two different cases of porosity related to hardness measurements.

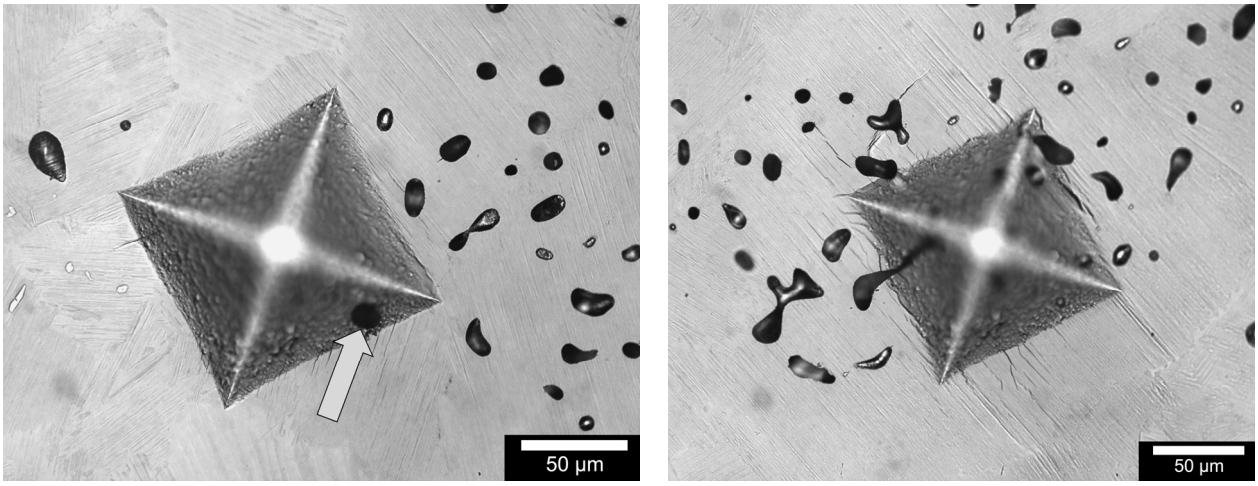

(a) (b)

Figure 56 – Different Vickers indents measured on the alloy 1Cr. Indent containing one pore indicated by an arrow. (b) Indent containing several pores in the indentation area.

In Figure 56 (a), even though the pores were quite near the indent, its shape remained fairly unaffected. The indent also hit a small pore indicated by the arrow. On the other hand, in Figure 56 (b) the shape of the indent was deformed and the lamellae cracked in the vicinity of the indentation leading to an overall lower hardness value (larger indentation). Therefore, two different cases of Vickers hardness measurement influenced by porosity can be distinguished:

- Figure 56 (a) in which a measurement of a compound (pore-matrix) was actually conducted. This probably leads to lower values and higher scatter than a fully dense material but it corresponds to a reasonable estimate of a pore-containing material's strength;
- Figure 56 (b) in which the hardness value was significantly affected by the pores leading to high scatter or even invalidating the measurement. In such a case, a new measurement was carried out in another region of the specimen.

Consequently, the influence of porosity in hardness measurements in principle increases the standard deviation and possibly reduces the overall hardness. Regardless of the uncertainties inherent to the method, results of hardness are often used in aging studies [200,154,47] or in experiments involving the addition of new alloying elements [131,201], where significant changes in the mechanical properties are expected.

In case of the reference material TNB-V5, it is possible to see from Figure 24 and Figure 34 that the hardness value of the specimen prepared by arc melting is higher than the powder

metallurgy one. This is most certainly due to the difference in lamellar spacing originated from the faster cooling rates of the arc melted specimen and the residual porosity of the powder metallurgy specimen. A similar behaviour was also shown by the compositions 1.5Mo and 8Nb. The indenter load used for the measurements shown in Figure 24 and Figure 34 was different but as described by the ASTM E384-06, "…the Vickers hardness number (HV) is obtained by dividing the force applied to a Vickers indenter by the surface area of the permanent impression made by the indenter." [202], the values obtained with different forces should be similar. A comparison made between the HV numbers of the specimen with aluminium variations in the feasibility study (Chapter 4) Figure 12 and Screening Part I Figure 34 supports that fact.

Based on the hardness of the low β series, Figure 34, the values achieved with precipitation strengthening are in average higher than the reference material, while with addition of heavy elements (solid solution hardening) were similar to TNB-V5. Actually, it would be expected that all additions would cause an increase in hardness. The slightly lower values of 3Nb-0.7W, 3Nb-2Ta and 3Nb-1Mo probably resulted from the increased porosity that inevitably plays a role in hardness measurements.

Specimens from the high β series in Figure 36, which were similar to the low β series with regard to microstructure homogeneity but contained less porosity, showed in general higher hardness values than TNB-V5. As the porosity was improved in Screening Part II and in the Final Alloy Candidates, so was the hardness. This supports the fact that the porosity had a considerable influence in the hardness values.

7.2.2 Tensile

The room temperature tensile properties of two-phase titanium aluminides alloys are greatly dependent on the composition and microstructure [71,203]. Kim et al. [73] also describes this relationship as a function of the morphology of the α_2 phase including volume fraction, distribution and thickness. Usually duplex microstructures provide the highest ductility and strength, while fully lamellar are more brittle and generally show lower strength. However, fully lamellar microstructures are the most creep resistant [71,204,205] and since the microstructures obtained with near solidus sintering of the engineering titanium aluminide alloys are always fully lamellar, the behaviour of this type of microstructure is of greatest interest for MIM-TiAl.

Tensile properties measured at room temperature with the Final Alloy Candidates are displayed in Table 20. TNB-V5 showed similar UTS as 3Nb-1Mo but was slightly more ductile. In contrast, 3Nb-1Mo-1Si displayed higher UTS but lower ductility. Kim et al. [206] showed that there is a direct relationship between colony sizes, tensile strength and ductility. The Hall-Petch relationship was also demonstrated valid for a wide variety of titanium aluminides [207–211]. As the colonies get smaller, the more difficult it is for the dislocations to move [212]. Nonetheless, the Hall-Petch relationship is questionable in the case of a fully lamellar microstructures because the lamellar spacing also plays an important role [10]. Consequently, the higher UTS of 3Nb-1Mo-1Si can only partly be explained by the finer colony size (Figure 47). The greatest contribution to the improved tensile properties is probably from the Si precipitates.

As reported by Kim et al. [74,206], fully lamellar microstructures exhibit an inhomogeneous deformation behaviour. Upon loading soft oriented colonies deform whereas a neighbouring colony might not, which leads to microcrack formation and non-uniform deformation. The ductility is consequently dependent on the general yielding before the formation of cracks of critical size that lead to cleavage fracture. Since a fully lamellar microstructure with no texture shows a random distribution of soft and hard oriented grains, the formation of critical sized cracks is prevented by a smaller colony size. Consequently smaller colonies also lead to more plastic deformation at room temperature. The specimen 3Nb-1Mo-1Si showed nonetheless lower plastic elongation than TNB-V5 and 3Nb-1Mo. Additionally, in the case of 3Nb-1Mo-1Si-0.2Gd, no plastic strain at all could be measured. That appears to be an effect of the precipitates. Fracture in titanium aluminides at room temperature proceeds by general yielding and it is controlled by the crack nucleation process [213]. With the presence of precipitates, local stress concentration can occur which leads to early crack formation. Lower ductilities result as a direct consequence. For the alloy 3Nb-1Mo-1Si-0.2Gd, an additional factor for low plasticity was the presence of large pores >100 μm. This type of porosity was normally irregular and similar to the precipitates could facilitate stress concentration and cracking.

In comparison to duplex microstructures of extruded high Nb containing titanium aluminides that can achieve UTS >1000 MPa and yet considerable ductilities of 1 to 2% [52,53], the room temperature tensile properties of MIM-TiAl alloys are rather unsatisfactory. Nonetheless when compared to the cast + HIP conditions of similar compositions the mechanical properties are within the same range. For instance, Ti-46Al-8Nb was reported to

show UTS of 482 MPa and 0.2% elongation [13], the same alloy with a refined microstructure due to boron addition Ti-46Al-8Nb-1B showed 620 MPa and 0.8% [214]. The more traditional GE alloy (Ti-48Al-2Nb-2Cr) is able to reach 465 MPa and 2.4% elongation [215]. Obviously the impurity levels and the microstructures of cast + HIP materials are different to materials processed by MIM, however considering that MIM is a near net-shape process, the as-sintered tensile properties are quite acceptable.

Thermomechanical processing of titanium aluminides allows the preparation of a variety of microstructures and thus properties [70,216,217]. MIM is considerably limited in regard to microstructural variations, considering that sintering normally requires temperatures above the α transus temperature and that no recrystallisation is possible due to the lack of induced plastic deformation. However, considering that titanium aluminides are primarily focused on high temperature applications, the fully lamellar microstructure of the MIM process is not detrimental. The low ductility seems to be the major disadvantage, which is characteristic of this type of microstructure. It is possible that with improved process control during MIM, the impurities levels could be lowered and consequently the ductility enhanced.

7.3 Creep behaviour

7.3.1 The influence of loading mode in creep measurements: tensile vs. compression

The different creep response in tension and compression has been reported for many different materials [218–223]. In general, the creep resistance measured in compression is higher than in tension and this difference tends to be larger the higher the stress [218]. The crystalline lattice is compressed when the material is subjected to compressive forces increasing the resistance to diffusion, while under tension it is expanded, which facilitates diffusion-assisted dislocation climb [10]. Additionally, tensile creep loading also causes early formation of cracks in the tertiary stage, therefore leading to lower creep life.

In the case of the Final Alloy Candidates, there was a clear difference in compression and tensile creep at 800°C – 350 MPa. Not only was the creep deformation lower in compression, but also the minimum creep rate, as shown in Figure 57. Despite the differences between both loading modes, the trend of creep resistance was similar. The only exception was the Gd-containing specimen. Xia et al. [122] reported a similar result while comparing compression and tensile creep behaviour of Ti-44Al-1Mn-2.5Nb-0.15Gd and Ti-44Al-1Mn-2.5Nb. In this

study the authors also observed an improvement in creep resistance due to Gd addition but it was only visible in the tensile measurement.

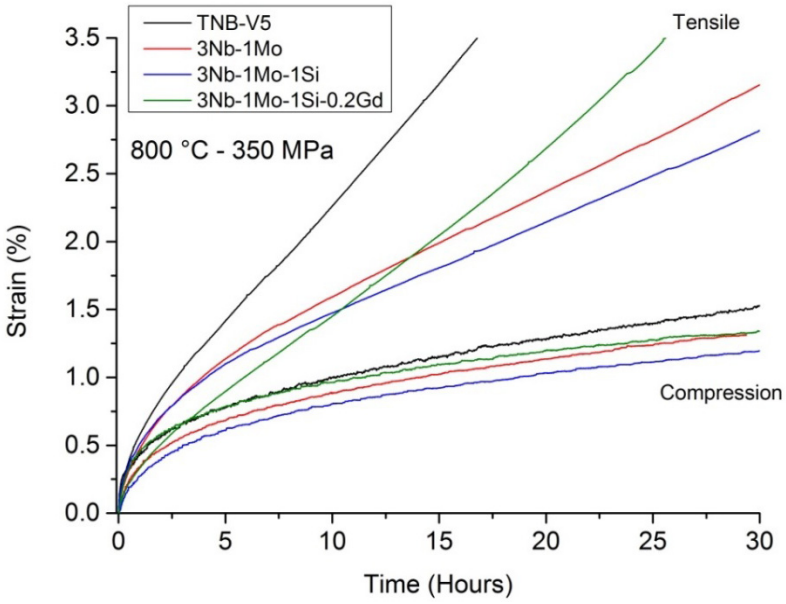

Figure 57 – Comparison of tensile and compression creep at 800 °C – 350 MPa.

It has been reported that the main factor contributing to the difference in creep behaviour measured in compression and tension in titanium aluminides was related to microstructural changes during testing [122,170]. The authors explained that the lower secondary creep rates and overall superior creep resistance in compression was due to the stability of the α_2 phase. As reported by Wang et al. [224], the α_2 lamella become unstable under tensile load, which could not be observed at the same temperature without the application of stress. Consequently, since in compression the dissolution of the α_2 lamellae is less frequent, the actual measured creep resistance is higher in compression. Based on the phase fraction change measured after creep testing (Table 21 and Table 22), the same mechanism most probably occurs in case of the Final Alloy Candidates. Furthermore, the inverse behaviour in the case of the Gd-containing specimen can be explained assuming a dynamic precipitation of Gd-containing particles with the dissolution of the α_2 phase. Since the dissolution of the α_2 phase is slower in compression, less strengthening particles would be present and thus the lower creep resistance in compression results.

Even though a great difference in creep resistance could be observed in compressive and tensile creep, a similar qualitative result was achieved with the Final Alloy Candidates. The

differences were however smaller in the primary creep region and increased only in secondary creep. Consequently, it is possible to conclude that compression creep measurements are in fact a valid parameter for the investigation of the primary creep resistance. Moreover, considering the simplicity of the compression creep test and the time required to prepare the specimens, compression creep was a powerful tool for the rough assessment of the primary creep behaviour.

7.3.2 Primary creep of TNB-V5 and the different influencing factors

The primary creep resistance of TNB-V5 prepared by arc melting is displayed in Figure 25, while TNB-V5 prepared by uniaxially pressing of feedstock in Figure 44. The time to reach 1% plastic deformation at 800 °C and 350 MPa is quite similar with around 7 hours. Both compression measurements are however above the value obtained in tensile creep (approximately 3 hours) conducted with a MIM specimen, Figure 50. Considering the inherent scatter of the measurements and the influence of loading mode (compression vs. tension), the primary creep resistance of TNB-V5 was fairly independent of the preparation method. Nonetheless there are different opposing factors playing a role in the primary creep resistance, which led to this outcome. They will be discussed in the following.

A direct comparison of specimens might not be very straightforward due to the different microstructures achieved with arc melting and powder metallurgy. It is noteworthy that arc melted specimens contained microstructural inhomogeneities due to the dendrites formed during solidification, typical of cast microstructures. Moreover, there is a drastic difference in the impurity levels, particularly in the oxygen and carbon content of specimens processed by powder metallurgy, which is significantly higher. Even though the primary creep resistance (evaluated as the time to reach 1% plastic deformation) was remarkably comparable, the overall primary creep behaviour was different, yet this difference could only be seen in tensile creep measurements.

7.3.2.1 Microstructure

The microstructure has a strong influence on creep resistance, with the fully lamellar showing superior results than the duplex form of the same composition [73,225]. Independent of the preparation method, all microstructures investigated in this work were fully lamellar and

therefore of the theoretical most creep resistant type. However, the specimens prepared by arc melting were cooled down faster than specimens prepared by powder metallurgy. The effect of the cooling rates has already been identified as a critical controlling factor for the colony size and lamellar spacing [226,227]. Both factors can influence the primary creep resistance.

Fine colony sizes in fully lamellar microstructures have been shown to increase the minimum creep rate with the same lamellar spacing, but this effect was only present for sizes below 100 μm [72]. Considering that arc melting led to colony sizes in the order of 30 μm and powder metallurgy to about 80 μm, the primary creep resistance should in fact be lower. On the other hand, the lamellar spacing of the arc melted specimens was most probably finer than UP and MIM. Although it was not measured in the framework of this research, the lamellar spacing can be plausibly assumed to be small due to the fast cooling rates applied in the case of arc melting. In contrast, specimens prepared by UP and MIM are assumed to have similar lamellar spacing but larger than arc melted. As reported by Maruyama et al. [72], at high stresses fine lamellar spacing significantly reduced the minimum creep rate in binary titanium aluminides, increasing the creep resistance. The negative effect of the small colony size of the arc melted specimens was probably counterbalanced by the fine lamellar spacing.

The effect of microstructure inhomogeneities on the primary creep properties of cast titanium aluminides was studied by Malaplate et al. [49]. The authors reported that the primary creep stage was enlarged due to the presence of cast defects. These soft areas (defects) were firstly hardened upon loading, which resulted in the build-up of internal stress. As a direct result, a homogenisation of the strength (over the inhomogeneous microstructure) took place during the primary creep stage, which resulted in a longer primary creep regime but lower minimum creep rates than the powder metallurgy counterpart.

In the case of the arc melted specimen presented in this work, the effect observed by Malaplate et al. [49] could not be noticed at all. In fact, the UP specimen showed a longer primary creep regime and also accumulated more strain with a similar minimum creep rate as the arc melted specimen, as displayed in Table 24. It is possible that this effect is not so pronounced in compression considering that the results of Malaplate et al. [49] were measured in tension. If a comparison in tensile creep is made between MIM and cast TNB-V5, the effect of microstructural inhomogeneities is evident and a similar conclusion as Malaplate et al. [49] can be drawn: the primary creep regime is much longer in the case of the cast condition but the minimum creep rate is lower than MIM.

Ideally, from the application point of view, a short primary creep regime is highly desirable considering that the strain rate is high in this region. If both cast and MIM materials would exhibit similar secondary creep rates, a shorter primary creep would result in overall longer times to reach the same amount of plastic deformation. Therefore homogeneous microstructures of the MIM process offer better performance in case of primary creep resistance because the primary creep regime involves a lower amount of strain and finishes after shorter times.

Table 24 – Comparison of the primary stage and the minimum creep rate of TNB-V5 in different process conditions measured at 800 °C – 350 MPa.

Condition	Time to 1% strain (hours)	Loading mode	Duration of primary creep (hours)	Strain during primary creep (%)	Minium creep rate (10^{-7} 1/s)
Arc melted	7.2	Compression	26	1.4	50
UP	7	Compression	36	1.65	51
MIM	2.7	Tension	2.3	0.9	4.9
As-cast*	1.8	Tension	8.2	2.1	3.1

*** Unpublished research, Paul et al. 2010.**

7.3.2.2 Impurities

The impurity level, as previously pointed out, might lead to the precipitation of oxides, carbides and nitrides depending on the final levels after sintering. Clearly from Table 11, Table 13 and Table 19, the oxygen levels were much higher in the case of powder metallurgy processed materials compared to arc melted specimens. The nitrogen levels were similar but the carbon contents were higher due to the presence of binder during processing. The carbon content was only measured in MIM specimens but it is assumed that the levels in the UP specimens were within the same range. In case of TNB-V5, the carbon pick-up was small but large variations in the pick-up happened in other alloys (carbon values varied from 751 to 1237 μg/g). It is reasonable to assume that in the case of the powder metallurgy specimens, the lamellar phases γ and α_2 could have been saturated with impurities and precipitation of oxides and carbides might have occurred. Their effect on primary creep resistance is however positive as will be discussed in the following.

The presence of carbon in different concentrations has been reported as an effective method to improve primary creep resistance of titanium aluminides [52,116,160,161,228]. Carbides increase the resistance to dislocation motion by solid solution hardening of the lamellar phases and also due to precipitates. A significant increase in primary creep resistance was reported by Karadge et al. [160] in the alloy K5SC (Ti-48.3Al-46.2Al-2Cr-2Nb-0.2W-0.2Si-0.1C). The authors explained that as the α_2 phase dissolved, the new γ/γ interface was reinforced with carbide particles, which took place during aging and also during creep testing. The measured carbon content of the MIM specimens was around 0.25-0.5 at.%, therefore carbides might have been precipitated. However, either due to solid solution hardening, the presence of carbide particles or both, the effect of carbon contributed to improve the primary creep resistance.

The effects of oxygen on the mechanical properties of binary titanium aluminide alloys were investigated by Kawabata et al. [117], while ternary and quaternary alloys containing oxygen were studied by Morris [229], Lamirand et al. [152,230] and Ding et al. [231]. All published works reported that oxygen additions increased tensile strength at room and high temperatures, which was associated with a decrease in ductility. Oxygen is believed to increase the strength properties directly by solid solution hardening and precipitation of oxides and indirectly by changing the volume fraction of the α_2 phase.

In one of the few studies that evaluated the effect of oxygen on primary creep resistance, Perdrix et al. [161] reported only little increase in the time to 1% plastic strain up to 5000 μg/g of oxygen. The authors explained that the primary creep was improved with additions of nitrogen and carbon due to precipitation strengthening, which in the case of oxygen did not take place even with the largest oxygen additions. Since the solubility of C, N and O is highly dependent on the relative fractions of the phases γ and α_2, which in turn is dependent on composition, it is difficult to assess if precipitation of oxides actually happened in the case of powder metallurgy specimens. Nonetheless the presence of oxides, like carbides and nitrides, is not harmful for the primary creep resistance. Therefore the inherent high levels of impurities of the MIM process are not detrimental for the primary creep resistance, yet they limit the ductility at room temperature.

7.3.3 The effect of residual porosity

Powder metallurgy materials with very high porosities are normally not suited for load bearing applications. The residual porosity therefore needs to be low (<5%), if the materials are to be subjected to mechanical stresses. Ideally the porosity should also be homogeneously distributed and round in shape, which usually requires proper consolidation (sintering). In general, porosity decreases the area of the load bearing section and contributes to inhomogeneous distribution of stress that ultimately leads to early failure of the component. The effect of porosity in MIM Ti-6Al-4V has been extensively studied in regard to mechanical properties at room temperature [176,177,232–234]. All authors reported an increase in yield and ultimate tensile strength, as well as ductility with a reduction in porosity. This happens because of the improved actual cross section of material and the decrease of the number of possible crack initiation sites, which normally limits the ductility and might be critical for fatigue properties.

The literature concerning creep behaviour of pore-containing materials is not vast. As a general rule, similarly to the mechanical properties at room temperature, the presence of pores degrades the creep resistance of specimens with otherwise similar microstructural features. Zhang et al. [235] reported that cast porosities in a single crystal nickel based superalloy only affected creep resistance for deformations >10%. The authors suggested that the tertiary creep rupture was induced by the already present cast porosity leading to faster tertiary creep rates and lower creep strains. However, Gutman et al. [236] studied the effect of porosity in creep of a die-cast magnesium alloy and reported that already the minimum creep rate decreased as density increased. Additionally, in the case of Gutman's study [236], not only the amount of porosity was identified to play a role but also the size, shape and distribution of pores. Obviously, rounder and more homogeneously distributed pores led to the highest creep resistance.

A systematic evaluation of the effect of porosity in the primary creep behaviour is not possible with the data set available in this study due to the absence of pore-free specimens with similar microstructures. Nevertheless, a qualitative analysis conducted with the composition 3Nb-1Mo from Screening Part I and II indicates that there is, in fact, an influence of porosity in primary creep resistance.

Table 25 summarises the data of 3Nb-1Mo specimens prepared during Screening Part I and II. Microstructurally the specimens were similar, especially with respect to microstructural

homogeneity. The other main influencing factors on the creep resistance are also displayed for comparison. The specimen from Screening Part II was less porous and showed a longer time to reach 1% plastic strain. It also showed smaller colony size and lower amounts of impurities. But these two factors (colony size and impurity level) changed in a way that should positively affect the creep strength of the specimen from Screening Part I and consequently should not decrease the time to 1% strain. Even if the scatter in the measurements from Screening Part II is accounted for, the lowest recorded time to 1% strain (13 h) was still higher than the time of 11 hours achieved with the specimen from Screening Part I. Consequently, in spite of the differences in other influencing factors, it is possible to conclude that the primary creep resistance was indeed influenced by the residual porosity. Since these measurements were relatively short (<3% plastic deformation) and were conducted in compression, the possibly more severe degrading effect in tertiary creep could not be assessed.

Table 25 – Data of 3Nb-1Mo with similar microstructural inhomogeneities prepared by Uniaxial Pressing and tested at 800 °C – 350 MPa.

Series	Time to 1% strain (hours)	Porosity (%)	Colony Size (µm)	Impurity level (µg/g)	
				Oxygen	Nitrogen
Screening Part I	11	4.3	80	2437	314
Screening Part II	15.5	0.8	65	1620	169

The effect of porosity in the secondary creep regime can be analytically estimated by applying the Equation 1 to a pore-free and a pore-containing condition. Assuming that the pores cause a decrease in the area and therefore in the stress, it is possible to estimate the ratio between the minimum creep rates:

$$\frac{\dot{\varepsilon}_1}{\dot{\varepsilon}_2} = \left(\frac{\sigma_1}{\sigma_2}\right)^n \qquad \textbf{Equation 2}$$

It is also necessary to assume that the temperature and activation energy are constant in both conditions. Equation 2 predicts the secondary creep rate ratio for various stress exponent values, as shown in Figure 58. The variation of the creep rate with porosity is more critical for higher stress exponents and higher porosities.

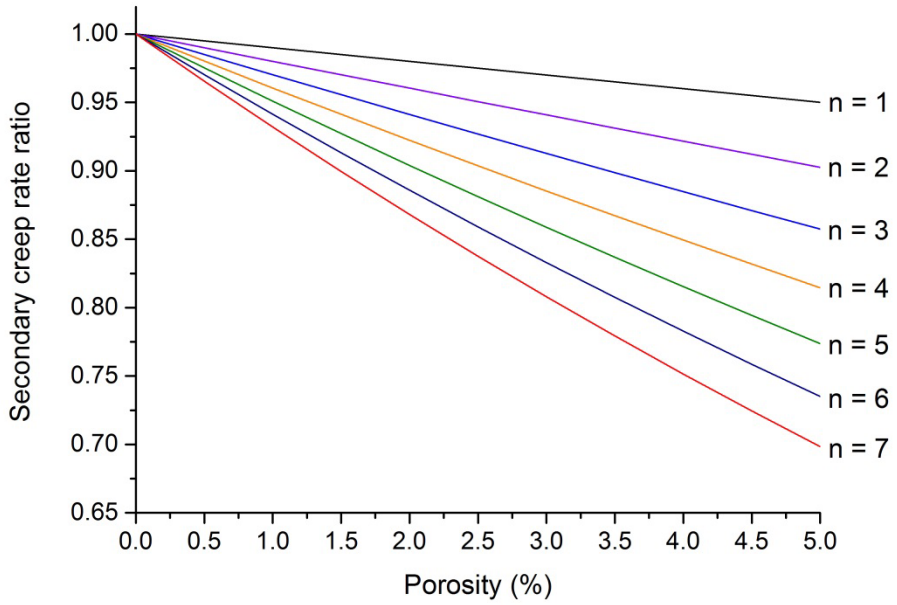

Figure 58 – Secondary creep rate ratio as a function of porosity for different stress exponent values.

The minimum creep rates of the Final Alloy Candidates measured at 800 °C – 350 MPa were used to calculate the pore-free minimum creep rates using Equation 2, as displayed in Table 26. Since the porosities of alloys were fairly low, the decrease in the minimum creep rate due to porosity was very small, as predicted by the previous analysis.

Table 26 – Comparison of creep ratios of different alloys. The minimum creep rate of the pore-free condition was calculated with Equation 2. Values of the minimum creep rate were measured at 800 °C – 350 MPa loading.

Alloy	Porosity (%)	Minimum creep rate (x10^{-7} 1/s)		Creep rate ratio $\left(\frac{\dot{\varepsilon}_1}{\dot{\varepsilon}_2}\right)$
TNB-V5	0.12	4.8		---
	0	n = 1	4.794	0.999
		n = 5	4.771	0.994
		n = 7	4.760	0.992
3Nb-1Mo	0.08	2.1		---
	0	n = 1	2.098	0.999
		n = 5	2.092	0.996
		n = 7	2.088	0.994
3Nb-1Mo-1Si	0.13	1.8		
	0	n = 1	1.798	0.999
		n = 5	1.788	0.994
		n = 7	1.784	0.991
3Nb-1Mo-1Si-0.2Gd	0.7	3.1		---
	0	n = 1	3.078	0.993
		n = 5	2.993	0.965
		n = 7	2.951	0.952

From the above analysed data, it is possible to conclude that the effect of porosity in secondary creep within the range studied (<1%) is very small and only a slight increase in the minimum creep rate took place. Obviously this result is based on the assumption that the pores are only decreasing the load bearing cross section of the specimen.

Additionally, another possible contribution for the decrease in creep resistance with the presence of pores is the local change in stress distribution that is inevitably induced. As in case of cyclic loading, pores with sharp points or edges lead to stress localisation in small areas, thus locally increasing plastic deformation. In a situation where the pores are nearly perfectly round, it is reasonable to assume that the local discontinuity of the microstructure already suffices to change the stress around it, also leading to stress localisation, which in

turn could accelerate creep deformation. Consequently, although the extent of the actual effect of porosity could not be clearly determined in this study, it seems that minimising discontinuities in the microstructure and increasing the load bearing cross section by increasing density might improve the creep resistance.

7.4 Optimisation of primary creep resistance in titanium aluminides fabricated by MIM

Primary creep resistance in fully lamellar microstructures is highly dependent on the characteristics of the lamellae and their interfaces [78,101]. The deformation processes following the first stage of creep are supported by the lamellar structure and its cohesion. Considering the random orientation of colonies (absence of texture) in the case of MIM processed materials, hindering dislocation motion in the lamellae is an efficient strategy to improve primary creep resistance.

In order to increase the strength of the lamellar structure in the context of primary creep, different strategies have been considered. These include refinement of lamellar spacing [43,72,91,93], pre-straining [99], aging [45,112], and alloying with heavy elements [111,237]. The common feature of these methods is the creation of barriers for dislocation motion that are effective at the creep temperature and remain stable for as long as possible. Since MIM processed titanium aluminides require sintering, under normal processing conditions the variation of lamellar spacing is not viable with a regular vacuum furnace. Pre-straining might be difficult depending on the complexity of the part, especially considering that MIM implies near-net shaping. Aging or precipitation strengthening as well as solid solution hardening were therefore promising approaches to be considered.

Throughout this research work, different elements were tested based on the composition of TNB-V5, which is one of the most creep resistant titanium aluminides reported up to this date [53]. The alloying elements evaluated were classified according to their microstructural effect:

- solid solution hardening. This concept was elaborated with the heavy refractory elements W, Ta, Nb and Mo to additionally slow down diffusional processes;
- precipitation strengthening through additions of Si and Gd.

It is important to mention that these elements are in principle not exotic in alloy design of titanium aluminides. However, they were mostly studied in cast or mechanically worked materials and quite often were added due to different purposes than optimisation of primary creep resistance.

7.4.1 Low β and high β series

There were two different main series in regard to the amount of refractory elements added, the low β and high β series that contained, as the names imply, different amounts of the same β stabilising elements (W, Ta, Nb and Mo). The low β series was designed to limit the amount of retained β phase, since it might be detrimental for the creep properties [238–240]. While in the high β series, the presence of larger phase fractions of the retained β phase was accepted in exchange for the potential increase of solid solution hardening and reduced diffusivity. Additionally, in the low β series, the presence of elements that induce precipitation, Gd and Si, were evaluated.

Clearly, comparing Figure 35 and Figure 37 there is a trend that the low β series showed overall better performance than the high β series. As widely discussed in the literature, the presence of β phase is typically considered detrimental for the creep resistance [240,239,130,238]. One reason for this is the enrichment of heavy alloying elements in the β phase causing a depletion of these elements in the γ phase, which in turn decreases the solid solution hardening effect [241,239,238]. Additionally, due to the more open bcc structure of the β phase, diffusion could be accelerated leading to more creep deformation [137,240,242–244].

All alloys from the high β series showed the presence of retained β phase, Figure 32. Comparing the time to 1% strain in Figure 37, only alloys with the heaviest additions (W and Ta) showed improvement in comparison to TNB-V5. Consequently, it is reasonable to state that the presence of retained β phase decreased the primary creep resistance, except when very heavy elements were added. This effect is probably due to the low diffusivity of W and Ta that hindered dislocation climb, which plays an important role in primary creep deformation [10,245,246]. Even though the same effect was expected for additions of Nb and Mo, in this case it is possible to speculate that the depletion of the alloying elements in the lamellar phases was more critical, which resulted in shorter times to 1% strain than TNB-V5. Assuming that Nb and Mo diffuse faster than W and Ta as alloying additions in titanium

aluminides and that despite the formation of β phase some remnant solute atoms were still in solid solution, W and Ta would be more effective in hindering dislocation climb.

All elements (W, Ta, Nb and Mo) in the high β series assumingly increased the resistance to dislocation glide by solid solution hardening and hindered dislocation climb due to their low diffusivity. However, the depletion of the elements to stabilise the β phase in combination to the presence of the β phase itself led to generally lower performance of the high β series in regard to primary creep resistance. The formation of retained β phase assumingly took place out of thermodynamic equilibrium due to the cooling rate applied after sintering (~100 °C/min). Since the β phase field is larger at higher temperatures, it is reasonable that the equilibrium concentrations of the β phase stabilisers was not reached in the α and γ phases.

Based on the results of Screening Part I, only the composition 3Ta from the high β series was selected to proceed to Screening Part II. It was later discarded due to poor performance in comparison to competing alloys. Although promising, the W-containing alloys were also not further investigated due to the necessity of heat treatment (solution and aging) for maximising the creep resistance. Obviously, heat treatments can be incorporated into the sintering cycle but they would require longer times at high temperatures (>20h) [45,139], which might make MIM W-containing alloys industrially less interesting. Furthermore, long times at high temperatures might lead to aluminium sublimation at the surface of MIM parts [37].

Since the strengthening of the lamellar structure, regardless of the method, usually results in lower ductilities, the addition of Cr was included in Screening Part I as a possible ductilising element. The primary creep resistance was however poorer than that of the reference material in both the low and high β series. If otherwise the primary creep resistance with Cr addition had been better, this element would have been further investigated in the screening process for the evaluation of the ductilising effect. Considering a compromise of properties, ductility is secondary in comparison to creep resistance; therefore additions of Cr were not further investigated. Similarly, Mn additions were also tested with the arc melted specimens (Figure 25) but the results of compression creep tests were unsatisfactory, consequently this element was even not included in the Screening Part I.

The low β series provided a wide variety of candidates with improved primary creep resistance in comparison to TNB-V5. The alloy 3Nb-1Mo relying on solid solution hardening showed the longest time to 1% strain. Even though the β phase was present at the lamellar

boundaries and at triple points, a compromise between the presence of β phase and the remnant solute atoms in the lamellar phases was achieved by the composition 3Nb-1Mo. Furthermore, in the low β series, precipitation strengthened alloys containing Si and Gd were also very promising.

7.4.2 Precipitation strengthening

Precipitates increase primary creep resistance because they are effective obstacles for dislocation glide [52]. If the particles are well distributed (placed at the lamellar interfaces, colony boundaries and inside γ grains) and grow to the right size, a significant improvement can be achieved [45,160]. In this research work, additions of Si and Gd were studied with the objective of improving the primary creep resistance through precipitation strengthening. Obviously, since light elements C, N and O that are inevitably present in MIM-TiAl might induce precipitation, they most probably also had a contribution. However, under normal process conditions, these elements occur in the same order of magnitude after sintering (Table 19 shows the values obtained throughout this work for MIM specimens). Consequently, it is plausible to assume that they would affect the test specimens in a similar degree. This is also valid in regard to their effect in solid solution hardening. Therefore, even though the precipitation strengthening effect had two contributors, the effects of Si and Gd could be assessed assuming that the contribution of the light elements is qualitatively similar among the specimens.

To some extent, Si additions to titanium aluminides are controversial. The great majority of studies indicate improved creep resistance through precipitation strengthening by the ζ phase, Ti_3Si_5 [119,160,247]. In these investigations, the precipitates were located in the γ phase or at lamellar interfaces, increasing the resistance to dislocation movement. On the other hand, Du et al. [168] reported a negative effect of Si, when investigating the alloy Ti-47Al-2Cr-1Nb-0.8Ta-0.2W-0.15B with and without 0.3Si addition prepared by powder extrusion. The authors explained that, in their particular work, not all Si atoms formed Ti_3Si_5 hence Si remained in solid solution. This in turn led to a higher concentration of vacancies in the lamellar interfaces that promoted dislocation climb, hence decreasing the creep resistance. It is worthy to mention that this effect was greatly dependent on the process conditions. Certainly the negative effect of Si additions could be improved by changing process parameters to ensure the precipitation of Ti_3Si_5. Therefore it is reasonable to state that Si

additions to titanium aluminides are beneficial to the creep resistance, as long as the ζ phase is precipitated.

In this study, the addition of 1 at.% Si to TNB-V5 increased the time to 1% strain. Yet, the best result was achieved with the alloy 3Nb-1Mo-1Si by the combined effects of solid solution hardening/slow diffusion (Mo addition) with precipitation strengthening induced by Si. The solubility of Si in titanium aluminides is believed to be low considering that silicides could be found with Si contents as low as 0.2 at.% [248,247]. According to the microstructure investigation and HEXRD measurements, the precipitates found in the as-sintered condition were the same as reported in previous publications, the ζ phase (Ti_3Si_5) [249,119,228,250]. The size and distribution of the precipitates could only be evaluated qualitatively but it was clear that precipitates in various sizes decorated the colony boundaries and were occasionally found inside the colonies. Therefore, the improvement in primary creep resistance was attributed to the presence of the ζ phase. The effect of precipitation strengthening though Si addition was evident comparing 1Si and TNB-V5, Figure 35.

The largest precipitate particles (for instance ~20 μm) are assumed to play no role in increasing primary creep resistance due to their reduced effectiveness as dislocation obstacles in comparison to the same fraction of finer precipitates at the lamellar interfaces and at the γ phase. The effect of these large particles in stress concentration and dislocation pile-up is only conjectural. Like pores, depending on the creep conditions, they might even lead to early cracking and low creep life.

Based on the XRD results of crept specimens, it is evident that a process of dynamic precipitation of ζ phase took place during creep testing. The extent of the precipitation was also proportional to the testing temperature. From the initial phase fraction of 3% in the as-sintered condition, the amounts of Ti_3Si_5 increased to 4% and 9% after creep testing at 800°C and 900 °C, respectively. The formation of ζ phase occurred at the expense of the α_2 phase, which decreased from 19% in the as-sintered condition to 13% after approximately 160 hours at 900 °C. The dissolution of the α_2 phase was described as a typical mechanism for the precipitation of the ζ phase during creep testing or aging [228,250,247]. As described by Gouma et. al. [251], silicides nucleate at the α_2/γ interface due to segregation of Si atoms and grow as the α_2 phase is decomposed. Consequently, the α_2/γ interface is consumed during the process. However, as the α_2 phase dissolves, it leaves an incoherent Ti_3Si_5 particle between the newly formed γ/γ interface, which contributes to the creep resistance.

Up to this date, there are significantly less research works available in regard to the effects of Gd in titanium aluminides than Si additions. Similar to Si, additions of Gd have been reported to increase the creep resistance of titanium aluminides by precipitation strengthening [170]. The solubility of Gd in titanium aluminides seems to be low, considering that early reports found Gd rich precipitates with 0.15 at.% Gd addition to Ti-44Al [120,169]. In this study, Gd-rich precipitates were found with 0.2 and 0.5 at.% Gd addition, however the precipitates in the 3Nb-0.2Gd alloy were smaller and more homogeneously distributed than in 3Nb-0.5Gd. The time to 1% strain of the Gd-containing specimens was overall longer or comparable to TNB-V5, Figure 35 and Figure 44.

Xia et al. [120] and Li et al. [169] studied the effect of Gd additions in cast titanium aluminides and found out that big Gd rich precipitates in a "finger like" morphology were formed during solidification. In a later work, Xia et al. [122], also reported the additional presence of fine precipitates on the interfaces of the lamellar structure after creep testing, thus indicating a dynamic precipitation effect. The authors explained that the very small particles precipitated as the α_2 phase dissolved during creep tests with tensile loading, which contributed to improve the creep strength in comparison to a Gd free counterpart. A similar mechanism can be assumed to take place in the alloy 3Nb-1Mo-1Si-0.2Gd when compared to the 3Nb-1Mo-1Si at 800 °C – 350 MPa, as shown in Figure 50. The time to 1% strain was the longest in these conditions and the amount of plastic deformation in primary creep was the lowest of all alloys tested (nearly 1%). Therefore, it is reasonable to conclude that in addition to the precipitates already present in the as-sintered condition, dynamic precipitation of Gd rich particles contributed to the improved primary creep resistance.

In contrast to the 3Nb-1Mo-1Si alloy, comparing Table 21 and Table 22, it seems that the dynamic precipitation of Gd particles not only occurred at the expense of α_2 but also of the retained β phase. The creep life was the lowest in all creep conditions tested, which indicates that the presence of precipitates associated with dissolution of interfaces and degradation of the microstructure are more critical with Gd additions. Even though the use of $GdSi_2$ as means for simultaneous introduction of Gd and Si led to more homogeneous microstructures and lower oxygen contents, the presence of large pores (>100 μm) in the sintered microstructure could not be avoided. This certainly shortened the creep life besides limiting the ductility at room temperature.

The nature of the Gd-containing precipitates is, however, unclear. Li et al. [169], based on selected area diffraction patterns and EDX results, tentatively identified these precipitates in

the alloy Ti-44Al-0.15Gd as the orthorhombic phase Gd_2TiO_5. The HEXRD results from 3Nb-1Mo-1Si-0.2Gd, Figure 54, contained peaks that could be successfully indexed as Gd_2TiO_5; however additional peaks that did not fit the Gd_2TiO_5 structure were also found. These peaks actually belonged to another Ti-Gd containing oxide, namely the TiGdO. Consequently, a mixture of oxides was present. The distribution and the temperature range in which each type of precipitate was formed could not be evaluated. Nonetheless, it is quite possible that for temperatures >800 °C, the Gd oxides either dissolved or lost their effectiveness. The primary creep resistance of 3Nb-1Mo-1Si-0.2Gd decreased as the test temperature increased (Figure 51 and Figure 52) clearly indicating loss of the strengthening effect of Gd additions.

7.5 Final Alloy Candidates

The aim of this research work was the development of a MIM-TiAl alloy with enhanced primary creep resistance. Based on the composition of TNB-V5, several alloying elements were tested leading to the Final Alloy Candidates. These compositions were prepared by MIM and creep tested using different parameters. Unfortunately, within the framework of this project, a thorough analysis of the creep behaviour was not possible. For that reason, the creep conditions were arranged as to provide a wide overview of the primary creep behaviour under critical high stress/temperature combinations.

The Larson-Miller Parameter (LPM) is a helpful approach to assess creep data of metals. It takes into account the temperature and time of each measurement and combines them into a parametric value. Normally the stress is plotted as a function of the LMP. The LMP is traditionally used to predict the creep life of heat resistant materials and for comparing the creep resistance of different materials. In Figure 59, the LMP plots of the Final Alloy Candidates are compared to the reference material, TNB-V5 also processed by MIM. The lines correspond to the time to 0.2, 0.5 and 1% plastic deformation.

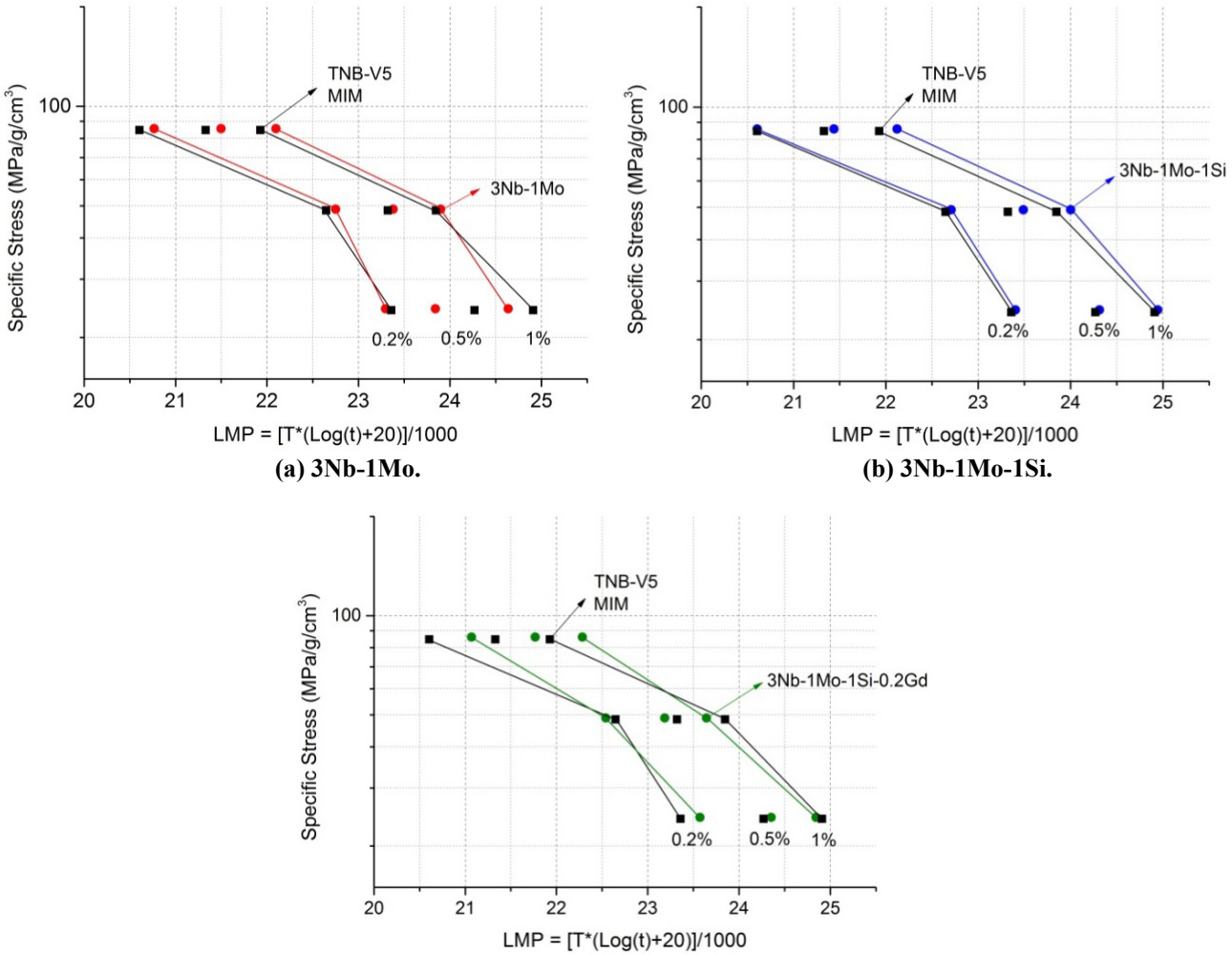

(a) 3Nb-1Mo.

(b) 3Nb-1Mo-1Si.

(c) 3Nb-1Mo-1Si-0.2Gd.

Figure 59 – Larson-Miller Parameter plots comparing the Final Alloy Candidates to TNB-V5.

In the high stress range, all alloys showed some improvement in primary creep resistance, yet the most pronounced increase was achieved by 3Nb-1Mo-1Si-0.2Gd. Considering that 3Nb-1Mo and 3Nb-1Mo-1Si showed similar behaviour, it is possible to conclude that the Gd-containing particles were mainly responsible for this increase, which is clearly seen in the time to 1% strain.

In the middle stress range, 3Nb-1Mo and 3Nb-1Mo-1Si showed better performance than TNB-V5. Although small, the difference between 3Nb-1Mo and 3Nb-1Mo-1Si can be attributed to the presence of the ζ phase since both alloys were otherwise microstructurally similar. On the other hand, 3Nb-1Mo-1Si-0.2Gd showed considerably lower primary creep resistance than TNB-V5. Considering that the points in this region of the LMP plot were measured at 950 °C, it is quite likely that at this temperature the Gd precipitates lose their dislocation pinning effect, as discussed previously.

At the low stress range, the alloys 3Nb-1Mo-1Si and 3Nb-1Mo-1Si-0.2Gd were quite comparable to TNB-V5, while 3Nb-1Mo was the least creep resistant material. The better performance of 3Nb-1Mo-1Si in comparison to 3Nb-1Mo indicates that the ζ phase was stable at the test temperature (900 °C). A possible reason for the poor creep resistance of 3Nb-1Mo could be the retained β phase. Obviously, with the exception of TNB-V5, all alloys contained retained β phase to some degree, however 3Nb-1Mo-1Si and 3Nb-1Mo-1Si-0.2Gd were additionally strengthened by precipitates. This probably counterbalanced the negative effect of the retained β phase.

In order to obtain a rough idea of the overall creep damage and to examine the effect of the retained β phase, failed specimens were cut in the region close to the fracture surface perpendicular to the loading direction and analysed in the SEM (Figure 60). The role of the retained β phase with regard to the creep resistance was in principle detrimental. As discussed earlier, besides facilitating diffusion due to its more open bcc structure, the β phase takes the heavy elements out of solid solution (assuming cooling out of thermodynamic equilibrium after sintering), thus decreasing the creep resistance. In fact, comparing the crept microstructures of Figure 60, it seems that β phase located at colony boundaries played a critical role in creep damage as site of crack initiation, as shown in Figure 60 (b).

The creep damage developed in the different materials presented distinct characteristics. TNB-V5 showed deformed wavy lamellae and the presence of creep pores in the vicinity of colony boundaries. In contrast, the creep damage of 3Nb-1Mo was greatly concentrated at the β phase in the colony boundaries resulting in sharp cracks. This particular behaviour changes as Si was added. In the alloy 3Nb-1Mo-1Si, wavy lamellae and more roundish creep porosity could be found, similar to TNB-V5. The addition of Gd seems to have promoted more γ phase recrystallisation at the colony boundaries but the creep voids were comparable to the 3Nb-1Mo-1Si alloy.

Even though 3Nb-1Mo-1Si-0.2Gd contained the largest phase fraction of β phase in the as-sintered condition (before creep testing), the analysis of the fractured specimens indicates that due to precipitate strengthening in the colony boundaries, the creep damage was differently distributed. Without further precipitation strengthening, the retained β phase led to the formation of sharp cracks, as in the case of the alloy 3Nb-1Mo, but due to precipitation strengthening it becomes apparently less critical for the creep damage, as in the case of the alloy 3Nb-1Mo-1Si-0.2Gd.

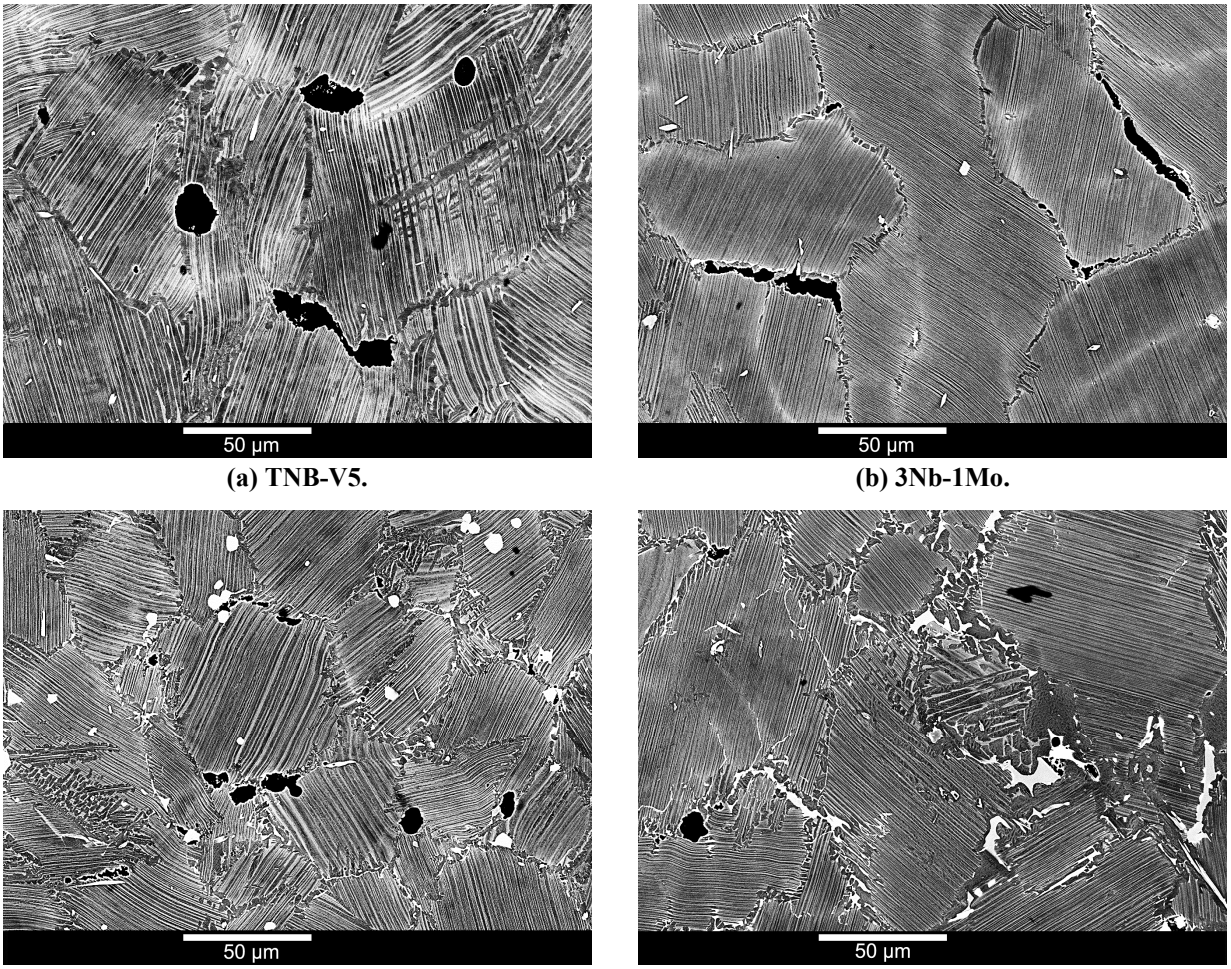

(a) TNB-V5. **(b) 3Nb-1Mo.**

(c) 3Nb-1Mo-1Si. **(d) 3Nb-1Mo-1Si-0.2Gd**

Figure 60 – Microstructures of creep fractured specimens tested at 800 °C – 350 MPa.

During the primary creep stage, the plastic strain mainly occurs at the lamellar interface through the generation of interfacial dislocations and dislocation loops in the γ phase [90]. Consequently, the primary creep resistance is greatly dependent on the morphology of the lamellar interfaces to hinder dislocation glide and climb. Obviously, both approaches of introducing obstacles that reduce dislocation motion such as precipitates and adding heavy atoms to reduce diffusivity were successful in the Final Alloy Candidates. Nevertheless, the performance at a specific temperature and load combination as well as the development and distribution of creep damage were different. Despite some side effects, e.g. lower creep life, the optimisation of primary creep resistance was successfully achieved in the case of all Final Alloy Candidates at 800 °C – 350 MPa.

8. Conclusions

This research work constituted a pioneering and exploratory characterisation effort of creep resistance of titanium aluminides prepared by Metal Injection Moulding (MIM). It was simultaneously an attempt to optimise primary creep at high stress/temperature combinations through alloy design. The preparation of reliable specimens was of great concern and an extensive study on sintering behaviour of pre-alloyed and pre-alloyed + elemental powder blends was necessary. After careful analysis of the experimental data, the following conclusions could be drawn:

Processing of titanium aluminides through MIM is possible and sound specimens with very low porosity could be achieved. The microstructures formed through sintering are fine and contain colony size usually in the order of 80 μm or smaller, independent of composition. The presence of contaminations, in particular O, C and N that are typically higher than in cast materials might lead to precipitates. However, their effect in primary creep resistance is in principle not detrimental.

The pre-alloyed approach for the preparation of specimens is more advantageous than blending pre-alloyed and elemental powders. The porosity was lower and also the microstructure homogeneity could be improved by decreasing the amounts of elemental powders added. On the other hand, if only small compositional variations from the master alloy are required, the pre-alloyed blended elemental powder approach is a powerful technique for the preparation of different compositions. Changes in the sintering behaviour need nonetheless to be taken into account.

Even though specimens processed by MIM, as many other powder metallurgy processes, inevitably contain residual porosity, the UTS at room temperature were quite comparable to the as-cast or cast and HIP conditions of similar alloys. Nevertheless, the ductility was lower due to the increased amount of contamination that is inherent to the MIM process. The porosity additionally decreased the primary creep resistance. Consequently, the minimisation of porosity through proper sintering parameters is essential for the mechanical performance of MIM-TiAl.

The investigation of primary creep resistance through compression creep led to significant results that were qualitatively similar to the tensile creep experiments. However, the creep

resistance measured in compression was higher than in tension, which is in agreement with previous works.

Several alloying elements were evaluated for the improvement of primary creep resistance; however the alloy variations were limited to compositions close to TNB-V5 (Ti-45Al-5Nb-0.2B-0.2C). Given the importance of climb and glide of dislocations in primary creep, two main mechanisms were employed: (i) the introduction of heavy elements to slow down diffusional processes and simultaneously increase the glide resistance of dislocations through solid solution hardening, which was achieved by adding W, Ta, Nb and Mo; (ii) precipitation strengthening to pin dislocations while moving in the γ phase, achieved by additions of Si and Gd. After the extensive screening phases, from all the alloys tested three showed significantly improved performance regarding primary creep resistance:

- Ti-44.5Al-3Nb-1Mo-0.2B-0.2C;
- Ti-44.5Al-3Nb-1Mo-1Si-0.2B-0.2C;
- Ti-44.5Al-3Nb-1Mo-1Si-0.2Gd-0.2B-0.2C.

All alloys mentioned achieved improved primary creep resistance at 800 °C – 350 MPa in comparison to the reference material. These alloys rely on the presence of the heavy atoms Mo and Nb and of precipitates. According to the structural characterisation, Si-containing precipitates were identified as the ζ phase, while Gd-containing precipitates were composed of a mixture of Gd oxides.

The alloy Ti-44.5Al-3Nb-1Mo-1Si-0.2Gd-0.2B-0.2C showed the highest primary creep resistance at 800 °C – 350 MPa. However, at higher temperatures it was the least resistant, indicating that the strengthening precipitates lose their effect above 800 °C. The alloy Ti-44.5Al-3Nb-1Mo-1Si-0.2B-0.2C achieved the most balanced creep resistance in all conditions tested and it was also slightly superior to the reference material.

The large body of experimental work conducted reveals that the production of creep resistant and reliable MIM-TiAl is feasible. However with the optimisation of one property, another is likely to decrease. Therefore, a compromise of properties is essential, considering that some issues such as porosity and contamination are inevitable. Nevertheless, with the correct process parameters, particularly concerning sintering, and the use of an adequate alloy, high quality parts with performances comparable to competing techniques might be achieved at significantly lower costs.

9. References

[1] F.H. Froes, C. Suryanarayana, D. Eliezer, J Mater Sci 27 (1992) 5113.
[2] T. Tetsui, Current Opinion in Solid State and Materials Science 4 (1999) 243.
[3] M. Dahms, Adv Perform Mater 1 (1994) 157.
[4] D. Dimiduk, Materials Science and Engineering: A 263 (1999) 281.
[5] T. Tetsui, Materials Science and Engineering: A 329–331 (2002) 582.
[6] X. Wu, Intermetallics 14 (2006) 1114.
[7] W. Shouren, G. Peiquan, Y. Liying, Journal of Materials Processing Technology 204 (2008) 492.
[8] H. Zhu, T. Wei, D. Carr, R. Harrison, L. Edwards, W. Hoffelner, D. Seo, K. Maruyama, JOM 64 (2012) 1418.
[9] H. Clemens, S. Mayer, Advanced Engineering Materials 15 (2013) 191.
[10] F. Appel, J.D.H. Paul, M. Oehring, Gamma Titanium Aluminide Alloys: Science and Technology, First ed., Weinheim, 2011.
[11] J.P. Kuang, R.A. Harding, J. Campbell, Materials Science and Engineering: A 329–331 (2002) 31.
[12] M.T. Jovanović, B. Dimčić, I. Bobić, S. Zec, V. Maksimović, Journal of Materials Processing Technology 167 (2005) 14.
[13] D. Hu, X. Wu, M.H. Loretto, Intermetallics 13 (2005) 914.
[14] Z.M. Hu, T.A. Dean, Journal of Materials Processing Technology 111 (2001) 10.
[15] T. Tetsui, K. Shindo, S. Kaji, S. Kobayashi, M. Takeyama, Intermetallics 13 (2005) 971.
[16] Y.C. Kim, S. Lee, S. Ahn, N.J. Kim, J Mater Sci 42 (2007) 2048.
[17] R. Gerling, H. Clemens, F.P. Schimansky, Advanced Engineering Materials 6 (2004) 23.
[18] G. Molénat, M. Thomas, J. Galy, A. Couret, Advanced Engineering Materials 9 (2007) 667.
[19] J.C. Rawers, W.R. Wrzesinski, J Mater Sci 27 (1992) 2877.
[20] G.-X. Wang, M. Dahms, MTA 24 (1993) 1517.
[21] M. Dahms, G. Leitner, W. Poessnecker, S. Schultrich, F. Schmelzer, Z. Metallk. 84 (1993) 351.
[22] M. Dahms, T.J. Jewett, C. Michaelsen, Zeitschrift Für Metallkunde 88 (1997) 125.
[23] G.-X. Wang, B. Dogan, F.-Y. Hsu, H.-J. Klaar, M. Dahms, MMTA 26 (1995) 691.
[24] K. Taguchi, M. Ayada, K.N. Ishihara, P.H. Shingu, Intermetallics 3 (1995) 91.
[25] T. Lee, J. Kim, S. Hwang, Metallurgical and Materials Transactions A 28 (1997) 2723.
[26] G. Das, H. Kestler, H. Clemens, P.A. Bartolotta, JOM 56 (2004) 42.
[27] R. Gerling, A. Bartels, H. Clemens, H. Kestler, F.-P. Schimansky, Intermetallics 12 (2004) 275.
[28] L.E. Murr, S.M. Gaytan, A. Ceylan, E. Martinez, J.L. Martinez, D.H. Hernandez, B.I. Machado, D.A. Ramirez, F. Medina, S. Collins, R.B. Wicker, Acta Materialia 58 (2010) 1887.
[29] S. Biamino, A. Penna, U. Ackelid, S. Sabbadini, O. Tassa, P. Fino, M. Pavese, P. Gennaro, C. Badini, Intermetallics 19 (2011) 776.
[30] D. Srivastava, I.T.H. Chang, M.H. Loretto, Materials & Design 21 (2000) 425.
[31] W. Liu, J.N. DuPont, Metall and Mat Trans A 35 (2004) 1133.
[32] R. Gerling, F.-P. Schimansky, G. Wegmann, Advanced Engineering Materials 3 (2001) 387.
[33] R. Gerling, F.-P. Schimansky, Materials Science and Engineering A 329-331 (2002) 45.
[34] R. Gerling, E. Aust, W. Limberg, M. Pfuff, F.P. Schimansky, Materials Science and Engineering: A 423 (2006) 262.
[35] H. Zhang, X. He, X. Qu, L. Zhao, Materials Science and Engineering: A 526 (2009) 31.

[36] T. Ebel, O. Milagres Ferri, W. Limberg, M. Oehring, F. Pyczak, F.P. Schimansky, Key Engineering Materials 520 (2012) 153.
[37] W. Limberg, T. Ebel, F. Pyczak, M. Oehring, F.P. Schimansky, Materials Science and Engineering: A 552 (2012) 323.
[38] S. Terauchi, T. Teraoka, T. Shinkuma, T. Sugimoto, Funtai Oyobi Fummatsu Yakin/Journal of the Japan Society of Powder and Powder Metallurgy 47 (2000) 1283.
[39] T. Ebel, O.M. Ferri, W. Limberg, F.-P. Imansky, in:, Advances in Powder Metallurgy and Particulate Materials - 2011, Proceedings of the 2011 International Conference on Powder Metallurgy and Particulate Materials, PowderMet 2011, 2011, pp. 445–457.
[40] K.-U. Kainer, T. Ebel, O.M. Ferri, W. Limberg, F. Pyczak, F.-P. Schimansky, M. Wolff, Powder Metallurgy 55 (2012) 315.
[41] W.J. Zhang, S.C. Deevi, Intermetallics 11 (2003) 177.
[42] D.Y. Seo, L. Zhao, J. Beddoes, Metall and Mat Trans A 34 (2003) 2177.
[43] T.A. Parthasarathy, M. Keller, M.G. Mendiratta, Scripta Materialia 38 (1998) 1025.
[44] J. Beddoes, D.Y. Seo, W.R. Chen, L. Zhao, Intermetallics 9 (2001) 915.
[45] W.R. Chen, J. Beddoes, L. Zhao, Materials Science and Engineering: A 323 (2002) 306.
[46] D.Y. Seo, T. Sawatzky, H. Saari, D.J. Kim, P. Au, C.S. Seok, J Mech Sci Technol 26 (2012) 2009.
[47] T. Sawatzky, D.Y. Seo, H. Saari, D. Laurin, Y.-W. Kim, The Microstructure, Creep, and Hardness Properties of Powder Metallurgy Beta Gamma TiAl-4Nb-3Mn Alloy, 2012.
[48] D.Y. Seo, T.R. Bieler, S.U. An, D.E. Larsen, Metall and Mat Trans A 29 (1998) 89.
[49] J. Malaplate, M. Thomas, P. Belaygue, M. Grange, A. Couret, Acta Materialia 54 (2006) 601.
[50] M.A. Morris, T. Lipe, Intermetallics 5 (1997) 329.
[51] M.A. Morris, M. Leboeuf, Intermetallics 5 (1997) 339.
[52] F. Appel, M. Oehring, R. Wagner, Intermetallics 8 (2000) 1283.
[53] F. Appel, J.D.H. Paul, M. Oehring, U. Fröbel, U. Lorenz, Metall and Mat Trans A 34 (2003) 2149.
[54] D. Peter, J. Pfetzing, M.F.-X. Wagner, G. Eggeler, Materials Science and Engineering: A 510–511 (2009) 368.
[55] G. Sauthoff, Intermetallics, John Wiley & Sons, 2008.
[56] G. Lütjering, J.C. Williams, Titanium, Springer, 2007.
[57] E.A. Loria, Intermetallics 8 (2000) 1339.
[58] F. Appel, M. Oehring, in:, C. Leyens, M. Peters (Eds.), Titanium and Titanium Alloys, First ed., Wiley-VCH Verlag GmbH & Co. KGaA, 2003, pp. 89–152.
[59] J.C. Schuster, M. Palm, JPED 27 (2006) 255.
[60] W.G. Burgers, Physica 1 (1934) 561.
[61] A.K. Singh, K. Muraleedharan, D. Banerjee, Scripta Materialia 48 (2003) 767.
[62] D.R. Johnson, H. Inui, M. Yamaguchi, Intermetallics 6 (1998) 647.
[63] V. Küstner, M. Oehring, A. Chatterjee, V. Güther, H.-G. Brokmeier, H. Clemens, F. Appel, Gamma Titanium Aluminides 2003 (2003) 89.
[64] R.M. Imayev, V.M. Imayev, M. Oehring, F. Appel, Intermetallics 15 (2007) 451.
[65] S. Naka, M. Thomas, C. Sanchez, T. Khan, Development of Third Generation Castable Gamma Titanium Aluminides: Role of Solidification Paths, Minerals, Metals & Materials Soc, Warrendale, 1996.
[66] Y. Jin, J.N. Wang, J. Yang, Y. Wang, Scripta Materialia 51 (2004) 113.
[67] Y. Wang, Y. Liu, G. Yang, H. Li, B. Tang, Transactions of Nonferrous Metals Society of China 21 (2011) 215.
[68] M. Takeyama, M. Kikuchi, Intermetallics 6 (1998) 573.
[69] M.J. Blackburn, The Science, Technolgy, and Application of Titanium. / Jaffee, R. I. (ed.). Oxford Pergamon Press Ltd. 43 (1970) 663.
[70] Y.-W. (Y-W.. Kim, Acta Metallurgica et Materialia 40 (1992) 1121.

[71] Y.-W. Kim, JOM 46 (1994) 30.
[72] K. Maruyama, R. Yamamoto, H. Nakakuki, N. Fujitsuna, Materials Science and Engineering: A 239-240 (1997) 419.
[73] Y.-W. Kim, D.M. Dimiduk, JOM 43 (1991) 40.
[74] Y.-W. Kim, Intermetallics 6 (1998) 623.
[75] C. Leyens, M. Peters, eds., Titanium and Titanium Alloys: Fundamentals and Applications, 2005.
[76] F.R.N. Nabarro, F. de Villiers, Physics Of Creep And Creep-Resistant Alloys, CRC Press, 1995.
[77] M.E. Kassner, Fundamentals of Creep in Metals and Alloys, Elsevier, 2008.
[78] J. Beddoes, W. Wallace, L. Zhao, International Materials Reviews 40 (1995) 197.
[79] J.E. Dorn, Journal of the Mechanics and Physics of Solids 3 (1955) 85.
[80] B.F. Dyson, M. McLean, Acta Metallurgica 31 (1983) 17.
[81] K. Sawada, H. Kushima, M. Tabuchi, K. Kimura, Materials Science and Engineering: A 528 (2011) 5511.
[82] S. Takeuchi, A.S. Argon, J Mater Sci 11 (1976) 1542.
[83] R.E. Frenkel, O.D. Sherby, J.E. Dorn, Acta Metallurgica 3 (1955) 470.
[84] O.D. Sherby, J.L. Lytton, J.E. Dorn, Acta Metallurgica 5 (1957) 219.
[85] M.S. Soliman, J Mater Sci 22 (1987) 3529.
[86] S.-C. Huang, MTA 23 (1992) 375.
[87] P.M. Hazzledine, Intermetallics 6 (1998) 673.
[88] T.A. Parthasarathy, M.G. Mendiratta, D.M. Dimiduk, Scripta Materialia 37 (1997) 315.
[89] J.A. Wert, M.F. Bartholomeusz, MMTA 27 (1996) 127.
[90] W.R. Chen, J. Triantafillou, J. Beddoes, L. Zhao, Intermetallics 7 (1999) 171.
[91] C.E. Wen, K. Yasue, J.G. Lin, Y.G. Zhang, C.Q. Chen, Intermetallics 8 (2000) 525.
[92] P.D. Crofts, P. Bowen, I.P. Jones, Scripta Materialia 35 (1996) 1391.
[93] A. Chatterjee, H. Mecking, E. Arzt, H. Clemens, Materials Science and Engineering: A 329–331 (2002) 840.
[94] R. Yamamoto, K. Mizoguchi, G. Wegmann, K. Maruyama, Intermetallics 6 (1998) 699.
[95] W. Schillinger, H. Clemens, G. Dehm, A. Bartels, Intermetallics 10 (2002) 459.
[96] H. Zhu, D.Y. Seo, K. Maruyama, P. Au, Scripta Materialia 54 (2006) 1979.
[97] T.A. Parthasarathy, P.R. Subramanian, M.G. Mendiratta, D.M. Dimiduk, Acta Materialia 48 (2000) 541.
[98] W.J. Zhang, S.C. Deevi, Intermetallics 10 (2002) 603.
[99] J.N. Wang, A.J. Schwartz, T.G. Nieh, D. Clemens, Materials Science and Engineering: A 206 (1996) 63.
[100] B.J. Cane, P.F. Aplin, The Journal of Strain Analysis for Engineering Design 29 (1994) 225.
[101] M. Es-souni, A. Bartels, R. Wagner, Acta Metallurgica et Materialia 43 (1995) 153.
[102] K. Maruyama, M. Yamaguchi, G. Suzuki, H. Zhu, H.Y. Kim, M.H. Yoo, Acta Materialia 52 (2004) 5185.
[103] H.S. Cho, S.W. Nam, Y.-W. Kim, Metals and Materials 4 (1998) 33.
[104] L.M. Hsiung, T.G. Nieh, Scripta Materialia 36 (1997) 323.
[105] R. Kainuma, Y. Fujita, H. Mitsui, I. Ohnuma, K. Ishida, Intermetallics 8 (2000) 855.
[106] S.-C. Huang, E.L. Hall, MTA 22 (1991) 427.
[107] T. Tsujimoto, K. Hashimoto, High-Temperature Ordered Intermetallic Alloys III 133 (1989) 133.
[108] S.-C. Huang, E.L. Hall, Acta Metallurgica et Materialia 39 (1991) 1053.
[109] T. Kawabata, T. Tamura, O. Izumi, MTA 24 (1993) 141.
[110] J.C. Beddoes, W. Wallace, M.C. de Malherbe, Materials and Manufacturing Processes 7 (1992) 527.
[111] T.T. Cheng, M.R. Willis, I.P. Jones, Intermetallics 7 (1999) 89.

[112] D.Y. Seo, J. Beddoes, L. Zhao, G.A. Botton, Materials Science and Engineering: A 329–331 (2002) 810.
[113] U. Hecht, V. Witusiewicz, A. Drevermann, J. Zollinger, Intermetallics 16 (2008) 969.
[114] M. Oehring, A. Stark, J.D.H. Paul, T. Lippmann, F. Pyczak, Intermetallics 32 (2013) 12.
[115] W.H. Tian, M. Nemoto, Intermetallics 5 (1997) 237.
[116] P.I. Gouma, S.J. Davey, M.H. Loretto, Materials Science and Engineering: A 241 (1998) 151.
[117] T. Kawabata, T. Abumiya, O. Izumi, Acta Metallurgica et Materialia 40 (1992) 2557.
[118] H.S. Cho, S.W. Nam, J.H. Yun, D.M. Wee, Materials Science and Engineering: A 262 (1999) 129.
[119] T. Noda, M. Okabe, S. Isobe, M. Sayashi, Materials Science and Engineering: A 192–193, Part 2 (1995) 774.
[120] K. Xia, W. Li, C. Liu, Scripta Materialia 41 (1999) 67.
[121] C.M. Liu, W. Li, K. Xia, Journal of Materials Science 35 (2000) 975.
[122] K. Xia, X. Wu, D. Song, Acta Materialia 52 (2004) 841.
[123] S.-C. Huang, E.L. Hall, MTA 22 (1991) 2619.
[124] M. Morinaga, J. Saito, N. Yukawa, H. Adachi, Acta Metallurgica et Materialia 38 (1990) 25.
[125] T. Tsujimoto, K. Hashimoto, M. Nobuki, JIM, Materials Transactions 33 (1992) 989.
[126] T. Hanamura, M. Tanino, J Mater Sci Lett 8 (1989) 24.
[127] Y.L. Hao, R. Yang, Y.Y. Cui, D. Li, Intermetallics 8 (2000) 633.
[128] A.K. Singh, D. Banerjee, Metall and Mat Trans A 28 (1997) 1745.
[129] J.D.H. Paul, F. Appel, R. Wagner, Acta Materialia 46 (1998) 1075.
[130] A.M. Hodge, L.M. Hsiung, T.G. Nieh, Scripta Materialia 51 (2004) 411.
[131] D. Vojtěch, T. Popela, J. Hamáček, J. Kützendörfer, Materials Science and Engineering: A 528 (2011) 8557.
[132] M. Schloffer, B. Rashkova, T. Schöberl, E. Schwaighofer, Z. Zhang, H. Clemens, S. Mayer, Acta Materialia 64 (2014) 241.
[133] J. Lapin, T. Pelachová, M. Dománková, Intermetallics 19 (2011) 814.
[134] H. Saage, A.J. Huang, D. Hu, M.H. Loretto, X. Wu, Intermetallics 17 (2009) 32.
[135] P.L. Martin, M.G. Mendiratta, H.A. Lipsitt, MTA 14 (1983) 2170.
[136] G.E. Fuchs, Materials Science and Engineering: A 192–193, Part 2 (1995) 707.
[137] H. Zhu, D.Y. Seo, K. Maruyama, P. Au, Scripta Materialia 54 (2006) 425.
[138] L. Huang, P.K. Liaw, C.T. Liu, Metall and Mat Trans A 38 (2007) 2290.
[139] R. Yu, L.L. He, Z.Y. Cheng, J. Zhu, H.Q. Ye, Intermetallics 10 (2002) 661.
[140] Y. Shida, H. Anada, Oxid Met 45 (1996) 197.
[141] Y.G. Li, M.H. Loretto, Acta Metallurgica et Materialia 42 (1994) 2913.
[142] H. Clemens, W. Wallgram, S. Kremmer, V. Güther, A. Otto, A. Bartels, Advanced Engineering Materials 10 (2008) 707.
[143] V. Imayev, T. Khismatullin, R. Imayev, Phys. Metals Metallogr. 109 (2010) 402.
[144] T. Sawatzky, D.Y. Seo, H. Saari, D. Laurin, D.J. Kim, Y.W. Kim, Materials Science Forum 654-656 (2010) 500.
[145] C. Qiu, Y. Liu, L. Huang, B. Liu, W. Zhang, Y. He, B. Huang, Transactions of Nonferrous Metals Society of China 22 (2012) 2593.
[146] V.M. Imaev, R.M. Imaev, T.I. Oleneva, T.G. Khismatullin, Phys. Metals Metallogr. 106 (2008) 641.
[147] M. Oehring, J.D.H. Paul, U. Lorenz, F. Appel, Titanium Aluminide Based Alloy, US 2010/0015005 A1, 2010.
[148] M. Schloffer, F. Iqbal, H. Gabrisch, E. Schwaighofer, F.-P. Schimansky, S. Mayer, A. Stark, T. Lippmann, M. Göken, F. Pyczak, H. Clemens, Intermetallics 22 (2012) 231.

[149] W. Smarsly, H. Clemens, V. Güther, S. Kremmer, A. Otto, H. Chladil, Material for a Gas Turbine Component, Method for Producing a Gas Turbine Component and Gas Turbine Component, WO2009/052792 A8, 2009.
[150] S. Becker, A. Rahmel, M. Schorr, M. Schütze, Oxid Met 38 (1992) 425.
[151] W.J. Zhang, S.C. Deevi, G.L. Chen, Intermetallics 10 (2002) 403.
[152] M. Lamirand, J.-L. Bonnentien, G. Ferrière, S. Guérin, J.-P. Chevalier, Scripta Materialia 56 (2007) 325.
[153] C.J. Rossouw, C.T. Forwood, M.A. Gibson, P.R. Miller, Philosophical Magazine A 74 (1996) 77.
[154] Y.-W. Kim, A. Rosenberger, D.M. Dimiduk, Intermetallics 17 (2009) 1017.
[155] W.J. Zhang, G.L. Chen, F. Appel, T.G. Nieh, S.C. Deevi, Materials Science and Engineering: A 315 (2001) 250.
[156] W.J. Zhang, Z.C. Liu, G.L. Chen, Y.-W. Kim, Materials Science and Engineering A 271 (1999) 416.
[157] M. Oehring, F. Appel, P.J. Ennis, R. Wagner, Intermetallics 7 (1999) 335.
[158] T. Kawabata, M. Tadano, O. Izumi, ISIJ International 31 (1991) 1161.
[159] W.H. Tian, T. Sano, M. Nemoto, Philosophical Magazine A 68 (1993) 965.
[160] M. Karadge, P.I. Gouma, Y.-W. Kim, Metall and Mat Trans A 34 (2003) 2129.
[161] F. Perdrix, M.-F. Trichet, J.-L. Bonnentien, M. Cornet, J. Bigot, Intermetallics 9 (2001) 807.
[162] H. Gabrisch, A. Stark, F.-P. Schimansky, L. Wang, N. Schell, U. Lorenz, F. Pyczak, Intermetallics 33 (2013) 44.
[163] W.H. Tian, M. Nemoto, Intermetallics 13 (2005) 1030.
[164] D.J. Larson, C.T. Liu, M.K. Miller, Intermetallics 5 (1997) 411.
[165] M.E. Hyman, C. McCullough, C.G. Levi, R. Mehrabian, MTA 22 (1991) 1647.
[166] D.J. Larson, C.T. Liu, M.K. Miller, Materials Science and Engineering: A 239–240 (1997) 220.
[167] W.J. Zhang, S.C. Deevi, Materials Science and Engineering: A 362 (2003) 280.
[168] X.-W. Du, J.. Wang, J. Zhu, Intermetallics 9 (2001) 745.
[169] W. Li, B. Inkson, Z. Horita, K. Xia, Intermetallics 8 (2000) 519.
[170] X. Wu, D. Song, K. Xia, Materials Science and Engineering: A 329–331 (2002) 821.
[171] C. Liu, K. Xia, W. Li, Journal of Materials Science 37 (2002) 1515.
[172] X. Chang, J. Si, F. Gao, Y. Jing, J. Zhang, Journal of Iron and Steel Research, International 14 (2007) 26.
[173] R.M. German, A. Bose, Injection Molding of Metals and Ceramics, Metal Powder Industries Federation, 1997.
[174] K. Kato, Metal Powder Report 48 (1993) 49.
[175] Y. Ahida, Metal Powder Report 58 (2003) 38.
[176] G.C. Obasi, O.M. Ferri, T. Ebel, R. Bormann, Materials Science and Engineering: A 527 (2010) 3929.
[177] O.M. Ferri, T. Ebel, R. Bormann, Materials Science and Engineering: A 527 (2010) 1800.
[178] J. Soyama, M. Oehring, W. Limberg, T. Ebel, K. Kainer, F. Pyczak, in:, European Powder Metallurgy Association, Basel, 2012, pp. 151–156.
[179] H. Clemens, A. Bartels, S. Bystrzanowski, H. Chladil, H. Leitner, G. Dehm, R. Gerling, F.P. Schimansky, Intermetallics 14 (2006) 1380.
[180] D. Hu, C. Yang, A. Huang, M. Dixon, U. Hecht, Intermetallics 23 (2012) 49.
[181] M. Mirjalili, M. Soltanieh, K. Matsuura, M. Ohno, Intermetallics 32 (2013) 297.
[182] C. Michaelsen, S. Wöhlert, R. Bormann, MRS Online Proceedings Library 343 (1994) 205.
[183] S. Wohlert, R. Bormann, Journal of Applied Physics 85 (1999) 825.
[184] T.K. Lee, E.I. Mosunov, S.K. Hwang, Materials Science and Engineering: A 239-240 (1997) 540.

[185] G.-X. Wang, M. Dahms, Scripta Metallurgica et Materialia 26 (1992) 1469.
[186] T. Schmoelzer, K.-D. Liss, G.A. Zickler, I.J. Watson, L.M. Droessler, W. Wallgram, T. Buslaps, A. Studer, H. Clemens, Intermetallics 18 (2010) 1544.
[187] C.J. Butler, D.G. McCartney, Acta Materialia 46 (1998) 1875.
[188] R.M. German, Powder Metallurgy Science, First ed., Metal Powder Industry, New Jersey, 1994.
[189] Y. Mishin, C. Herzig, Acta Materialia 48 (2000) 589.
[190] M. Oehring, A. Stark, J.D.H. Paul, T. Lippmann, F. Pyczak, Intermetallics 32 (2013) 12.
[191] E. Baril, L.P. Lefebvre, Y. Thomas, Powder Metallurgy 54 (2013) 183.
[192] Z. Liu, G. Welsch, MTA 19 (1988) 527.
[193] A. Menand, A. Huguet, A. Nérac-Partaix, Acta Materialia 44 (1996) 4729.
[194] A. Huguet, A. Menand, Applied Surface Science 76–77 (1994) 191.
[195] A. Menand, H. Zapolsky-Tatarenko, A. Nérac-Partaix, Materials Science and Engineering: A 250 (1998) 55.
[196] A. Nérac-Partaix, A. Menand, Scripta Materialia 35 (1996) 199.
[197] M.A. Pietzka, J.C. Schuster, JPE 15 (1994) 392.
[198] C.Y. Nam, D.M. Wee, P. Wang, K.S. Kumar, Intermetallics 10 (2002) 113.
[199] J.H. Yun, M.H. Oh, S.W. Nam, D.M. Wee, H. Inui, M. Yamaguchi, Materials Science and Engineering: A 239–240 (1997) 702.
[200] D.Y. Seo, S. Bulmer, H. Saari, P. Au, Materials Science Forum 561-565 (2007) 481.
[201] A.N. Khan, A. Usman, Journal of Alloys and Compounds 491 (2010) 209.
[202] ASTM E384, Test Method for Knoop and Vickers Hardness of Materials, ASTM International, 2011.
[203] M. Yamaguchi, H. Inui, K. Ito, Acta Materialia 48 (2000) 307.
[204] S. Djanarthany, J.-C. Viala, J. Bouix, Materials Chemistry and Physics 72 (2001) 301.
[205] K. Kothari, R. Radhakrishnan, N.M. Wereley, Progress in Aerospace Sciences 55 (2012) 1.
[206] Y.-W. Kim, Materials Science and Engineering: A 192–193, Part 2 (1995) 519.
[207] C. Koeppe, A. Bartels, J. Seeger, H. Mecking, MTA 24 (1993) 1795.
[208] C. Mercer, W.O. Soboyejo, Scripta Materialia 35 (1996) 17.
[209] J.Y. Jung, J.K. Park, C.H. Chun, S.M. Her, Materials Science and Engineering: A 220 (1996) 185.
[210] G. Cao, L. Fu, J. Lin, Y. Zhang, C. Chen, Intermetallics 8 (2000) 647.
[211] J. Tang, B. Huang, Y. He, W. Liu, K. Zhou, A. Wu, Materials Research Bulletin 37 (2002) 1315.
[212] N. Hansen, Scripta Materialia 51 (2004) 801.
[213] A.N. Stroh, Philosophical Magazine Series 7 46 (1955) 968.
[214] D. Hu, J.F. Mei, M. Wickins, R.A. Harding, Scripta Materialia 47 (2002) 273.
[215] X. Wu, D. Hu, Scripta Materialia 52 (2005) 731.
[216] S.L. Semiatin, V. Seetharaman, V.K. Jain, MMTA 25 (1994) 2753.
[217] D.M. Dimiduk, P.L. Martin, Y.-W. Kim, Materials Science and Engineering A 243 (1998) 66.
[218] G.P. Tilly, G.F. Harrison, The Journal of Strain Analysis for Engineering Design 7 (1972) 163.
[219] G.E. Lucas, R.M.N. Pelloux, MTA 12 (1981) 1321.
[220] M. El-Shennawy, Y. Morita, M. Kouso, JSME International Journal Series A 42 (1999) 403.
[221] S.K. Sondhi, B.F. Dyson, M. McLean, Acta Materialia 52 (2004) 1761.
[222] S. Sujatanond, Y. Mutoh, Y. Miyashita, Y. Otsuka, Applied Mechanics and Materials 313-314 (2013) 98.
[223] O.V. Sosnin, J Appl Mech Tech Phys 11 (1970) 832.
[224] J.G. Wang, L.M. Hsiung, T.G. Nieh, Intermetallics 7 (1999) 757.

[225] M. Es-Souni, A. Bartels, R. Wagner, Materials Science and Engineering: A 192–193, Part 2 (1995) 698.
[226] K.S. Chan, Y.-W. Kim, Acta Metallurgica et Materialia 43 (1995) 439.
[227] D.M. Dimiduk, P.M. Hazzledine, T.A. Parthasarathy, M.G. Mendiratta, S. Seshagiri, Metall and Mat Trans A 29 (1998) 37.
[228] P.-I. Gouma, K. Subramanian, Y.-W. Kim, M.J. Mills, Intermetallics 6 (1998) 689.
[229] M.A. Morris, Intermetallics 4 (1996) 417.
[230] M. Lamirand, J.-L. Bonnentien, S. Guérin, G. Ferrière, J.-P. Chevalier, Metall and Mat Trans A 37 (2006) 2369.
[231] H. Ding, G. Nie, R. Chen, J. Guo, H. Fu, Materials & Design 41 (2012) 108.
[232] O.M. Ferri, T. Ebel, R. Bormann, Materials Science and Engineering: A 504 (2009) 107.
[233] L. Bolzoni, E.M. Ruiz-Navas, E. Gordo, Materials Characterization 84 (2013) 48.
[234] Y. Yan, G.L. Nash, P. Nash, International Journal of Fatigue 55 (2013) 81.
[235] J. Zhang, J. Li, T. Jin, X. Sun, Z. Hu, Journal of Materials Science & Technology 26 (2010) 889.
[236] E.M. Gutman, Y. Unigovski, M. Levkovitch, Z. Koren, Journal of Materials Science Letters 17 (1998) 1787.
[237] M.H. Loretto, A.B. Godfrey, D. Hu, P.A. Blenkinsop, I.P. Jones, T.T. Cheng, Intermetallics 6 (1998) 663.
[238] E. Hamzah, M. Kanniah, M. Harun, Materials Science and Engineering: A 483–484 (2008) 555.
[239] S. Nishikiori, S. Takahashi, S. Satou, T. Tanaka, T. Matsuo, Materials Science and Engineering: A 329–331 (2002) 802.
[240] J.G. Wang, T.G. Nieh, Intermetallics 8 (2000) 737.
[241] B.J. Inkson, C.B. Boothroyd, C.J. Humphreys, Acta Metallurgica et Materialia 41 (1993) 2867.
[242] N. Masahashi, Y. Mizuhara, M. Matsuo, T. Hanamura, M. Kimura, K. Hashimoto, ISIJ International 31 (1991) 728.
[243] M. Nobuki, D. Vanderschueren, M. Nakamura, Acta Metallurgica et Materialia 42 (1994) 2623.
[244] T.G. Nieh, L.M. Hsiung, J. Wadsworth, Intermetallics 7 (1999) 163.
[245] F. Appel, Materials Science and Engineering: A 317 (2001) 115.
[246] J. Lapin, Scripta Materialia 50 (2004) 261.
[247] S. Karthikeyan, M.J. Mills, Intermetallics 13 (2005) 985.
[248] F. Herrouin, D. Hu, P. Bowen, I.P. Jones, Acta Materialia 46 (1998) 4963.
[249] S. Tsuyama, S. Mitao, K. Minakawa, Materials Science and Engineering: A 153 (1992) 451.
[250] P.I. Gouma, M.J. Mills, Y.-W. Kim, Philosophical Magazine Letters 78 (1998) 59.
[251] P.I. Gouma, M. Karadge, Materials Letters 57 (2003) 3581.